

Electrochemical Biosensors for Monitoring Complex Diseases and Comorbidities

by

Chi-En Lin

A Dissertation Presented in Partial Fulfillment  
of the Requirements for the Degree  
Doctor of Philosophy

Approved March 2018 by the  
Graduate Supervisory Committee:

Jeffrey La Belle, Chair  
Michael Caplan  
Curtiss Cook  
Sarah Stabenfeldt  
Mark Spano

ARIZONA STATE UNIVERSITY

August 2018

## ABSTRACT

Monitoring complex diseases and their comorbidities requires accurate and convenient measurements of multiple biomarkers. However, many state-of-the-art bioassays not only require complicated and time-consuming procedures, but also measure only one biomarker at a time. This noncomprehensive single-biomarker monitoring, as well as the cost and complexity of these bioassays advocate for a simple, rapid multi-marker sensing platform suitable for point-of-care or self-monitoring settings. To address this need, diabetes mellitus was selected as the example complex disease, with dry eye disease and cardiovascular disease as the example comorbidities. Seven vital biomarkers from these diseases were selected to investigate the platform technology: lactoferrin (Lfn), immunoglobulin E (IgE), insulin, glucose, lactate, low density lipoprotein (LDL), and high density lipoprotein (HDL). Using electrochemical techniques such as amperometry and electrochemical impedance spectroscopy (EIS), various single- and dual-marker sensing prototypes were studied. First, by focusing on the imaginary impedance of EIS, an analytical algorithm for the determination of optimal frequency and signal deconvolution was first developed. This algorithm helped overcome the challenge of signal overlapping in EIS multi-marker sensors, while providing a means to study the optimal frequency of a biomarker. The algorithm was then applied to develop various single- and dual-marker prototypes by exploring different kinds of molecular recognition elements (MRE) while studying the optimal frequencies of various biomarkers with respect to their biological properties. Throughout the exploration, 5 single-marker biosensors (glucose, lactate, insulin, IgE, and Lfn) and one dual-marker (LDL and HDL) biosensor were successfully developed. With the aid of nanoparticles and the engineering design of experiments, the zeta potential, conductivity, and molecular weight of a biomarker were found to be three example factors that contribute to a biomarker's optimal frequency. The study platforms used in the study did not achieve dual-enzymatic marker biosensors (glucose and lactate) due to signal contamination from localized accumulation of reduced electron mediators on self-assembled monolayer. However, amperometric biosensors for glucose and lactate with disposable test strips and integrated samplers were successfully developed as a back-up solution

to the multi-marker sensing platform. This work has resulted in twelve publications, five patents, and one submitted manuscripts at the time of submission.

## ACKNOWLEDGMENTS

The dissertation was made possible because of the supports from my committee members and Dr. Jeffrey LaBelle, as well as the generous funding from Advanced Tears Diagnostics and Mayo Clinic. The facility and administrative support from the School of Biological Health and Systems Engineering were also much appreciated. The author would also like to thank the intellectual support and friendship from David Probst and Mackenzie Honikel. The author would like to especially thank HanYin Chao for the family support. The content of this dissertation was adapted or reproduced from the author's published<sup>1-11</sup> and submitted<sup>12,13</sup> manuscripts with all coauthors' consents and all publishers' permissions. The content of this dissertation is protected by the patent disclosures listed below.

1. **Chi Lin**, David Probst, Jeffrey T. La Belle, Marcus Smith. *Analyte Detection Using Electrochemical Impedance Spectroscopy-Based Imaginary Impedance Measurement*. US Provisional Patent Application #: 62/473,894.
2. Jeffrey T. La Belle, **Chi Lin**, Jonus Reyna, Amnah Alkhan, Cael Muggeridge, Susan Sheffield. *Saliva Glucose Measurement Device and Methods*. International Patent #: PCT/US/2017/015434.
3. Mackenzie Honikel, **Chi Lin**, Andrew Pennman, Brittney Cardinel, Jeffrey T. La Belle, Pierce Youngbar, Marcus Smith. *Electrochemical Osmolarity or Osmolarity Sensor for Clinical Assessment*. International Patent #: PCT/US/2018/017158.
4. Jeffrey La Belle, **Chi Lin**, Garrett Repp, Brittney A. Cardinel, Mark Spano, Jennifer Blain Christen, HongWu Jiang, Marcus W. Smith, Andrew Penman, Pierce Youngbar, Mackenzie M Honikel. *Point-of-Care Tear Diagnostic Tool for Detecting Dry Eye Using Electrochemical Impedance Spectroscopy*. Provisional Patent Application #: 62/505,004.

## TABLE OF CONTENTS

	Page
LIST OF TABLES .....	viii
LIST OF FIGURES .....	ix
CHAPTER	
1 BACKGROUND AND INTRODUCTION .....	1
Complex Disease and Comorbidity .....	1
Example Complex Disease: Diabetes Mellitus.....	1
Example Comorbidities of Diabetes Mellitus: Cardiovascular Disease and Dry Eye ...	2
1.1 Monitoring the Right Biomarkers .....	4
Selection of Biomarkers .....	6
1.2 Modalities of Biosensors .....	14
Optical .....	15
Mechanical.....	18
Electrochemical .....	19
2 MULTI-MARKER DETECTION .....	27
Fundamental of Electrochemical Impedance Spectroscopy.....	27
Novel Algorithm for Optimal Frequency.....	30
Overview of Optimal Frequency.....	30
The Imaginary Impedance Algorithm.....	33
The Signal Deconvolution Algorithm .....	36
2.1 A Dual-Marker Prototype: Two Antibodies .....	39
Introduction .....	39
Methods .....	41
Results .....	42
Discussions.....	49

CHAPTER	Page
Conclusion .....	50
2.2 A Dual-Marker Prototype: Two Enzymes .....	52
Introduction .....	52
Methods .....	53
Results and Discussions .....	54
Conclusion .....	60
2.3 A Dual-Marker Prototype: One Antibody and One Enzyme .....	61
Introduction .....	61
Methods .....	61
Results .....	62
Discussions.....	65
Conclusion .....	67
3 FACTORS AFFECTING THE OPTIMAL FREQUENCY .....	69
3.1 Direct Measurement of a Biomarker's Native Optimal Frequency .....	69
Introduction .....	69
Methods .....	71
Results and Discussions .....	76
Conclusion .....	86
3.2 The Effect of Zeta Potential, Conductivity, and Molecular Weight on OF .....	88
Introduction .....	88
Methods .....	89
Results and Discussions .....	93
Conclusion .....	110
4 SUMMARY AND FUTURE WORK .....	111
REFERENCES .....	113

CHAPTER	Page
APPENDIX	
A PHYSICAL ADSORPTION BASED FABRICATION OF BIOSENSORS .....	128
B COVALENT BINDING BASED SENSOR FABRICATION .....	130
C QUALITY CONTROL .....	132
D SAMPLE PREPARTION AND TESTING PROTOCOL .....	134
E LASER CUTTING PROTOCOL .....	136
F ELECTROCHEMICAL CIRCUIT MODELING PROTOCOL .....	138
G CHANGE IN FERRI/FERRO CONCENTRATIONS ON SAM .....	153

## LIST OF TABLES

Table		Page
1.	FDA Approved Biomarkers for Monitoring DM, CVD, and DED .....	5
2.	Summary of the Selected Biomarkers .....	12
3.	Summary of EIS Algorithms .....	32
4.	Comparison of Optimal Frequencies .....	83
5.	Summary of the Cutoff Frequencies and the OFs of each Nanoparticle Conjugates .....	95
6.	Summary of Each Nanoparticle Conjugates and Biomarker Analyte's Results .....	102
7.	Summary of ANOVA Results .....	104



## LIST OF FIGURES

Figure		Page
1.	Randle's Circuit .....	28
2.	Differences Between Complex and Imaginary Impedance Algorithms .....	33
3.	Typical Imaginary Impedance Responses .....	34
4.	The Four Main Impedance Components of EIS .....	35
5.	Electron Flows Between an Enzymatic Reaction and an Affinity-Binding Reaction.....	40
6.	Determining the Formal Potential with Cyclic Voltammetry.....	41
7.	Nyquist Plots for LDL and HDL Sensors .....	43
8.	Electrochemical Characterization of LDL and HDL in Purified Solution.....	45
9.	Coimmobilization of HDL and LDL .....	47
10.	Electrochemical Equivalent Circuits for LDL, HDL, and Coimmobilization .....	48
11.	Electrochemical Responses of Lactate and Glucose .....	55
12.	Calibraiton Curves of Lactate and Glucose .....	56
13.	Calibration Curve of Glucose Sensor Prepared by Physical Adsorption .....	57
14.	EIS Response of Coimmobilized Glucose and Lactate .....	58
15.	EIS Deconvoluted Response of Coimmobilized Glucose and Lactate .....	59
16.	Electrochemical responses of Insulin and Glucose .....	62
17.	Calibration Curves of Insulin and Glucose .....	63
18.	Electrochemical Circuit Modeling of the Insulin Sensor .....	63
19.	Insulin Calibration Curve Using Charge Transfer Resistance .....	64
20.	Modeled Coimmobilized EIS Response of Insulin and Glucose .....	64
21.	Sensor Fabrication Schematics Using SPCE and TSC .....	72
22.	Imaginary Impedance Response of Lfn and IgE on the SPCE-Alpha Platform.....	77
23.	Specificity Testing of Lfn and IgE SPCE-Alpha.....	78
24.	Stability Testing of the Lfn and IgE SPCE-Alpha .....	79
25.	Complex Medium Testing of the Lfn and IgE SPCE-Alpha .....	80

Figure	Page
26. Robustness of the Native OF.....	81
27. Calibration Curves of the IgE and Lfn Sensor Prototypes.....	84
28. Sensor Setup for the Investigation of Optimal Frequency.....	91
29. Determination of Example Biomarkers' Optimal Frequencies.....	94
30. EIS Responses of Various Types of Nanoparticle Conjugations to the IL-12 Antibody ...	95
31. EIS Responses of Various Nanomaterials in the Presence of IL-12 antigen .....	96
32. Overlay of $Z''$ Responses of IL-12 antibody Conjugated with Various Nanomaterials .....	98
33. Overlay of Slope and RSQ values of Various Nanomaterial Conjugations .....	199
34. The Effect of Conductivity, Zeta, and Molecular Weight on the Optimal Frequency .....	101
35. Modeling of Optimal Frequency.....	103

## CHAPTER 1

### BACKGROUND AND INTRODUCTION

#### COMPLEX DISEASE AND COMORBIDITY

Complex diseases are influenced by a combination of genetics, environmental factors, and lifestyle choices. They are often accompanied by other chronic illnesses, which are referred as comorbidities. Complex diseases and associated comorbidities require a personalized and multi-staged approach to manage. The patient needs to be accurately diagnosed then prescribed the treatments, medications, and tools required to improve patient's health and quality of life. Finally, the patients need to cooperate and have the diligence to fully execute doctors' prescriptions. However, there are many unmet needs in every step. Many biomarkers used to diagnose and monitor metabolic state over time are often time consuming and costly to perform, and many of them suffer from low sensitivity and specificity. Consequently, the doctors are challenged to make medical decisions based on inaccurate and delayed results. Furthermore, after the prescribing of therapeutic treatments, the daily management of the disease and the execution of therapies can be very cumbersome to perform, causing a low compliance rate among the patients. There are also insufficient means to quickly obtain feedbacks showing the progress of the disease management. A rapid and accurate bioassay that provide timely results can empower both the clinicians and patients to achieve a more efficient healthcare system.

#### *Example Complex Disease: Diabetes Mellitus*

Diabetes mellitus (DM) is selected as the example complex disease for the scope of this dissertation due to its rising prevalence, high risk of complications, and accelerating medical costs. DM affects 347 million people worldwide and 29.1 million in the U.S.<sup>14</sup>. The number of people with DM is expected to triple within the United States by the year 2050, meaning approximately one in three adults will suffer from DM<sup>15</sup>. The average person with DM spends

\$13,700 on their supplies and treatment yearly, which is approximately 2.3 times higher than standard healthcare associated costs endured by a healthy person<sup>16</sup>.

DM is a chronic disease resulting from a hormonal disorder that causes either the inadequate production of insulin, diminished tissue responses to insulin, or both<sup>17</sup>. People with DM often suffer from large fluctuation of blood glucose, which can cause many complications if left unchecked. The two main types of DM are type 1 and type 2, with type 1 (T1D) accounting for approximately 10% of all DM cases<sup>14</sup>. Insulin therapy and many automated insulin administering technologies are very effective on T1D patients in managing their BG levels<sup>17</sup>. However, overdosage of insulin can cause hypoglycemia (abnormally low BG levels) and the subject can suffer from coma and even death if not treated immediately. Type 2 diabetes (T2D) is the majority (90%) of all DM cases<sup>14</sup>. It is typically characterized by insulin resistance and is more likely to be diagnosed later in life<sup>18</sup>. Insulin resistance is characterized by diminished responses to insulin at local tissues, which then prompt the pancreas to produce more insulin to maintain normal glucose levels. The pancreas eventually becomes unresponsive as it no longer can sustain such high levels of insulin production. T2D can be treated with lifestyle changes or oral medications early on that stimulate the secretion of insulin in the pancreas and/or the sensitivity of insulin at local tissues<sup>18</sup>.

#### *Example Comorbidities of Diabetes Mellitus: Cardiovascular Diseases and Dry Eye*

People with DM may suffer from many comorbidities such as cardiovascular diseases (CVD), retinopathy, neuropathy, stroke, obesity, and depression. According to a large clinical study published in 2006, 44.4% of DM patients suffer from one or more comorbidities<sup>19</sup>. Among these comorbidities, CVD and dry eye were selected as the example comorbidities for the scope of this dissertation. CVD is the leading cause of death in the U.S<sup>20</sup> and is responsible for 30% of all deaths globally<sup>21</sup>. People with DM are two times more likely to have CVD compared to non-diabetics, with CVD being the leading cause of death<sup>21</sup>. CVD is a collection of multiple heart

diseases that are often associated with the accumulation of plaques in the walls of the arteries. The accumulation of plaques narrows the arteries, and can potentially lead to blood clots, causing a heart attack or stroke. There are also other types of CVD such as arrhythmia, heart failures, and heart valve problems. Major CVD risk factors including poor diets, tobacco use, low physical activity levels, obesity, and hypertension<sup>21</sup>. Fortunately, due to more effective diagnostics, treatments, and better lifestyle, the mortality and prevalence of CVD in U.S. have been developed countries, suggesting the importance of multifaceted risk factor-reducing strategies<sup>21</sup>.

Dry eye disease (DED) is caused by a lack of lubrication of the ocular surface, commonly characterized by either reduced tear production levels (aqueous deficient dry eye) or increased tear evaporation (hyper-evaporative dry eye), causing great discomfort for the patient. It is one of the most prevalent ocular diseases among the epidemics of the 21<sup>st</sup> century<sup>22</sup>, affecting more than 16.4 million adults in the U.S.<sup>23</sup>. The astonishing prevalence is in part due to the widespread incidence of DM, a worldwide epidemic costing nearly \$250 billion in the U.S. alone<sup>24</sup>, as 54.3% of type II diabetic patients suffer from DED<sup>25</sup>. This statistic is projected to rise with increasing life expectancy, rising prevalence of DM, and growing ocular strain caused by increasing technology dependence.

Because of the reasons discussed above, DM, CVD, and DED are the example complex disease and comorbidities studied in this dissertation. Stemming from this combination, the next section discusses the selection of biomarkers that are often used to diagnosis or manage each disease.

*Acknowledgement:* the content of this section was adapted from the author's published works<sup>1,3,4,9</sup> with permissions from all coauthors and publishers.

## CHAPTER 1.1

### MONITORING THE RIGHT BIOMARKERS

Managing complex diseases starts with accurate measurements of multiple biomarkers to evaluate the state of health. According to the National Institute of Health, a biomarker can be described as a biological characteristic that is objectively measured and evaluated as an indicator of biological processes, pathogenic processes, or pharmacological responses to a therapeutic intervention<sup>26</sup>. It allows the investigator to evaluate outcomes, known as the clinical endpoints and surrogate outcomes. Clinical endpoints include variables reflecting how a patient functions or how long he/she may live. Since clinical endpoints may be too complicated to measure, surrogate endpoints can be used instead. By monitoring the biomarkers of interest, therapeutic and pathophysiological evidences can be collected investigate surrogate endpoints that predict clinical benefits, safety, or harm.

Monitoring multiple biomarkers have been shown to improve outcomes in many complex diseases, including DM<sup>27-29</sup>, CVD<sup>30</sup>, and DED<sup>31</sup>. While there is a plethora of biomarkers for DM, CVD, and DED, selecting the ones that are approved by Food and Drug Administration (FDA) is of utmost importance because of its influence in the commercialization of medical devices, as well as its clinical significance that has been rigorously validated. When dealing with the FDA, substantial equivalence to a preexisting device is vital in obtain the approval. Table 1 summarizes some of the common FDA approved biomarkers for DM and its comorbidity: CVD and DED.

	Diagnostic, Managing, or Therapeutic Uses	Cut-off Levels	FDA Approval Number of an Example Assay
<i>DM Biomarker</i>			
Glycated Hemoglobin	Measurement of the 3-month average plasma glucose concentration	6.5% 5.8% - 6.4% is indicative of pre-DM	K153726
<b>Glucose</b>	Measurement of blood glucose levels	Hypoglycemia: < 70 mg/dL Hyperglycemia (fasting): > 130 mg/dL	P150021
<b>Insulin</b>	Glycemic control	Hyperinsulinaemia: 20 mU/L	K963911
<b>Lactate</b>	Measurement of exercise intensity	2 – 4 mM	K100602
Zinc Transporter 8 Autoantibody	Evaluate the performance of pancreas islet cells	15 U/mL	DEN140001
<i>CVD Biomarker</i>			
Apolipoprotein B and Apolipoprotein A-I	Prognostic, risk prediction for myocardial infarction	ApoB/ApoA-I ratio > 1	K072977, K063608
Myoglobin	Detection of acute myocardial infarction	200 ng/mL	K080481
Troponin I	Detection of acute myocardial infarction	0.01 – 0.1 ng/mL	K031739
Troponin T	Detection of acute Myocardial infarction	0.05 – 0.1 ng/mL	K162895
C-Reactive Protein	Early detection of inflammation and cardiac risk factors	Less than 1 ug/mL is low risk, higher than 3 ug/mL is high risk	K040030
Creatine Kinase MB subform	Early detection of acute myocardial infarction	10 ng/mL	K022654
B-type natriuretic peptide (BNP) and N-terminal prohormone of BNP	Detection of acute coronary heart diseases, heart failure, ventricular overload	0.25 – 2 ng/mL	K021317
Myeloperoxidase	Detection of inflammation	350 ng/mL	K050029
<b>Low density- and high density-lipoprotein</b>	Evaluation of total cholesterol levels for heart artery health	LDL: 100 mg/dL HDL: 40 mg/dL	K041926

Table 1: FDA approved biomarkers for monitoring DM, CVD, and DED. Adapted from <sup>31-42</sup>. The

bolded biomarkers are the ones studied in this dissertation.

	Diagnostic, Managing, or Therapeutic Uses	Cut-off Levels	FDA Approval Number of an Example Assay
<i>DED Biomarkers</i>			
<b>Lactoferrin (Lfn)</b>	Tear composition and output of lacrimal gland	1.1 mg/mL	K042071
<b>Immunoglobulin E</b>	Allergic reactions	80 ng/mL	K061970
Matrix Metalloproteinase 9	Tear composition and output of lacrimal gland	40 ng/mL	K132066
Osmolarity	Reduced tear secretion or increased tear evaporation	308 mOsm/L	K083184

Table 1: *continued*

Table 1 encompasses a large number of FDA-approved biomarkers that should be measured simultaneously to monitor both the DM and its comorbidity. To build the functional prototypes of the multimarker sensor, the following biomarkers were selected based on their applications and their biological characteristics to build either the single-marker or dual-marker prototypes. The selected biomarkers were: glucose, insulin, lactate, LDL, HDL, Lfn, and IgE.

## SELECTION OF BIOMARKERS

### *Lactoferrin and Immunoglobulin E (Lfn and IgE)*

Lfn and IgE are two biomarkers representative of DED and allergic conjunctivitis (AC). DED and AC are considered as the two most prevalent ocular diseases among the epidemics of the 21<sup>st</sup> century<sup>22</sup>. Similar to the prevalence of DED, AC, is estimated to affect 40% of the American population<sup>43</sup>. In 80% of all cases, AC symptoms arise prior to adolescent years, and can worsen with prolonged exposure to environmental irritants, which significantly impact patient's quality of life<sup>44</sup>. Unfortunately, AC is often underdiagnosed and not treated until very severe<sup>45</sup>. This can be attributed to the wide overlap of symptoms<sup>46</sup> such as itching, redness, and inflammation, as well as the lack of a reliable POC diagnostic tool. Misdiagnosis commonly leads to ineffective prescribed treatments, adverse or worsening conditions, and increased economic burdens placed



upon both patients and physicians. A tool facilitating differential diagnosis of DED and AC can be very helpful in alleviating the high diagnostic demand<sup>31</sup>.

Lfn is a FDA approved tear dry eye biomarker that correlate well with tear composition and output of the lacrimal gland<sup>34,47</sup>. Specifically, Lfn is very effective in diagnosing aqueous deficient dry eye and Sjogren's syndrome<sup>48</sup>. Currently, Lfn can be detected using immunodiffusion assays such as Lactoplate, lactoferrin test kits and enzyme-linked immunosorbent assays (ELISA)<sup>31,49</sup>. However, these tests are incapable of providing immediate results and are costly to perform. Similarly, to test for allergies, patients are subjected to a panel of immunogenic antigen species likely to trigger allergic responses, which can be costly to the patient and provider<sup>50</sup>. Since elevated IgE levels are often observed in allergic responses<sup>44</sup>, it is an additional FDA approved biomarker for allergic reactions<sup>51</sup> and is recommended as the primary biomarker for AC<sup>52</sup>. Much work toward a quantitative IgE assay is in progress<sup>53-55</sup>, but there is currently a lack of POC diagnostic tools suitable for rapid, sensitive and inexpensive diagnosis of ocular conditions. A dual marker (Lfn and IgE) POC platform may help differentiate and evaluate the conditions of DED and AC rapidly, reducing the cost and time required for diagnosis. The two biomarkers are also very useful in laying the foundation of biosensors that utilize the antibody as the molecular recognition element (MRE). Under the collaboration with Advanced Tear Diagnostics, the author has successfully developed the said dual marker POC platform using the screen-printed carbon sensor<sup>9</sup>, as explained further in Chapter 3.1. The experience and knowledge gained throughout the process were vital in understanding the challenges and limitations of developing a dual-marker prototype in disposable sensor settings.

### *Glucose*

Glucose is perhaps the most important biomarker for people with DM and is the most direct means to evaluate a person's glycemic state. The normal blood glucose level can vary among individuals depending on their metabolisms. For healthy and non-diabetic people, the normal

blood glucose level should fall between 70 to 125 mg/dL with a mean of 100 mg/dL<sup>56</sup>. For DM, the American Diabetes Association recommended to maintain a blood glucose level within 90 – 130 mg/dL before meals and less than 180 mg/dL after meals<sup>56</sup>. For people with DM, frequent glycemic fluctuation above these suggest ranges may lead to many microvascular complications.

Glucose is a very small molecule with a molecular weight of 180.16 Da. Its MREs operate in a very different way from affinity-binding MREs such as antibodies. The MREs of glucose are enzymes with various types of cofactors, which can generate electrons when binding with glucose. Since it operates very different from antibodies, it is interesting to study its optimal frequency and how it differs from other affinity-binding based biomarkers' optimal frequencies. Being a well-studied biomarker with many commercially available products, glucose is also ideal for training and learning sensor production and improvement. Patient's noncompliance is a major issue in managing complex diseases. In the case of DM, one primary contributor to noncompliance is the pain and inconveniences of needle pricking. Therefore, developing noninvasive glucose sensors can be both practical and informational throughout the learning process. As a result, the author has developed a noninvasive tear glucose sensor with integrated tear capturing component that has resulted in 3 publications<sup>6,8,10</sup>. The experience and knowledge obtained from developing the tear glucose sensor has enable the author to appreciate the electrochemical phenomenon and the design of noninvasive biosensors.

### *Lactate*

Lactate is an important biomarker (90.08 Da molecule) often measured in clinical diagnostics<sup>57</sup> and in monitoring the fitness of athletes<sup>58</sup>. Lactate levels in the body indicate oxygen deficiency or elevated salt concentrations and can be altered due to pathophysiological conditions or intensive exercise<sup>59</sup>. In terms of pathophysiological conditions, elevated blood lactate concentration can reflect lactic acidosis caused by various factors such as toxins, shock, anemia, sepsis, and organ failure<sup>60</sup>. Because of these potential pathophysiological conditions, lactate is often monitored

closely in intensive care units and emergency rooms<sup>57</sup>. Lactate can also become elevated after intensive exercise, reflecting physical strain after prolonged periods of extensive anaerobic activity<sup>58</sup>.

Besides its significance in clinical environments, monitoring lactate is particularly beneficial to evaluate exercise intensity in DM patients. Exercise is a common therapeutic treatment prescribed to DM patients due to its significant improvement in long-term glycemic management<sup>61</sup>. While there are other ways to measure exercise intensity such as heart rate monitoring, blood lactate concentrations have been recommended as a superior predictor and indicator of exercise performance<sup>62</sup>. Its MREs are very similar to glucose's as they also utilize enzymatic reactions. Due to their similarity and clinical relevance for DM, glucose and lactate are ideal exemplary biomarkers to build a dual-enzymatic biomarker sensor prototype to investigate the mechanisms and challenges to implement enzymatic biomarkers in a multi-marker platform technology (Chapter 2.2).

Similar to glucose, lactate also has many commercially available biosensors, making it a good biomarker for training and learning purposes. Since many commercial lactate sensors require the use of needle, monitoring blood lactate levels can have similar noncompliance issue as blood glucose meters described above. Owing to the success of the tear glucose sensor, the author has cooperated with the Tokyo University of Agriculture and Technology to develop a tear lactate sensor employing a genetically modified lactate oxidase<sup>7</sup> and an integrated tear capturing component<sup>12</sup>. The endeavour has allowed the author to appreciate the biochemical and molecular aspects of a MRE.

### *Insulin*

Monitoring blood glucose levels alone may not be sufficient in maintaining tight glycemic control, as normal glucose homeostasis is determined by interactions between glucose, insulin, and other

biomarkers reflecting the intricate metabolisms of human body. Using Medtronic recent groundbreaking invention of pseudo-artificial pancreas as an example, relying solely on glucose measurements can have multiple disadvantages. The artificial pancreas consists of an automated insulin pump, a continuous glucose monitor (CGM), and a complex algorithm to determine insulin dosage based on CGM feedback. Unfortunately, the insulin bolus calculator does not account for the total amount of insulin in the body, but only how much insulin has been delivered. As a result, there is a 40% chance of both insulin overdose and underdose<sup>63</sup>. In addition, the insulin infusion set can fail with a false positive rate of 0.3/day<sup>64</sup>, and the CGM's accuracy can be affected by pressure-induced sensor attenuation, as well as exercising and other personal life choices<sup>65,66</sup>. Most importantly, commercial insulin vials were found to have large deviations from their advertised values<sup>67</sup>. All of these issues suggest the need for a rapid and convenience means of measuring insulin. Monitoring insulin and glucose simultaneously may provide a more comprehensive and accurate evaluation of a person's glycemic fluctuations than glucose alone, diverting the risk of algorithms built solely on glucose<sup>3</sup>.

Insulin is a 5700 Da molecule secreted from the pancreas to regulate blood glucose<sup>68</sup>. Due to its small molecular size, self-aggregation properties, and pico-molar concentrations in the body, measuring insulin has been a very challenging task. Using insulin as a target biomarker, not only does its single-marker sensor prototype solves critical needs, the combination of glucose-insulin dual marker prototype can serve as a crucial demonstration on how to achieve multi-marker detection using an affinity-based biomarker and an enzymatic biomarker (Chapter 2.3).

#### *Low-Density Lipoprotein and High-Density Lipoprotein (LDL and HDL)*

LDL and HDL (low density- and high density lipoproteins) are two vital biomarkers for the coronary heart disease, which accounts for more than 800,000 deaths in the U.S. and is the leading cause of death in all CVDs<sup>69</sup>. The National Cholesterol Education Program recommended the use of LDL and HDL as risk indicators for CVD<sup>30</sup>, and the LDL/HDL ratio has also been shown

to be an excellent predictor for the coronary heart disease<sup>70</sup>. Besides their clinical relevance, the two biomarkers are very similar in structure. A lipoprotein is a lipid-transferring biomolecule consists of a core of lipids and a shell of phospholipids and apolipoproteins. Depending on the ratio of the shell and the core, various sizes or density of lipoprotein can be formed. The HDL contains much less lipids as compared to LDL, resulting in a much smaller molecular weight of 175 kDa as compared to LDL's 512 kDa<sup>71</sup>. Different types of lipoproteins also have different kinds of apolipoproteins, which have different binding receptors. Apolipoprotein B is the primary type of apolipoproteins for LDL and apolipoprotein A1 for HDL, allowing them to be differentiated by appropriate MREs<sup>72</sup>.

Since LDL and HDL are very similar in structure as compared to other affinity-based binding biomarker, detecting both simultaneously can be the most very challenging to build in the multi-marker sensor platform. They also differ significantly from the enzymatic biomarkers in that the binding reaction does not generate electrons, further complicates their detection. Successful development of a LDL and HDL dual-marker prototype is therefore the hardest yet most rewarding dual-marker prototype, as discussed in Chapter 2.1.

#### *Summary of the selected biomarkers*

Through the 7 selected biomarkers, different biomolecular properties that are vital for the multi-marker detection platform can be investigated, such as 1) enzymatic reaction versus affinity binding, 2) large distribution of molecular weight, and 3) structural disparity (Table 2). The single-marker and dual-marker sensor prototypes developed for the selected 7 biomarkers not only can lay a solid foundation for developing the multi-marker sensor platform, but also meet practical clinical needs.

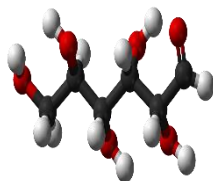
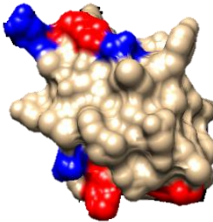
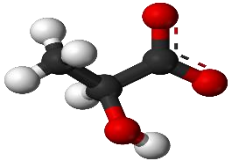
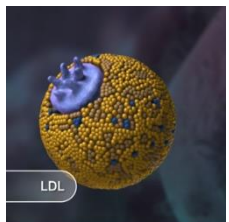

Biomarkers	Molecular Weight (Da)	Molecular Recognition Elements	Target Analyte's Structure
Glucose	180	Enzyme	 <p><a href="#">This Photo</a> by Unknown Author is licensed under <a href="#">CC BY-SA</a></p>
Insulin	5700	Antibody	 <p>Reference: PDB file 3I40 from <sup>73</sup></p>
Lactate	90	Enzyme	 <p><a href="#">This Photo</a> by Unknown Author is licensed under <a href="#">CC BY-SA</a></p>
Low density lipoprotein	175,000	Antibody	 <p><a href="#">This Photo</a> by Unknown Author is licensed under <a href="#">CC BY-ND</a></p>
High density lipoprotein	512,000	Antibody	 <p><a href="#">This Photo</a> by Unknown Author is licensed under <a href="#">CC BY-ND</a></p>

Table 2: Summary of the selected biomarkers.

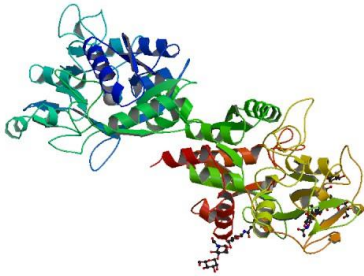
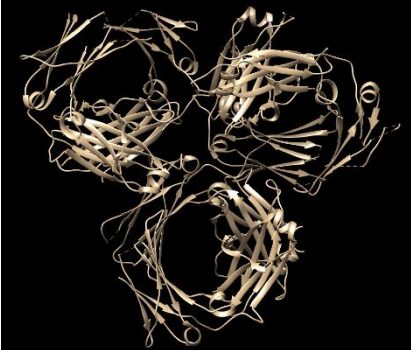
Biomarkers	Molecular Weight (Da)	Molecular Recognition Elements	Target Analyte's Structure
Lactoferrin	80,000	Antibody	 <p data-bbox="959 762 1289 816"><a href="#">This Photo</a> by Valencia UPV is licensed under <a href="#">CC BY</a></p>
Immunoglobulin E	200,000	Antibody	 <p data-bbox="943 1182 1338 1209">Reference: PDB file 5MOI from <sup>74</sup></p>

Table 2: *continued.*

*Acknowledgement:* The content of this section was adapted from the author's published work with the permission of all coauthors<sup>1-6,9-13</sup>.

## CHAPTER 1.2

### MODALITIES OF BIOSENSORS

To diagnosis and monitor complex diseases, biosensors can be developed in many ways to measure the biomarkers of interest. Depending on the intended applications, biosensors can be built to suit lab setting, point-of-care, and at-home use. Each application comes with different requirements of performance and cost. In general, the lab setting biosensors are often most accurate and novel, as new assays can be developed and tested against the state-of-the-art instruments for validation. After years of development and improvement, a lab-grade biosensor may successfully be translated into a point-of-care biosensor, which is performed by trained professionals or patients using meters and procedures that are much cheaper than the state-of-the-art instruments but are still too expensive and complicated for ordinary people. After a biosensor is fully matured in robustness, accuracy, simplicity, and manufacturing, it can be performed by untrained, ordinary people and becomes suitable for at-home use. To accurately diagnosis and manage complex diseases as well as raising health awareness, the need for rapid biosensors suitable for POC and at-home usage cannot be overstated.

Generally, a biosensor consists of two major components: a biologically derived recognition element, and a transducer. The recognition element may be in various forms such as enzymes or antibodies; and is responsible for capturing the target analytes. The transducer component is responsible for converting the binding reaction to measurable signals. Among many transducer modalities, mechanical, optical and electrochemical approaches are most commonly used. Depending on how the recognition element works, these modalities are often coupled with sample/analyte preparation methods to achieve labelled or label-free detection of target analytes. Besides enzymatic reactions, most biorecognition events do not generate significant amounts of measurable signal. Labelled approaches are often therefore regarded as the gold standard because the signal enhancement from labels permits accurate detection of target analyte.



Common labels include fluorescence, nanoparticles, enzymes, and electron mediators. However, to achieve biosensors that are suitable for point-of-care or at-home use, label-free detection is much preferred over labeled approach because of the reduced complexity and sample handling. The following sections describe each modality and discuss its ability to achieve label-free detection and/or approaches to achieve multi-marker detection.

## OPTICAL

Optical biosensors remain the most heavily used type of biosensor, achieving more than 93,200 publications in the medical field in the past 15 years. Labeled methods, such as ELISA utilize a fluorescent dye, or optical beacon to detect a target molecule, offering phenomenal sensitivity, but increasing complexity. It is capable of achieving multi-marker detection by employing multi-sensor arrays and sample labeling<sup>75-78</sup>. Each ELISA well can contain multiple sub-wells with immobilized MREs for the biomarkers of interest. Upon target capturing, secondary antibodies with fluorescent or chemiluminescence can be added. Tertiary antibodies or cascade reactions can be used to enhance target signal at the cost of increasing complexity. Instruments that are capable of running multiple ELISA plates at once can also be considered as a way for multi-marker detection. However, although the well-performing microarray sandwich assays have large dynamic ranges, reproducibility and complexity can be challenging in clinical practices. The cross-reactivity of the detection antibody (i.e. labels) can severely impede the multiplexing accuracy of the sandwich assays. In addition, an ELISA reader is quite expensive, and the procedures are too complicated for it to serve as a point-of-care or for patient use.

Label-free optical methods in contrast offer many benefits such as lower cost, and ease of use as well as reduced human error that may be introduced during the extensive labeling procedure, but it is much susceptible to noise. Currently, several label-free optical methods exist to measure biomarker concentrations, including surface plasmon resonance (SPR), surface enhanced Raman spectroscopy, and optical waveguide<sup>79</sup>.

Surface plasma resonance (SPR) is a label-free, real-time method having various designs such as prism coupling, waveguide coupling, optical fiber coupling, and long/short range surface resonance. The phenomenon was originally observed in 1907 by Dr. Jonnathan Zenneck<sup>80</sup>. In principle, a laser light source is passed through a prism, contacting the sensor substrate. The reflected beam reflects off the surface at a specific angle, known as the resonance angle, which provides information about the refractive indices of the system. In biosensor applications, when target analyte binds to the sensor surface that has been functionalized with complementary MREs (ligands, antibodies, aptamers, nucleic acids, etc.), it creates a difference in refractive indices, which alters the propagation of the electromagnetic wave. The addition or removal of the analytes changes the angle at which light is reflected, which can be correlated to the amount of biomolecule present and provide real-time information on the analyte-ligand binding kinetics. Prism coupling SPR, the most commonly used platform, operates according to the following equation:

$$\beta_{sp} = \frac{2\pi}{\lambda} n_p \sin(\theta)$$

where  $\lambda$  is the incident wavelength,  $n_p$  is the prism refractive index,  $\theta$  is the incident angle and  $\beta_{sp}$  is the propagation constant of the square wave prism. SPR is often coupled with an array of biosensors to achieve multiplexing capabilities<sup>81,82</sup>.

Another equally popular optical technique is the surface enhanced Raman spectroscopy (SERS). SERS functions through the inelastic scattering of monochromatic light, which can be measured in comparison to the input to determine a molecule's energy signature. The metallic surface utilized in SERS is intentionally roughened using various nanostructures, allowing it to overcome the otherwise low sensitivity of traditional Raman spectroscopy<sup>83</sup>. It can be used to achieve multi-marker detection by pairing the target with various fluorescent dyes or molecular beacons. It's multi-marker detection utility has been demonstrated in the detection of both the proteomic biomarkers<sup>84</sup> and enzymatic biomarkers<sup>85</sup> with high sensitivity as long as the fluorescent dyes are accurately paired. However, in addition to expensive instrumentations, laborious labeling process

are also required and permanent damage to the protein structure can occur. It is possible to achieve label-free, multi-marker detection using SERS after attaching the proteins onto the metallic surface. By achieving different surface structures through nanopatterning (i.e. nanovoids), the functionalized metallic surface permits only the selected antibodies to bind.<sup>86</sup> Different antibody-antigen biorecognition will yield different Raman intensity peaks, which could be compared against controls to achieve multi-marker detection. However, current fabrication of nanovoids is still very complicated, which limits its ability to be mass-manufactured.

Optical waveguide biosensors utilize the principle of total internal reflection, which occurs when the incident light hits the surface at an angle greater than the critical angle. To achieve this, typically the core material where the incident light passes through (i.e. glass or optical fiber) must have much greater index of refraction than the surrounding material (i.e. clad materials). While the incident light propagates through the core material, since not all of the electromagnetic energy is reflected back, an evanescent wave will form outside of the clad materials. Label-free optical waveguide biosensors can be achieved by immobilizing the molecular recognition elements onto the clad materials, and observe the change in evanescent field<sup>87</sup>, as its intensity decreases proportionally with the distance from the interface.

In general, there are various optical techniques capable of achieving sensitive, multi-marker POC biosensors. However, maintaining high reproducibility can be challenging due to the cross-reactivity of the detection antibody and variability in the testing medium. Optical techniques also often require expensive instruments, limiting its use in point-of-care diagnostics. It is also susceptible to temperature and pH fluctuations. However, due to its phenomenal sensitivity and accuracy when all the parameters are perfectly controlled (especially the labelled method such as ELISA), it remains as the gold standard method suitable for validating the performance of other biosensing modalities.

## MECHANICAL

Mechanical biosensors transduce a biological binding event into a measurable, physical quantity such as force, displacement, and oscillation. The use of mechanical biosensors has grown in parallel to the progress of micro- and nanomachining and the growing capabilities in semiconductor fabrication. Improvements in manufacturing have permitted highly sensitive detection limits, achieving pico-Newton level resolution which dictate many biological interactions<sup>88</sup>.

The most common architecture for label-free mechanical-based sensors relies on a microcantilever. Generally, cantilevers are designed through micromachining of a small “diving board” shaped device composed of a semiconductor material such as silicon. The surface is then functionalized with a recognition agent which is exposed to the analyte sample. Binding events induce deflection of the cantilever, or in the case of dynamic sensors, yield alterations in the resonant frequency oscillation patterns. These fluctuations of the homeostatic rhythm are proportional to the amount and rate of analyte binding<sup>88-90</sup>.

The system is then converted to some stimulus, whether it be optical, electrical, or mechanical, this stimulus will be altered according to the change in concentration of target analyte. Resonance frequency may be one of the most widely used methods in cantilever and sensor design. This comes from the theory that when a cantilever interacts with some molecule, the natural resonant frequency will change in direct proportion to the amount of binding, and rate of binding which occur on the surface<sup>89</sup>. The modulation of the resonant frequency can be described by the following equation:

$$\Delta f = \frac{1}{2} f_n \left( \frac{\Delta k}{k} - \frac{\Delta m}{m_n} \right)$$

where  $\Delta m$  is the change in mass from analyte binding relative to the initial mass  $m_n$ ,  $\Delta k$  the change in spring constant  $k$ , which results in a change in the resonant frequency  $f_n$ <sup>89,91-94</sup>.

Quartz crystal microbalance (QCM), an additional mechanically-based system, measures the shear oscillations caused by analyte binding to the substrate, which alters the frequency of the quartz crystal resonator. A thin gold layer is applied to the wafer substrate and functionalized with various molecular recognition elements. Following covalent immobilization, continuous analyte flow yields deposition onto the substrate and a direct change in the resonant frequency<sup>95</sup>.

Although highly sensitive, the practicality of mechanical biosensors constitutes a severe drawback. Sensor drift can limit the realistically achievable detection limits, especially when operating these systems under non-vacuum conditions, in the presence of complex solutions. Additionally, multiplexing capabilities requires assembly of an array of individually functionalized, closely packed sensors, and requires complex electrical deconvolution<sup>88</sup>.

## ELECTROCHEMICAL

Electrochemical approaches convert the analyte binding into measurable electrical signals by utilizing electron mediators<sup>96</sup>. It is most successful in biomarkers using enzymatic reactions, as the generated electrons can be easily measured as electrical signals. In biorecognition events without measurable signals, electroactive labels (enzymatic labels, electron mediators, nanomaterials) can be used to increase sensitivity with the tradeoff of increased complexity and cost. Similar to the optical approaches, analyte labeling<sup>77</sup> and multi-sensor array<sup>75,76</sup> are often used to achieve multi-marker detection, but there are also a few electrochemical techniques that are capable of label-free multi-marker detection. The following section describes common electrochemical techniques suitable for rapid biosensors, with highlights in label-free and multi-marker detection when applicable.

Amperometric approaches measure the resulting current produced by either the oxidation or reduction of a biological analyte in the presence of an applied potential. It is preferred for its simplicity and ease of manufacture, making it highly desirable in POC applications. Amperometric

detection techniques are commonly used in enzymatic reactions, such as glucose monitoring devices, in which the reaction between the analyte and enzyme generates electrons. For affinity binding based reactions such as antibody and antigen binding, enzymatic or electron-carrying labels can be used. A select few amperometric techniques are described here, highlighting the differences among the signal inputs. For a comprehensive review please see the work of A. Bard and L. Faulkner<sup>97</sup>.

Cyclic voltammetry (CV) is one of the most fundamental amperometric techniques, and provides information regarding the redox potential of the reaction. The electrochemical cell commonly contains an electron mediator, which continuously undergoes voltage induced redox reactions, facilitating electron transfer to the electrode. In CV, a voltage sweep is performed between two defined voltages at a fixed rate while the corresponding current is recorded. The linear sweep between the predetermined voltages is defined by a scan rate (V/s). Upon the completion of one linear sweep, the reverse scan is performed, forming a sawtooth, cyclical pattern<sup>96</sup>. The resulting voltammogram is a plot of current vs. voltage. The voltage is measured between the working and reference electrodes while the current is measured between the working and counter electrodes. The measured current (*i*) follows the Randles-Sevcik equation below<sup>97</sup>:

$$i_p = 0.4463 nFAC \left( \frac{nFvD}{RT} \right)^{\frac{1}{2}}$$

where  $i_p$  the maximum current,  $n$  is the number of electrons transferred in the redox event,  $F$  the Faraday constant,  $A$  the surface area of the electrode,  $D$  the diffusion coefficient,  $C$  the concentration,  $v$  the scan rate,  $R$  the gas constant, and  $T$  the temperature.

As the voltage is swept from positive to negative the electroactive species undergoes oxidation and reduction. Upon total reduction and oxidation of the species at the surface of the electrode, the current will peak at opposite polarity<sup>97</sup>. Through the exploration of both the forward and reverse reactions, information regarding the reversibility of the reaction and surface electrochemistry of the entire electrochemical cell is generated. The identified oxidation and

reduction voltages are commonly exploited in other amperometric techniques, serving as potential DC offset voltages for time-dependent electrochemical reactions and are often preferred for the desirable signal-to-noise ratios<sup>98–101</sup>. The formal potential (average of the oxidation and reduction voltages) is often exploited in impedimetric techniques.

The sensitivity of amperometric techniques is one of the shortcomings. To increase signal amplification, the conjugation of conductive nanomaterials and enzymatic labels (i.e. peroxidase) can be utilized. Not only does this combination supply electrons to the system through the enzymatic reaction, but also provides a conductive infrastructure for enhanced electron transport<sup>102</sup>. The CV results demonstrated wider detection limits on the nanomodified platform as compared to the bare platform. Although impractical by industrial standards for POC diagnostics, where the target analytes are often too low for CV without invoking complicated labeling and manufacturing procedures, the technique is still the standard for characterization of the electrochemical cell and the basis of electrochemistry<sup>97</sup>.

Chronoamperometry is another amperometric technique which uses a potentiostat to supply specific voltages to the cell in a strategic manner, and records the resulting current as a function of time<sup>103,104</sup>. Many different types of step waveforms exist and are further discussed by Bard and Faulkner<sup>97</sup>. The applied voltages are unique to the system because they can either be excitatory or inhibitory. Certain potentials will not elicit an electrochemical response by the species in solution, deemed electroinactive. These regions do not facilitate charge transfer at the interface of the electrode and the solution, producing no faradic current. However, upon the introduction of a strong voltage, electrons will flow between the electrode and the species, generating a current response. The transfer of electrons, and thus the generated current is proportional to the flux of species within the cell. The continued supply of voltage will cause a vast accumulation of reduced species at the surface of the electrode, termed the depletion zone, and the current response will decay<sup>97</sup>. Therefore, the rate of mass transfer of the species to the electrode is the limiting factor in

the current response. Upon the removal of the reducing potential, the species will oxidize, generating a current response of opposite polarity, until the eventual saturation state and relaxation of the response. Because of this phenomenon, selection of bias voltage is extremely important in any electrochemical techniques, as the current generated from non-target electroactive species (noise) should be minimized.

Chronoamperometry provides real-time, sensitive information of the electrochemical system. The versatility of applied input potentials make it desirable for the detection of many electrochemical analytes in DM and its comorbidities. Enzymatic biomarkers such as glucose and lactate are both ideal candidates for amperometric detection because their high concentrations in the body, allowing robust and label-free detections. Using this amperometric technique, the author has successfully developed a tear glucose<sup>6,10</sup>, a saliva glucose<sup>2</sup>, and a tear lactate biosensor<sup>7,12</sup> for noninvasive monitoring. Unfortunately, since amperometric techniques rely on enzymatic reactions or electron facilitating labels, it has limited utility in achieving label-free detection in affinity-based reactions, such as the antibody and antigen.

In contrast to amperometric techniques, potentiometric techniques measure the charge accumulation under the influence of a stable potentials<sup>96,105</sup>. Within the electrochemical cell, the reference electrode is maintained at a precise voltage, while the ionic content of the solution yields differences in the potential measured at the working electrode. Through assessment of the reported voltages, the composition of the solution in question can be determined. Electrode configurations containing ion selective membranes have been essential to the utilization of this technique in biosensing applications.

Potentiometric sensing gained popularity with the introduction of ion selective electrodes in the 1980s, and currently remain the largest, most widely used subset of potentiometric sensors in the field[36]. These sensor archetypes employ ion selective membranes, which effectively facilitate



the transport of selected ions across a conductive membrane. This creates an interface between the bulk solution and the active electrode, separating two solutions of varying ionic activity. The restrictive permeability of the membrane enables charge separation within the system and is ultimately responsible for signal generation, and reported selectivity<sup>106,107</sup>.

Although biomarkers are most commonly proteins, ions such as  $\text{Ca}^{2+}$  can provide physicians with insight into the efficacy of cardiac muscle contraction and is crucial for many signal transduction pathways and enzymatic reactions<sup>108</sup>. Therefore, assessment of  $\text{Ca}^{2+}$  content in biological fluids can be extremely valuable. The development of ion-selective electrodes for clinical applications remain under development<sup>109</sup>. However, advancements toward POC applications have been limited to DNA hybridization biosensors for diagnostic use<sup>110,111</sup>. Improved sensor qualities such as low detection limits, increased sensitivity and selectivity remain within the scope of many research efforts. However, device miniaturization, broadened applicability to clinically relevant ions and reduced electrode variability are a few of the concerns hindering the progress of ion selective membrane sensors<sup>106,107</sup>.

Field effect transistors (FETs) encompass one class of potentiometric sensing devices, highly desired due to the ease of small scale fabrication, rapid detection capabilities, low power consumption and on-chip integration<sup>106,112</sup>. The electrode configuration consists of a source and drain electrode, maintained at a stable bias and connected by a third electrode, termed gate electrode, which varies the supplied electric field potential. Additionally, the gate is coupled to a dielectric material, which undergoes changes in conductive properties with modulation of the electric field. This affects the current flow between the drain and source electrodes, resulting in signal production<sup>112</sup>.

The desirable performance characteristics of FETs has led to an exploration of biosensing applications and a subset of FETs, termed BioFETs<sup>113</sup>. The most applicable platform for

biomarker detection applications is the enzyme field effect transistor (EnFET). It can also be used in DNA- and cell-based models<sup>106,113</sup>. With similar operating principles as a standard FET, the primary difference is the substitution of the gate electrode for a biochemically sensitive surface, which remains in contact with the biological sample. Several studies utilize the deposition of an enzyme-functionalized dielectric layer, containing receptors to the analyte of interest. Upon binding and capture of the target analyte, the enzymatic reaction results in the consumption or production of ionic species, which can be detected by ion selective electrodes, and ultimately correlated back to concentration of the analyte<sup>113</sup>.

Various research efforts have explored the potential of antibody-based detection of CVD biomarkers using FETs. The conductive channel connecting the two electrodes, consisting of silicon nanowires is functionalized with the recognition antibody. Upon binding of charged analytes, a change in the conductance is transduced into a detection signal. The platform was utilized in the detection of cTnI and has produced detection limits (~2 ng/mL) comparable to that of the clinical gold standard<sup>114</sup>.

The rapid, label-free nature of potentiometric devices make them highly desirable in a POC setting<sup>114,115</sup>. However, current challenges associated with surface patterning, reproducibility and non-linearities have prevented successful commercialization of FET devices as diagnostic tools<sup>96,113,116,117</sup>. Furthermore, the large antibody structures used to detect biomolecules extend several nanometers from the nanostructure, producing ion screening effects and ultimately reducing sensitivity<sup>118,119</sup>.

Impedimetric biosensors contrast significantly with the previously discussed electrochemical techniques. Unlike amperometric and conductometric modalities, which employ a rather disruptive input to drive the system away from equilibrium and quantify the relaxation response, impedimetric techniques are much less intrusive to the system, permitting investigation of the

steady-state response following a small perturbation<sup>97</sup>. Commonly, a sinusoidal potential is applied to the electrochemical cell, and the resulting impedance, or obstruction to electron flow, due to molecular interactions and diffusion kinetics is measured<sup>120</sup>. This phenomenon yields desirable sensor performance characteristics such as increased sensitivity, precision and long-term stability, which have undoubtedly led to the exploration of immunosensor applications, encompassing medical, environmental and bacterial sensing.

The most representative impedimetric technique is the electrochemical impedance spectroscopy (EIS). It delivers, a sinusoidal voltage input encompassing a wide frequency spectrum at a pre-defined DC offset voltage (i.e. formal potential as discussed previously) and amplitude, while measuring the resulting current through the cell. The electrochemical reaction (binding, enzymatic, hybridization etc.) occurring at the working electrode influences the conductivity of the cell, generating a quantitative change in the input signal<sup>96</sup>. This is commonly seen as a change in magnitude or phase shift to the sinusoidal signal input. In the case of affinity-based binding, the signal generation is the obstruction of electron flow to the sensor surface due to steric hindrance or electrostatic interactions generated from the binding between antibody and antigen<sup>121</sup>. The hindrance of current flow can be modeled by resistive and capacitive elements, which together yield a frequency-dependent response, termed impedance (Z). In simple terms, EIS measures the obstruction to current flow through the electrochemical systems, allowing it to achieve label-free detection.

EIS offers great sensitivity (down to femto-molar) and rapid testing capabilities (< 1 minute). In conjunction with its label-free nature and wide spanning POC applications, it has many competitive advantages. EIS has been applied to multiple testing mediums, with various detection targets including DNA, proteins and whole cells, and successfully demonstrated feasibility in achieving relevant detection limits<sup>122–127</sup>. Advancements in sensor array development and deconvolution algorithms also permit simultaneous detection of two biomarkers enabling

enhanced specificity and assessment of potential comorbidities<sup>128</sup>. However, the technique is not without imperfections. The practicality and feasibility of EIS into clinical practice remain some of the greatest challenges. Variation resulting from surface functionalization methodologies, as well as the difficulty associated with large scale manufacturing remain a concern for many industrial entities<sup>129</sup>. However, current work is being pursued to simplify the immobilization process and meet the industrial requirements without sacrificing the sensitivity nor dynamic range of the sensor<sup>9</sup>. In general, as elucidated herein, the advantages of electrochemical techniques make them great competitors for next generation clinical assays. Their performance capabilities in conjunction with low production costs and POC feasibility greatly surpass current SOTA diagnostic tools.

### *Summary*

Among various detection modalities, EIS is most suitable for rapid, label-free POC diagnostics. Using EIS and the selected biomarkers, the author attempted to develop various single- and dual-marker biosensor prototypes to be incorporated in the multi-marker sensing platform, as discussed in the following chapter.

*Acknowledgement:* The content of this chapter is adapted from author's published manuscripts<sup>1-9</sup> and submitted manuscripts<sup>10-13</sup> with all coauthors' consents and all publishers' permissions.

CHAPTER 2  
MULTI-MARKER DETECTION  
FUNDAMENTAL OF ELECTROCHEMICAL IMPEDANCE SPECTROSCOPY

The key to enable electrochemical impedance spectroscopy's (EIS) potential of label-free multimarker detection is the concept of optimal frequency. Although many researchers have acknowledged its existence, it is still a relatively new concept<sup>130–133</sup>. In general, the optimal frequency is the frequency at which a biomarker can be quantified sensitively and accurately. Besides the potential of multimarker detection, it is also more advantageous than traditional EIS approaches in that the sensitivity, specificity, and assay time can all be improved. In addition to multi-marker detection, optimal frequency is also very useful in quality control. Using insulin as an example, after establishing its optimal frequency using a controlled EIS sensor, the same sensor can be used by customers to evaluate the concentration of insulin in a commercially off the shelf vial (see section 2.3 for more details). By surveying the literature, the following section discusses a few methods to determine the optimal frequency of a biomarker.

Prior to the discussion of algorithms, it is important to discuss the fundamentals of EIS. EIS follows the Ohm's Law in the form of:

$$Z(j\omega) = \frac{U(j\omega)}{I(j\omega)} \quad \text{Equation 1}$$

where  $Z$  is the complex impedance,  $\omega$  the angular frequency (which is equivalent to  $2\pi f$  where  $f$  is the input frequency),  $U$  the input signal, and  $I$  the current response. EIS works by supplying a small sinusoidal wave to the electrochemical cell, and then converts the sinusoidal current responses and phase shifts into complex impedance. The input signal can be expressed as:

$$U(j\omega) = U_b + U_0 * \sin(\omega t) \quad \text{Equation 2}$$

where  $U_b$  represents the biased voltage (which is typically the formal potential),  $U_0$  the voltage amplitude, and  $t$  the time. The current response can be expressed as:

$$I(j\omega) = I_b + I_0 * \sin(\omega t + \phi) \quad \text{Equation 3}$$

where  $I_b$  represents the current response,  $I_0$  the current amplitude and  $\phi$  the phase change.

Substituting Equation 2 and 3 into Equation 1, Equation 1 can be rewritten as:

$$Z(j\omega) = Z_b + Z_0 * \frac{\sin(\omega t)}{\sin(\omega t + \phi)} \quad \text{Equation 4}$$

where  $Z_b$  is the baseline resistance, and  $Z_0$  the amplitude. In other words, EIS measures the signal difference between the input and the output in terms of magnitude and phase.

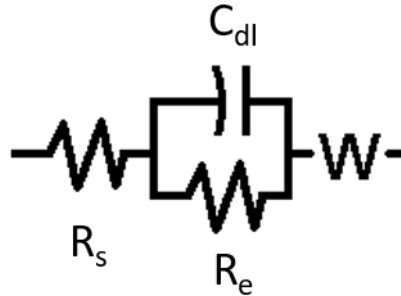


Figure 1: Randle's Circuit

As a whole, the system is a combination of multiple reactions of varying kinetics, each of which can be compared to the behavior of electrical circuit components, and modeled by resistive or capacitive elements<sup>120</sup>. The most commonly used equivalent circuit to model EIS data is the Randles circuit (Figure 1), consisting of an overall solution resistance in series with the parallel combination of a charge transfer resistance, capacitive double layer and Warburg diffusion element<sup>120,121,134,135</sup>. Each element in the system attributes some degree of obstruction to current flow through the system, thus influencing the output signal. The simplest electrochemical equivalent circuit component is the purely resistive approximation of the solution resistance ( $R_s$ ). The presence of electroactive analytes in solution contribute a degree of resistivity or conductivity to current flow through the cell. Large, non-polarizable molecules are intrinsically resistive by nature. This behavior can be modeled by a frequency-independent resistance, termed solution resistance, and is influenced by the ionic content of the solution, as well as the geometry of the conducting cell<sup>97</sup>. Correspondingly, the Warburg impedance ( $W$ ) is also descriptive of bulk solution properties, and is perhaps the most established and empirically validated circuit modeling component in electrochemistry<sup>136</sup>. The Warburg impedance component stems from the diffusion-

based transport of the electroactive analyte to the electrode surface. This is commonly dependent upon the respective analyte diffusivity, concentration gradient within the cell, and separation between the bulk solution and near field <sup>120,136</sup>.

Two additional elements, charge transfer resistance ( $R_{et}$ ) and double layer capacitance ( $C_{dl}$ ), are also included in a Randles circuit model, and are preferentially used as descriptors of immunosensors stemming from the impedance spectroscopy technique and molecular interactions. Charge transfer resistance permits investigation into the kinetics of the reaction occurring at the electrode-solution interface. As the name suggests, the movement of electrons between phases introduces a resistive element to the circuit. In the context of immunosensors this can be best described in relation to the molecular interactions occurring at the electrode surface. Upon analyte binding, high molecular weight complexes are formed, which act as barriers to the redox-mediated flow of electrons through the system. Supplementing the molecular binding phenomenon, regions of charge separation exist within the cell, analogous to a capacitor in an electrical circuit. The analytes in solution contain charged groups. Upon specific binding to the antibody receptor site, an accumulation of charge is observed at a specified distance from the electrode surface. The separation of charge, and thus equivalent capacitance is dictated by the dielectric layer, or the immobilization chemistry used to functionalize the sensor surface. In order to maximize capacitance and therefore sensitivity, the dielectric should be uniform, free of impurities, and exist across a short distance<sup>120</sup>. Unfortunately, perfect dielectric layers are improbable due to the inhomogeneity of electrode surfaces and permeation of ions and water molecules through the layer. Therefore, constant phase elements are often used instead of  $C_{dl}$  to represent the imperfect parallel plate capacitors<sup>135</sup>.

## NOVEL ALGORITHM FOR OPTIMAL FREQUENCY

### OVERVIEW OF OPTIMAL FREQUENCY

Although equivalent circuit modeling gives a system-wide evaluation, the impedance responses at individual frequencies are not analyzed. Therefore, equivalent circuit modeling does not lead to the identification of an optimal frequency. To identify the optimal frequency, two components of the impedance responses at individual frequencies can be utilized: complex impedance and phase angle.

$$Z' = |Z|\cos(\phi) \quad \text{Equation 5}$$

$$Z'' = |Z|\sin(\phi) \quad \text{Equation 6}$$

where  $Z'$  is the real impedance,  $Z''$  the imaginary impedance,  $\phi$  the phase angle, and  $Z$  the complex impedance. Since each impedance spectrum ( $Z'$ ,  $Z''$ ,  $Z$ , and  $\phi$ ) can be utilized to derive the optimal frequency, the overwhelming amount of data prompted various ways of analysis algorithms. In the following section, the author discusses a few common computing algorithms and their associated impedance components found in the literature.

#### *Maximum Response*

The simplest algorithm to calculate the optimal frequency is to observe the frequency at which the signal change is largest. In this approach, complex impedance is often used as the source of signal<sup>131,137-142</sup>, but phase angle can also be used as well<sup>143</sup>. This approach has been the most heavily used and published since the emergence of the optimal frequency phenomenon.

Generally, following immobilization of the target analyte's molecular recognition element, the optimal frequency can be determined by depositing a gradient of target analytes onto the sensor and identifying the frequency at which the highest percent change in impedance occurs.

Additional criteria such as the shortest response time among frequency candidates can be applied, but generally follow the same principle<sup>141,142</sup>. The optimal frequencies identified with this algorithm can shift drastically depending upon the testing conditions employed, suggesting that



the optimal frequency is representative of an equilibrium of an electrochemical system instead of the specific biomarker. Although permitting accurate detection of target analytes in various media, programming a POC diagnostic tool with a specific frequency (i.e. the optimal frequency) may yield inaccurate results due to inconsistencies among patient samples. This is largely a result of solution-dependent changes in electrochemical properties. When the testing solutions are altered, the electrochemical properties are also altered, leading to changes in descriptive parameters such as the charge transfer resistance or solution resistance, and consequently the optimal frequency. When using this algorithm, the derived optimal frequency represents the combination of signal generated from the target-MRE binding reactions and the background noise resulting from the surrounding medium composition. However, because of the simplicity and straightforward nature of this algorithm, it is suitable for investigational and characterization purposes.

#### *Maximum Correlation*

Another commonly used algorithm determines the optimal frequency through the maximum correlation, which is typically represented by R-square (RSQ) values<sup>132,144</sup>. RSQ value is one of the many parameters in a linear model obtained by fitting the dependent variable to the independent variable. It is a measure of goodness-of-fit between the model and the dependent variable. In EIS, by fitting the empirical impedance values to the known analyte concentration across the frequency spectrum, a linear model described by slope and RSQ parameters is obtained at each discrete frequency. In the maximum correlation algorithm, the optimal frequency is the frequency at which the RSQ value is highest. It also often relies on the complex impedance as the source of signal<sup>132,144</sup>.

Although a high RSQ value is generally desirable because it indicates sufficient agreement between the predicted model and the real data, it has limitations. A linear model with high RSQ value can be biased, and therefore a residual plot is often required to validate the model. Another

limitation is that, in EIS, it is possible that a range of frequencies all exhibit high RSQ values (> 0.95), making it hard to identify a single candidate to serve as the optimal frequency of the biomarker. Relying only on high RSQ values, alone can also have false positives, such as a flat-line response where the RSQ is high but the slope is significantly small. These scenarios indicate minimal detectable signal change between analyte concentrations, which can be masked by the error associated with measurement.

### *Transfer Functions*

Another category of algorithms is the transfer functions that take both the response and correlation into considerations. Generally, there is a tradeoff between the slope and RSQ values, as the frequency with highest RSQ is often not the frequency with the highest slope. To determine the optimal frequency, transfer functions can be adapted to permit complex design of algorithms for determining the optimal frequency<sup>130,145</sup>. The transfer function can also be used on the impedimetric responses to convert them into different parameters. For example, by employing the following transfer functions defined by Equations 7-9, the impedance values can be converted to.

$$C = \frac{1}{j\omega Z} \quad \text{Equation 7}$$

$$Y = j\omega C \quad \text{Equation 8}$$

$$M = \omega Z \quad \text{Equation 9}$$

where  $\omega$  the angular frequency, C the capacitance, Y the admittance, and M the modulus.

Optimal frequencies can also be calculated by finding the frequency at which the capacitance, admittance, or the modulus is largest with sufficiently high RSQ<sup>146</sup>. A summary of algorithms and the EIS components used to determine the optimal frequency is summarized in Table 3.

frequency. The number inside each cell represents the reference number.

	Max. Response	Max. Correlation	Transfer Function
Complex Impedance	131,137-142	132,144	130,145
Phase Angle	143		146
Real Impedance			146
Imaginary Impedance	<sup>13</sup> (author's work)	<sup>9</sup> (author's work)	<sup>1</sup> (author's work)

Table 3: Summary of EIS algorithms and the EIS components used to determine the optimal

## THE IMAGINARY IMPEDANCE ALGORITHM

Depending on the algorithm used, the electrochemical signals may consist of large full width half maximums (FWHM), causing severe signal overlays at each biomarker's optimal frequency, and thus prevents the execution of multi-marker detection. One example can be found in the complex impedance algorithm. When plotting the slope and RSQ values against the frequency spectrum, complex impedance algorithm often yields highest response at low frequencies (Figure 2). While this is not an issue for single biomarker detection, the abundance of signal from one biomarker's

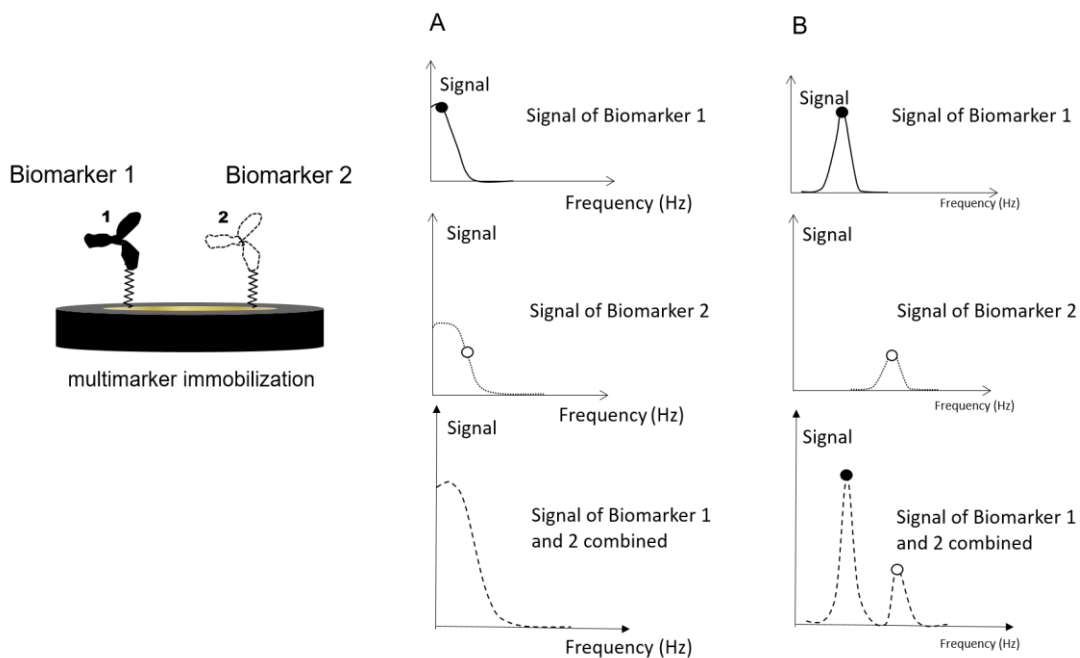


Figure 2: Differences Between Complex and Imaginary Impedance Algorithms. Schematic representation of 2 biomarker's impedance signals and the predicted signal when co-immobilized on the same sensor. Each biomarker's optimal frequency is determined by sensitivity and RSQ using A) complex impedance and B) imaginary impedance. The black circle represents the optimal frequency of biomarker 1 and white circle the optimal frequency of biomarker 2 in each approach. Notice that in Figure 1A, due to signal overlapping, the optimal frequencies of both markers are not distinguishable when co-immobilized. Reprint with permission from reference 1.

optimal frequency can overlap with the signal from another biomarker's optimal frequency, posing a great challenge for multi-marker detection.

On the other hand, the imaginary impedance algorithm offers an additional parameter for the determination of optimal frequency: peak location, which is also known as the cutoff frequency. In contrast to complex impedance, imaginary impedance peaks at a specific frequency, forming a parabolic shape when plotted across frequencies. By correlating the imaginary impedance to target concentration, the optimal frequency of a biomarker can be identified (Figure 3). Typically the highest slope will accompany with a very high RSQ (Figure 3B), making the identification of optimal frequency much simpler. A more detailed investigation of optimal frequency using the imaginary impedance algorithm can be found in chapter 3.

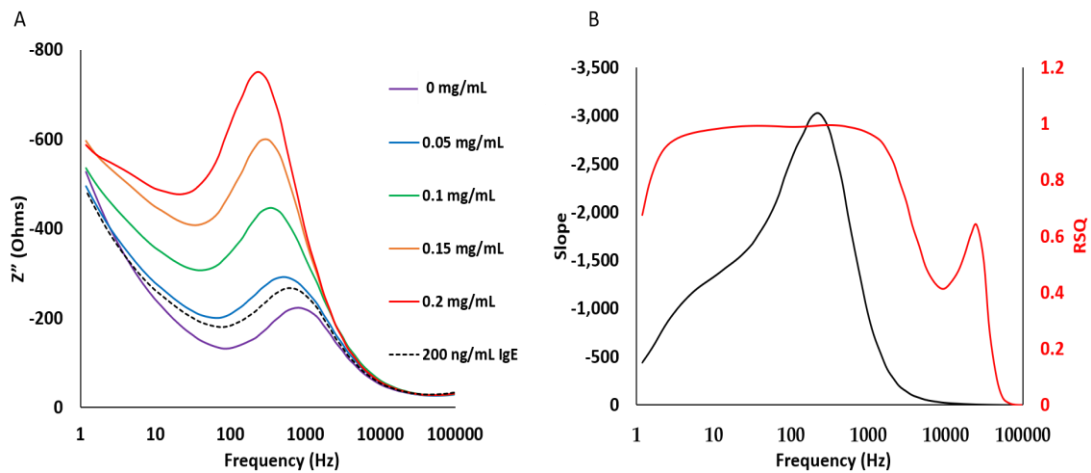


Figure 3: Typical Imaginary Impedance Responses. A) the overlay of imaginary impedance and the shifting of cut-off frequencies and B) the optimal frequency at 57.44 Hz where the slope peaks with very high RSQ.

#### *The Comprehensiveness of the Imaginary Impedance Algorithm*

One may argue that the imaginary impedance algorithm is only a snap shot of the electrochemical system and can potentially miss vital data, causing inaccuracies in the

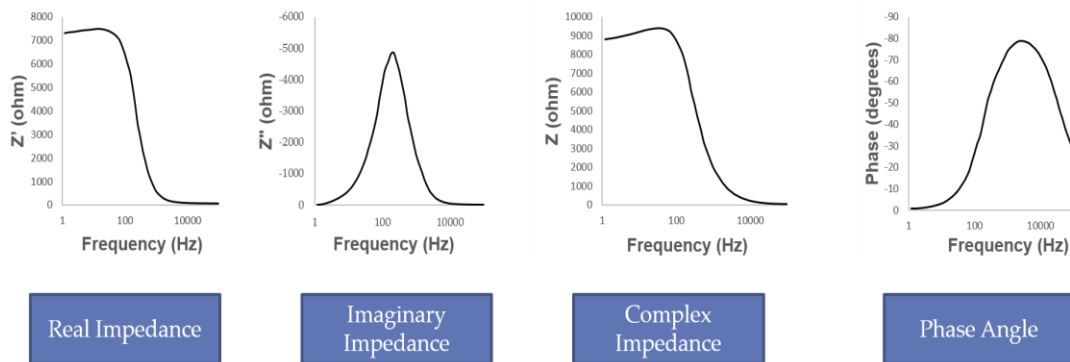


Figure 4: The four main impedance components of EIS.

measurement. In reality, the imaginary impedance can be considered as a more filtered signal that still represents the entire system. It can be seen from Equation 6 that the imaginary impedance is derived from both phase angle and complex impedance, which represent the whole system. Similarly, as seen in Equation 5, real impedance is also derived from the whole system. However, as shown in Figure 4, the signal pattern of real impedance is like that of complex impedance as they both resemble the response of a low-pass filter, suggesting a potential signal overlap if the optimal frequency is at the lower frequency range. Although phase angle is similar to the imaginary impedance in that they both have a distinct peak, its FWHM is higher than that of imaginary impedance, increasing the risk of signal overlap if the two optimal frequencies are close to each other. Therefore, the imaginary impedance algorithm not only preserves the vital information from the system, it also has the lowest risk in signal overlap, and is thus selected as the basis for determining the optimal frequency.

## THE SIGNAL DECONVOLUTION ALGORITHM

To decouple the signal generated from two biomarkers co-immobilized onto the same sensor surface, a unique decoupling algorithm is applied and described below. All impedance values are imaginary impedance.

Generally, the calibration curve at each frequency is typically expressed in the form of:

$$y(f) = m(f) * x + b(f) \quad \text{Equation 10}$$

where  $y$  is the imaginary impedance,  $m$  is the slope,  $x$  is the target concentration,  $f$  is the frequency, and  $b$  is the intercept.

The term  $b(f)$  can be interpreted as a baseline adjustment value, which can vary in different sensor configurations and surface topography's. The slope,  $m(f)$ , can be considered as the main signal generated from the binding of target molecules to their MREs including the association and dissociation rates. Using this concept, it can be argued that the dual marker co-immobilized data has three components: the resulting imaginary impedance ( $y(f)$ ), the impedance signal (slope) resulted from the 2 biomarkers ( $m(f) * x$ ), and the baseline adjustment impedance ( $b(f)$ ), described as:

$$y_{1,2}(f) = m_{1,2}(f) * x_{1,2} + b_{1,2}(f) \quad \text{Equation 11}$$

where 1 denotes biomarker 1 and 2 biomarker 2. If the pattern of  $b(f)$  in the co-immobilized setup can be modeled, then the impedance values caused by  $b$  can be subtracted from the overall co-immobilized impedance values. The remaining impedance values across all frequencies are then the decoupled impedance values resulted from the binding of 2 biomarker molecules to their corresponding antibodies. Depending on the concentration of antibodies, weighting multipliers may be considered.

XLfit, an Microsoft Excel add-on for parabolic fitting, was used to model the parabolic curves that were generated from plotting imaginary impedance ( $y(f)$ ) against frequencies and slopes ( $m(f)$ ) against frequencies. The parabolic fitting was performed on both purified biomarker 1 and

biomarker 2 to model their electrochemical responses ( $m_1(f)$  and  $m_2(f)$ ). The projected impedance values ( $y'_1(f)$  and  $y'_2(f)$ ) without the adjustment values ( $b_1(f)$  and  $b_2(f)$ ) were then obtained by multiplying the parabolic fitting of biomarker 1 and biomarker 2's slopes ( $m_1(f)$  and  $m_2(f)$ ) with their target concentrations ( $x_1$  and  $x_2$ ). The projected impedance values of biomarker 1 and biomarker 2 ( $y'_1(f)$  and  $y'_2(f)$ ) were then added together to project the impedance values of co-immobilized biomarker 1 and biomarker 2 ( $y'_{1,2}(f)$ ) without the adjustment values ( $b_{1,2}(f)$ ). The adjustment values ( $b_{1,2}(f)$ ) were then obtained by subtracting the predicted co-immobilized impedance values ( $y'_{1,2}(f)$ ) from the actual co-immobilized impedance values ( $y_{1,2}(f)$ ). After modeling the adjustment values ( $b_{1,2}(f)$ ), the projected adjustment values ( $b'_{1,2}(f)$ ) at each frequency can be obtained. Lastly, by subtracting the projected adjustment values ( $b'_{1,2}(f)$ ) from the actual co-immobilized impedance values ( $y_{1,2}(f)$ ), the decoupled impedance values resulted from only the binding of biomarker 1 and biomarker 2 could be obtained. A new calibration curves for each biomarker were then obtained to detect biomarker 1 and biomarker 2 separately, as demonstrated in the detection of LDL and HDL discussed later. See International Patent #: PCT/US/2018/023375 and U.S. Patent Application # 62/473,894 for more details.

### *Summary*

Overcoming signal overlaps when two biomarkers have similar optimal frequencies is a top priority in succeeding multi-marker detections. In this chapter, a novel algorithm of determining a biomarker's native optimal frequency is reported. A signal deconvolution algorithm is also reported to overcome signal overlapping. Without the imaginary impedance algorithm, the overlapping signal could be too much to deconvolute. By applying this algorithm, the following chapters will discuss its utility in achieving single marker and multimarker detections that are otherwise challenging to perform.

*Acknowledgement:* The contents in this chapter is adapted from the author's published work<sup>1,9</sup> and submitted works<sup>11,13</sup>. The author is the first author on all 3 manuscripts and have contributed to the

work in every aspect, ranging from designing the experiments, analyzing the results, and writing the manuscripts. The author would also like to thank Dr. Jeffrey LaBelle for guidance and mentorship. The author would also like to thank David Probst, Mackenzie Honikel, Dr. Michael Caplan and Dr. Mark Spano for intellectual support. The contents in this chapter received permission to be reproduced from the coauthors and publishers. The author has filed a U.S. provisional patent application (62/473,894) to protect the content of this chapter.



## CHAPTER 2.1

### A DUAL-MARKER PROTOTYPE: TWO ANTIBODIES

#### INTRODUCTION

Although hypothesized previously, a physical prototype demonstrating EIS's utility in multi-marker detection has yet been developed. As described in previous chapter, imaginary impedance ( $Z''$ ) algorithm has the potential to overcome signal overlapping, allowing the detection of multiple biomarkers simultaneously on a single electrode. However, to achieve the multimarker detection, one must recognize the distinct differences between the affinity-based binding and the enzymatic reaction in EIS. Figure 5 shows the electron flows in the enzymatic reaction and the affinity-binding reactions. In the enzymatic reactions, analytes are oxidized, and consequently the electrons are generated. The electron mediators then carry the electrons to the electrode, generating an observable signal. When all the electron mediators or the substrates in the system are consumed, the electron facilitation stops, and the signal is lost. This is especially evident in continuous glucose meters, where wound healing process can eventually cover the glucose sensor to a point that oxygen, the primary electron receptor in first generation glucose sensors, is no longer permeable from blood onto the sensor<sup>8</sup>. On the contrary, affinity based binding does not generate electron flow. Instead, the antibody-antigen complex serves as an obstruction to the electron flow. Although enzymatic or other electroactive labels can be added to the analytes to create a signal when binding occurs, it defeats the purpose of developing a label-free electrochemical sensor. One interesting alternative worthy of mentioning is a molecular engineering approach by adding an electron mediator probe onto a MRE that undergoes drastic conformational change when binding occurs, such as a tentacle probe<sup>147</sup>. This way, after MRE-target binding, the electron mediator probe can change location relative to the sensor surface, generating a differential electrochemical signal.

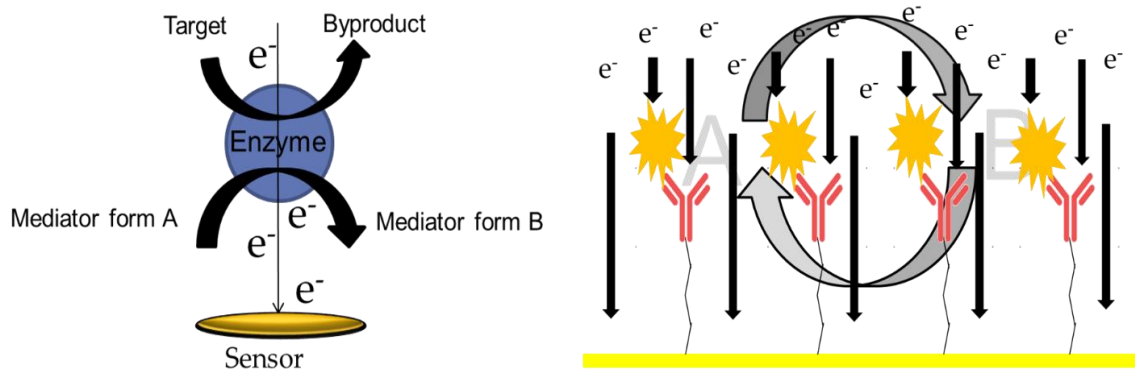


Figure 5: Electron flows between an enzymatic reaction and an affinity-binding reaction. A and B represents the oxidized and reduced form of an electron mediator. In the enzymatic reaction (left), a signal is generated from the oxidation of product to byproduct. In the antibody-binding reaction, the signal comes from the blockage of electrons with regard to antibody-antigen binding.

To detect a “signal” after the antibody-antigen complexes are formed in a label-free manner, the concept of formal potential is adopted. The formal potential is the average between the oxidation voltage and the reduction voltage (Figure 6). At the formal potential, the electron mediators are constantly converted back and forth, facilitating the electrons like a quiet engine. This way, electron blockage (thus termed impedance) with respect to antibody-antigen complexes can be measured, providing a label-free method to measure target analytes.

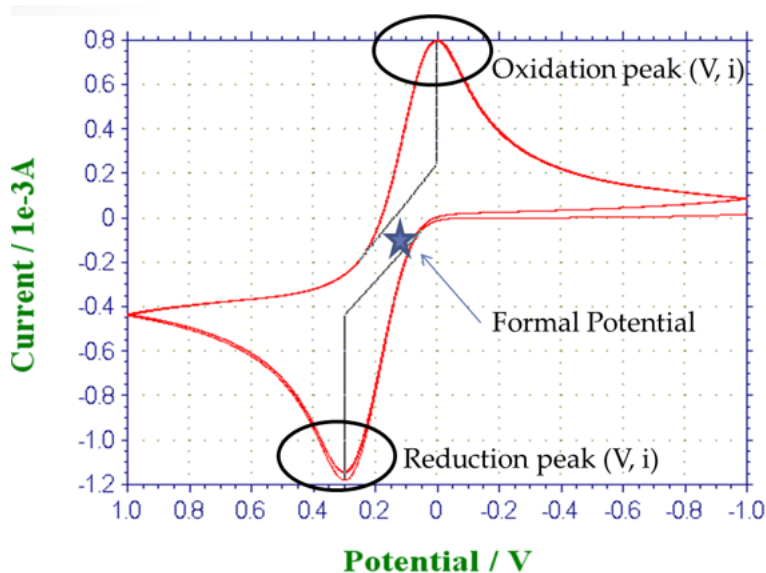


Figure 6: Determining the formal potential with cyclic voltammetry

To develop functional prototypes of the multimarker sensor, 3 dual-marker prototypes were developed. Each prototype was designed to investigate a combination of the detection mechanisms: antibody + antibody (A+A), enzyme + enzyme (E+E), and antibody + enzyme (A+E). The selection of biomarkers was discussed in Chapter 1. For the A+A prototype, two example biomarkers that utilize the antibody-antigen binding mechanism were investigated: low-density lipoprotein (LDL) and high-density lipoprotein. The two biomarkers not only have strong clinical value as described in Chapter 2.1, but also have biological characteristics suitable for multi-marker investigation. The MRE of both biomarkers are similar: IgG monoclonal antibody, which permits a similar baseline. The LDL and HDL antigens differ drastically in size (175kDa and 512 kDa, respectively), allowing them to be differentiated. In this chapter, we investigate the feasibility of detecting 2 antibody-based biomarkers while developing a dual-marker biosensor for monitoring 2 key biomarkers of CVD, a major comorbidity of DM.

## METHODS

A standard sensor preparation protocol utilizing the gold-disc electrodes (GDE) and the self-assembled monolayer was used in this study. For more details, please refer to the Appendix B.

To characterize the individual biomarker's signal, 50 ug/mL of either LDL or HDL antibodies were immobilize on the GDEs via covalent binding between primary amines of the antibody and carboxylic groups of the self-assembled monolayer. Single-marker sensors were first built using 50 ug/mL of respective antibodies. To build the dual-marker sensor, 50 ug/mL of LDL and HDL antibodies were co-immobilized onto the GDEs. All sensors were brought to room temperature prior to testing. A Serial dilution made in PBS was used to prepare purified LDL and HDL samples from 50 – 0 mg/dL. For LDL and HDL co-immobilization testing, the two markers were well mixed at a 1:1 ratio in a similar manner and the mixture has the concentration of 0-10 mg/dL for each biomarker. Antibody concentrations were still kept at 50 ug/mL in co-immobilization setting. EIS was performed to measure each sample's impedance at each sensor's formal potential from 1 Hz to 100 kHz at 12 points per decade in the presence of 100 mM potassium ferricyanide (see Appendix D for details). The imaginary impedance algorithm described previously was used to determine the optimal frequency. The signal deconvolution algorithm described previously was used to deconvolute the coimmobilized signal. All electrochemical circuit modeling was done via ZSimpWin (Echem Software, USA). EIS data was fit against potential electrochemical equivalent circuit models and evaluated using a Chi-square analysis and mean percent standard deviation (see Appendix F for details). The procedure was repeated to obtain the best fitting electrochemical equivalent circuit for purified LDL, purified HDL, and co-immobilized LDL and HDL.

## RESULTS

### *Electrochemical Verification of Self-Assembly Monolayer and Target Binding*

For quality control, AC impedance measurement was performed 3 times throughout the sensor preparation process: after polishing the bare electrodes, after MHDA, and after blocking. As shown in Figure 7a, a clean electrode showed only a Warburg tail, suggesting that the system is dominated by diffusion. Damaged or warped GDE's will have much higher impedance after polishing. As shown in figure 7b and 7c, the impedance will increase drastically after successful

MHDA binding and decrease after successful immobilization of MREs. When targets were introduced to the sensors, the impedance increased significantly from the blank, suggesting successful binding. The specificity of binding and surface coverage were evaluated in previous work<sup>148</sup>. Notice that the bare electrode impedance values are a hundred times smaller than the impedance values when binding occurs, suggesting that the cables have negligible effects on the measurements.

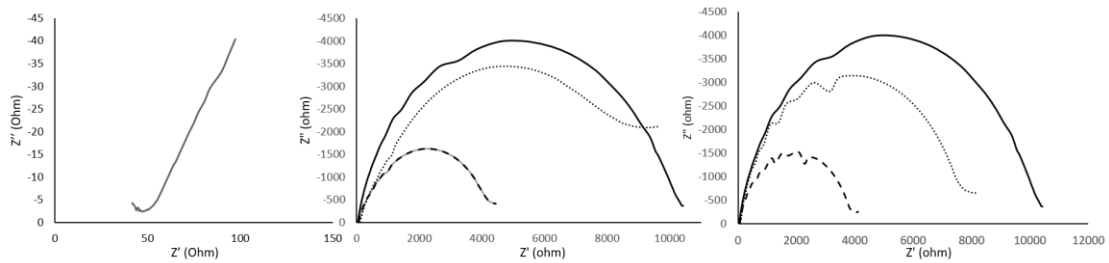


Figure 7: Nyquist plots for LDL and HDL sensors. a) Bare gold disk electrode. b) 16-MHDA (solid line), blank (thick dashed line) and 10 mg/dL HDL (light dashed line). c) 16-MHDA (solid line), blank (thick dashed line) and 10 mg/dL HDL. Reprinted with permission from reference 1. © Elsevier.

#### *Electrochemical Characterization of Purified LDL and HDL*

The EIS responses of LDL and HDL in imaginary impedance (Figure 8a and 8b) exhibit distinct peaks at various frequencies, resembling a bandpass filter-like shape. In contrast, the complex impedance (Figure 8c and 8d) does not exhibit the distinct peaks and resembles a shape like a low-pass filter. The optimal frequency was calculated by choosing the frequency with highest slope and satisfactory RSQ (>0.85). Using the imaginary impedance approach, the optimal frequencies of LDL and HDL were found to be at 81.38 Hz and 5.49 Hz, respectively (Figure 8a and 8b). Using the complex impedance approach, the optimal frequency of HDL could be found at 1.18 Hz. However, the optimal frequency for LDL could range from 1.18 Hz to 37.56 Hz as the tradeoffs between slope and RSQ are difficult to evaluate. Using the imaginary impedance approach, the calibration curve at each biomarker's optimal frequency was attained by graphing the concentration versus output imaginary impedance and fitted to a regression line. The

calibration curve for LDL at an optimal frequency of 81.48 Hz is described as  $y = -106.7 \ln(x) - 2881.5$  (Figure 8e, black curve) with an RSQ of 0.92. The calibration curve for HDL at an optimal frequency of 5.49 Hz is described as  $y = -238.16x - 783.11$  with an RSQ of 0.97 (Figure 4e, grey curve). The dynamic ranges for LDL and HDL sensors are 35.78 mg/dL – 211.22 mg/dL and 42.43 mg/dL – 172.65 mg/dL, respectively, with both encompassing the clinically relevant range of 100 - 190 mg/dL and 40-60 mg/dL, respectively <sup>149</sup>. Note that LDL was found to have a logarithmic fit while HDL a linear fit. The association and disassociation rate constants for LDL are  $342 \text{ nM}^{-1} \cdot \text{min}^{-1}$  and  $27 \text{ min}^{-1}$ , respectively, and HDL  $90 \text{ nM}^{-1} \cdot \text{min}^{-1}$  and  $3 \text{ min}^{-1}$ , respectively <sup>71</sup>.

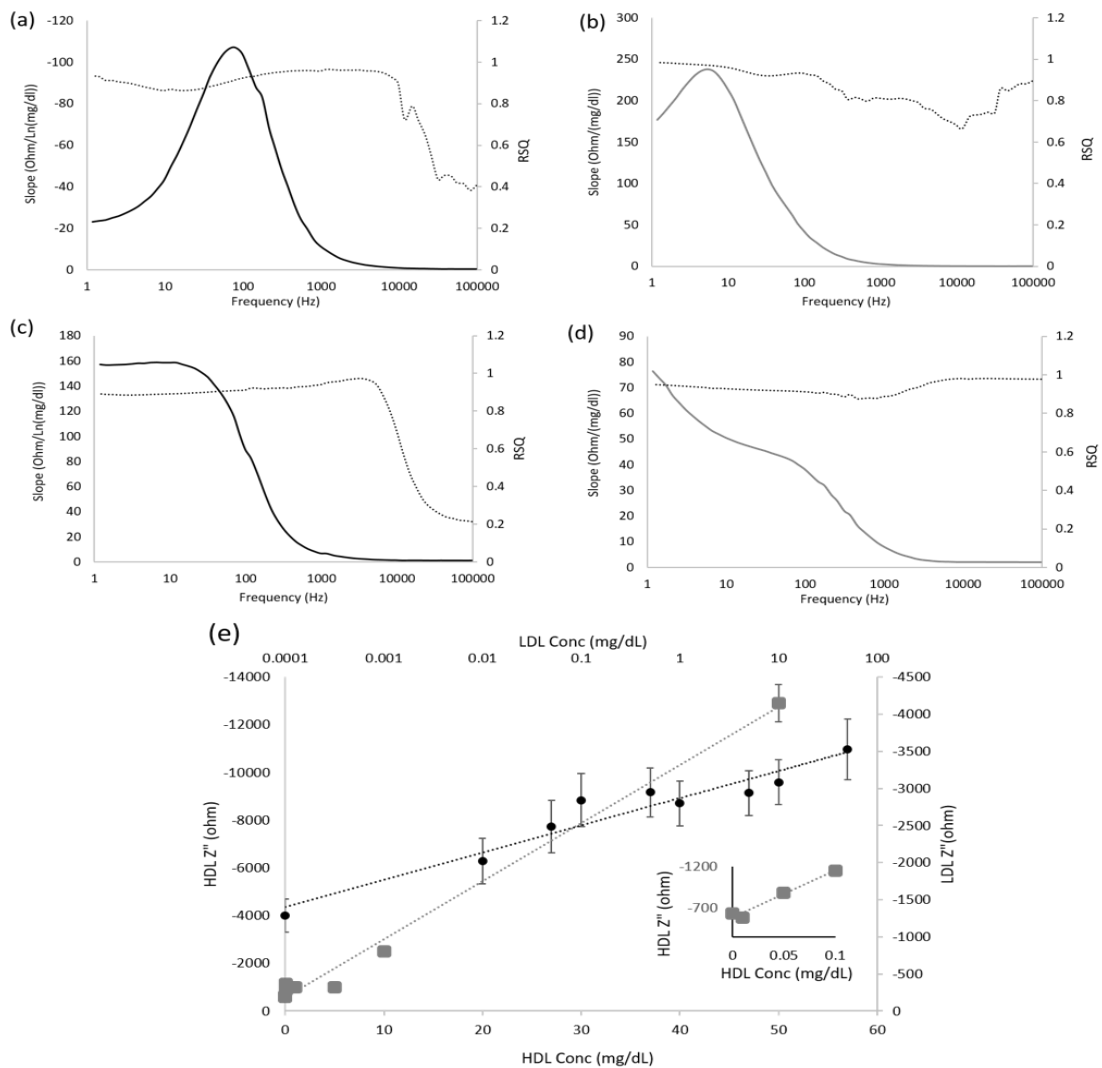


Figure 8: Electrochemical characterization of LDL (black) and HDL (grey) in purified solution. The imaginary impedance slope is overlaid with RSQ (dashed line) across the frequency sweep for: (a) purified LDL and (b) purified HDL. The complex impedance slope is overlaid with RSQ across the frequency sweep for: (c) purified LDL and (d) purified HDL. Using the imaginary impedance approach, (e) shows the overlay of the LDL (black) and the HDL (grey) calibration curves at each marker's optimal frequency over the concentration range tested (0-50 mg/dL for both). The inset is a zoomed-in view of the HDL slope from 0 to 0.1 mg/dL. Reprinted with permission from reference 1. © Elsevier.

### *Detection of LDL and HDL in Co-immobilized Setup*

The co-immobilized impedance signal of LDL and HDL shows a similar bandpass filter shaped peak at 31.5 Hz with a strong correlation. Knowing that the peaks in purified LDL and HDL are 81.38 Hz and 5.49 Hz, respectively (Figure 8a and 8b), the summation of the two signals when co-immobilized can theoretically yield a single peak that is within the two frequencies (Figure 9a). Note that the RSQ value of 1 with little to no slope at frequencies above 10 kHz shows the lack of signal above 10 kHz. Once the signal was decoupled using the algorithm described above, two peaks became apparent (Figure 9b). The decoupled HDL peak shifted slightly from 5.74 Hz to 3.74 Hz with a slope of 199.4 ohm/(mg/dL), and correlation of 0.99. The decoupled LDL peak shifted from 81.38 Hz in purified to 175.8 Hz with a slope of 57.15 ohm/(mg/dL) and a correlation of 0.88. The slopes were then used to generate new calibration curves that can back-calculate the LDL and HDL concentrations. The results were then plotted against the reference concentrations (Figures 9c, 9d) for verification. The lower limit of detection for the multi-marker sensor is 1 mg/dL but upper limit of detection still requires further optimization. Note that Figure 9c and 9d's scale bars have been adjusted to show only the linear range of the decoupled signal.



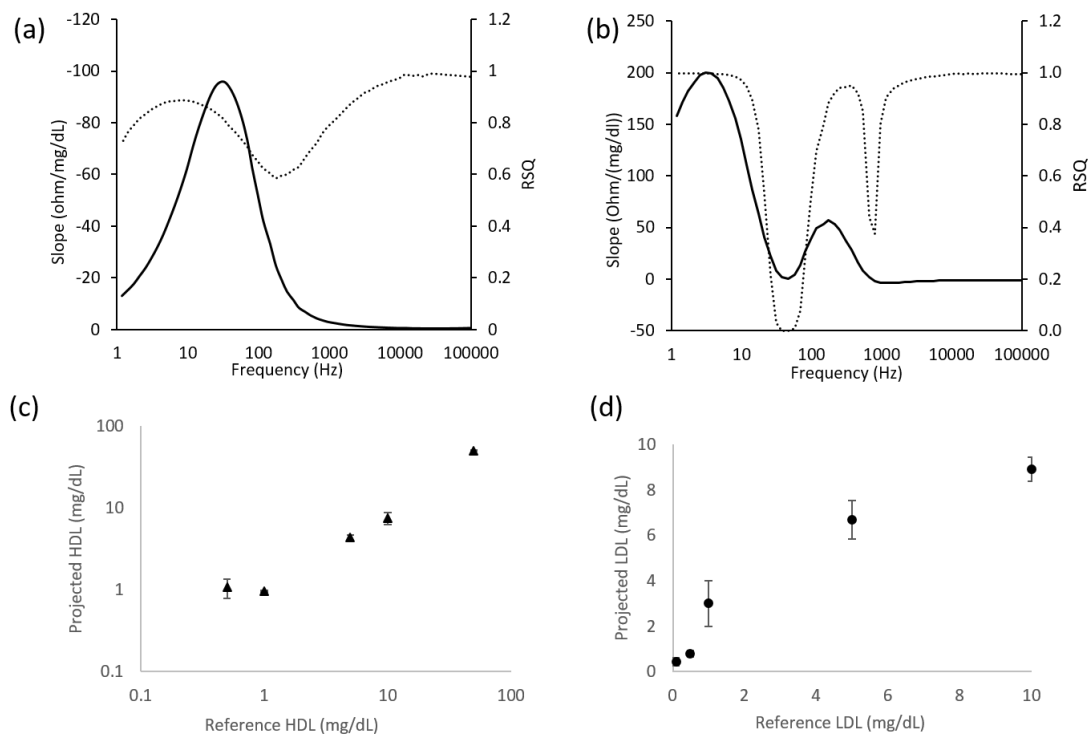


Figure 9. Co-immobilization of HDL and LDL. (a) raw data plotting the slope (solid line) and RSQ (dashed line) across frequency sweep, with a unique peak at 31.5 Hz; (b) The decoupled signal using the described algorithm. The two peaks occur at 3.74 Hz and 175.8 Hz, with each representing the optimal frequency of HDL and LDL, respectively. The RSQ also peaks at these frequency locations; (c) The comparison of the predicted HDL values using the calibration curve, versus the actual input values. (d) The comparison of the predicted LDL values using the calibration curve, versus the actual values. Reprinted with permission from reference 1. © Elsevier.

### Electrochemical Equivalent Circuits

The electrochemical equivalent circuits for LDL and HDL were both found to be the  $R(QR)$  circuit, which can be considered a modified Randle's circuit ( $R_s(Q[R_{ct}W])$ ) (Figure 10). This modeling is consistent with the theory that electrical properties of proteins can be considered as a resistance-capacitance parallel circuit<sup>150,151</sup>. The CPE represents an imperfect double layer capacitor

consisting of the electrode, the SAM, MREs, and bound target molecules. The impedance of CPE ( $Z_{CPE}$ ) is described as:

$$Z_{CPE} = \frac{1}{Q(j\omega)^n} \quad \text{Equation 12}$$

where  $j = (-1)^{\frac{1}{2}}$ ,  $\omega = 2\pi f$  with  $f$  being the frequency of the applied AC potential, and  $n$  representing a fractional value between 0 to 1, with 0 describing a pure resistor and 1 an ideal double layer capacitor<sup>152</sup>. The values of individual components in LDL's equivalent circuit are:  $R_s=239$  ohms,  $Q=1.66E-7$  Ssec<sup>n</sup>/cm<sup>2</sup>,  $n=0.87$ ,  $R_c=21701$  ohms. The values for HDL's equivalent circuits are:  $R_s=211$  ohms,  $Q=6.69E-7$  Ssec<sup>n</sup>/cm<sup>2</sup>,  $n=0.8$ ,  $R_c=30015$  ohms.

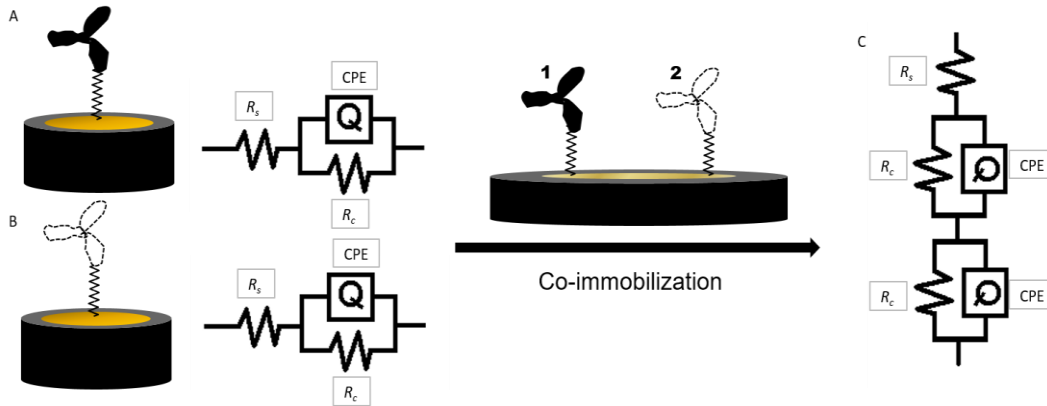


Figure 10: Electrochemical equivalent circuits for purified LDL (A), HDL (B), and co-immobilized LDL and HDL (C). ( $R_s$ ) = solution resistance; ( $R_c$ ) = a combined resistance of charge transfer resistance ( $R_{ct}$ ) and Warburg impedance ( $W$ ); ( $Q$ ) = constant phase element (CPE). Reprinted with permission from reference 1. © Elsevier.

The equivalent circuit model of co-immobilized LDL and HDL was found to be a combination of individual LDL and HDL equivalent circuits:  $R(QR)(QR)$ . While it is possible to model the co-immobilized LDL and HDL with the same  $R(QR)$  circuit, the chi-square and mean % stdev of  $R(QR)(QR)$  circuit ( $4.97E-04$  and  $2.01\%$ , respectively) are much smaller than that of  $R(QR)$  circuit ( $1.49E-03$  and  $3.85\%$ , respectively), suggesting a much better fit. The values for co-immobilization's equivalent circuits are:  $R_s=101$  ohms,  $Q_1=1.73E-4$  Ssec<sup>n</sup>/cm<sup>2</sup>,  $n_1=0.6$ ,  $R_{c1}=7966$  ohms,  $Q_2=2.07E-4$  Ssec<sup>n</sup>/cm<sup>2</sup>,  $n_2=0.8$ ,  $R_{c2}=9673$  ohms.

## DISCUSSION

### *The Use of Imaginary Impedance in Biomarker Detection.*

The greatest challenge of measuring two biomarkers using a single co-immobilized sensor is the large amount of signal aliasing. As seen in Figure 8c and 8d, using the complex impedance approach can pose a great challenge for signal decoupling and back-calculation of target concentrations when applied in multi-marker detection settings. However, with the distinct peaks and higher RSQ values obtained using the imaginary impedance approach, individual signals are easily distinguished. The peak also makes determining optimal frequency much easier than in the complex impedance approach. Similar to how many researchers correlated target concentration with electron transfer resistance and omitted solution resistance, using just the imaginary impedance allows researchers to focus on the capacitive signal resulted from the conformational changes of target-MRE binding. By using the decoupling algorithm, it is possible to detect two biomarker simultaneously on the same sensor. Based on these unique characteristics, the imaginary impedance approach better suits the characterization of multi-marker detection, while the complex impedance approach is more specific to single-marker detection.

### *Potential Connection between Optimal Frequency and Biomarkers' Properties*

LDL is approximately 22 nm to 27.5 nm in diameter<sup>153</sup> and HDL 7.3 – 13 nm<sup>154</sup>. Given that, it is interesting to note that LDL was detected at a higher frequency (81.38 Hz) and HDL at a lower frequency (5.49 Hz) in purified solution (Figure 8a and 8b), suggesting a potential relationship between optimal frequency and molecular size. Targets with various sizes can bind to their MREs to form size varying complexes, affecting the capacitance of the IPPC and consequently the optimal frequencies. The association and disassociation rates of HDL (342 nM<sup>-1</sup>.min<sup>-1</sup> and 27 min<sup>-1</sup>) are also much higher than that of LDL (90 nM<sup>-1</sup>.min<sup>-1</sup> and 3 min<sup>-1</sup>), suggestion potential connection to optimal frequencies as well.

This phenomenon helps explain the shift in frequencies after co-immobilizing the two biomarkers. After co-immobilization the optimal frequencies of LDL and HDL (5.48 Hz and 81.38 Hz, respectively) shifted to 3.74 Hz and 175.8 Hz, respectively. Note that the CHI660C is only capable of measuring 12 frequencies per decade and 81.38 Hz is 4 data points away from 175.8 Hz, suggesting a higher resolution might be desirable for future investigation. Parameters that may have influenced the shift in optimal frequencies are steric hindrance, molecular diffusion rates, as well as orientation and shape of the MRE-target complex. Other factors such as binding kinetics; the association and dissociation rates; the physical changes that occur during binding; and whether the mechanism is 1 step or multistep process can all have impacts as well. These factors can affect the electron transfer rate and the capacitance of the IPPC despite the immobilization of the two markers' antibodies at a 1-to-1 ratio. Future experiments will be conducted to evaluate the effect of each factor on optimal frequency and develop a more robust model in estimating the optimal frequencies. While it appears that both biomarkers can be detected simultaneously on the same sensor, optimization experiments such as altering the ratio of LDL and HDL antibody concentrations, EDC/NHS concentrations, and 16-MHDA concentration should also be performed to mature the platform for testing in complex solutions.

## CONCLUSION

While EIS has been previously reported to have the theoretical capability of multi-marker detection on a single sensor, one of the major roadblocks to a successful multi-marker sensor has been the signal overlapping and decoupling. Here we report the first step toward multi-marker detection by detecting LDL and HDL simultaneously on GDEs. We report a novel signal analyzing approach using just imaginary impedance, a signal decoupling algorithm, and discuss factors that may affect optimal frequencies. This is the first demonstration that EIS has the potential for multi-marker detection in a label-free manner. This work does not discuss the MRE orientation, biomarker's physical structure, binding mechanisms, and many other factors that may affect optimal frequency in great depth. No optimization and interference testing have been performed

on the multi-marker sensor. These alterations and affects will be one of the future points of research to aid in designing a model for the determination of an optimal frequency.

*Acknowledgement:* The contents in this chapter is adapted from the author's published work in reference 1. The author is the first author on this manuscript and have contributed to the work in every aspect. The author would also like to thank Dr. Jeffrey LaBelle for guidance and Lindsey Ryder for assisting the experiments. The contents in this chapter received permission to reproduce published texts and figures from the coauthors and the publisher. The content of this chapter is protected by the author's provisional patent application #: 62/473,894.

## CHAPTER 2.2

### A DUAL-MARKER PROTOTYPE: TWO ENZYMES

#### INTRODUCTION

After demonstrating EIS's multimarker potential with a dual-marker prototype using 2 antibodies, this chapter investigates a dual-marker prototype using 2 enzymes. As discussed previously, since enzymatic reactions are very different from affinity binding reactions, investigating a dual-marker prototype using enzymatic biomarkers is very important. To develop this prototype, glucose and lactate were selected as the 2 example biomarkers, see Chapter 1.1 for more details. Glucose is the most important biomarker for glycemic control and many glucose meters are currently commercially available. Lactate on the other hand, is also a vital biomarker for glycemic control from a therapeutic perspective. DM patients are often encouraged to exercise, but without knowing the lactate levels in the body, achieving sufficient exercise intensity for therapeutic purposes can be challenging. As discussed in greater detail in Chapter 1.2, the commercially available glucose meters and lactate meters often utilize the amperometric technique. In the amperometric technique, with the presence of an electron acceptor, a bias voltage is supplied to help facilitate the electrons generated from the oxidation of reactants. Since the reaction generates current, detection of target analytes is more robust comparing to the label-free affinity binding reactions. In a hindsight, using EIS to detect glucose and lactate does not necessarily hold competitive advantages besides academic novelty. Both biomarkers are comparably more concentrated in human body than many proteomic biomarkers, and amperometric techniques provide sufficient sensitivity and accuracy to achieve clinical utility. However, it is suspected that the optimal frequencies of enzymatic biomarkers may have different characteristics compared to affinity-binding biomarkers. For this reason, in addition to their high concentrations, glucose and lactate are ideal enzymatic biomarkers for the investigation of optimal frequencies and dual-marker biosensors. The author has successfully developed novel tear glucose and tear lactate biosensors using amperometric techniques, which can be added toward the multi-marker platform as a backup.

Although an enzymatic reaction generates electrical signal, detecting two enzymatic biomarkers using EIS is not necessarily an easy task, as distinguishing the electrons generated by one biomarker from the other can be challenging in a label-free setting. Fortunately, the concept of optimal frequency applies to enzymatic biomarkers as well. Using the complex impedance, the optimal frequency of glucose was previously demonstrated by Adamson *et al*<sup>144</sup>. While the optimal frequency of lactate has never been published, Gamero *et al* have developed an EIS based lactate sensor using the charge transfer resistance obtained from equivalent circuit modeling<sup>155</sup>. In this chapter, after identifying the optimal frequencies of glucose and lactate, the two biomarkers were co-immobilized onto the same working electrode to investigate the feasibility of a dual-enzymatic-marker biosensor.

## METHODS

A standard sensor preparation protocol utilizing the gold-disc electrodes (GDE) and the self-assembled monolayer was used to prepare the sensors (see Appendix B). For the immobilization of molecular recognition elements, the concentrations of lactate dehydrogenase and glucose oxidase were 9.4 mg/mL and 10 mg/mL, respectively. Final lactate and glucose samples were made in PBS and tested according to their respective physiological levels. The lactate concentrations tested were 0, 2.2 mM, 4.4 mM, 8.8 mM, 15 mM, and 30 mM. Each lactate concentration was accompanied with 30 mM of NAD cofactor as the electron acceptor. The glucose concentrations tested were 0, 8 mg/dL, 25 mg/dL, 60 mg/dL and 100 mg/dL (which is equivalent to 0, 0.006, 0.55, 1.5, 3.3, and 5.5 mM). For co-immobilization, the same concentrations of glucose oxidase and lactate dehydrogenase were immobilized on the GDEs. When testing the dual-marker sensors, the lactate concentrations were held at 1, 8, and 30 mM while the glucose concentration varied from 0 – 100 mg/dL at the same intervals described above. All samples were tested in 100 mM potassium ferricyanide as detailed in Appendix D. The imaginary impedance algorithm described previously was used to obtain the optimal frequencies

of lactate and glucose. The sensors underwent the same quality control steps described in Appendix C (data not shown). For modeling the dual-marker prototype's response, an Excel addon called XL-STAT was used to model the individual biomarker's response and deconvolute the co-immobilized signal as described previously. Lower limits of detection (LLD) were calculated using the  $3.3 * \text{standard deviation} / \text{slope}$ .

Physical adsorption of 10 mg/mL of glucose oxidase on screen printed carbon electrodes was performed as described in Appendix A. Briefly, 10  $\mu\text{L}$  of 10mg/mL of glucose oxidase was pipetted onto the sensing well of Zensor. The sensors were dried at 25°C in the incubator and then subjected to chemical vapor generated by 1 mL 25% glutaraldehyde. The glutaraldehyde crosslinks the primary amines of adsorbed proteins, holding them together on the surface of the electrode. Blocking of unreacted aldehyde groups was performed with 10 mM TRIS-HCL. The sensors were then stored in PBS and used immediately.

## RESULTS AND DISCUSSIONS

Using the methods described above and the imaginary impedance algorithm, the optimal frequencies of lactate and glucose were found to be 97.66 Hz and 31.5 Hz, respectively (Figure 11). The optimal frequency of glucose was found to be smaller than lactate. Perhaps one possible reason is the molecular weight (glucose is 180.156 g/mol and lactate 89.07 g/mol). It is interesting to note that, in the enzymatic biomarkers, a larger molecular weight yielded higher optimal frequency, whereas in the affinity-binding biomarkers investigated in previous chapter (LDL&HDL), a biomarker with larger molecular weight yielded lower optimal frequency. The effect of molecular weight on the optimal frequency is discussed further in Chapter 3.2.



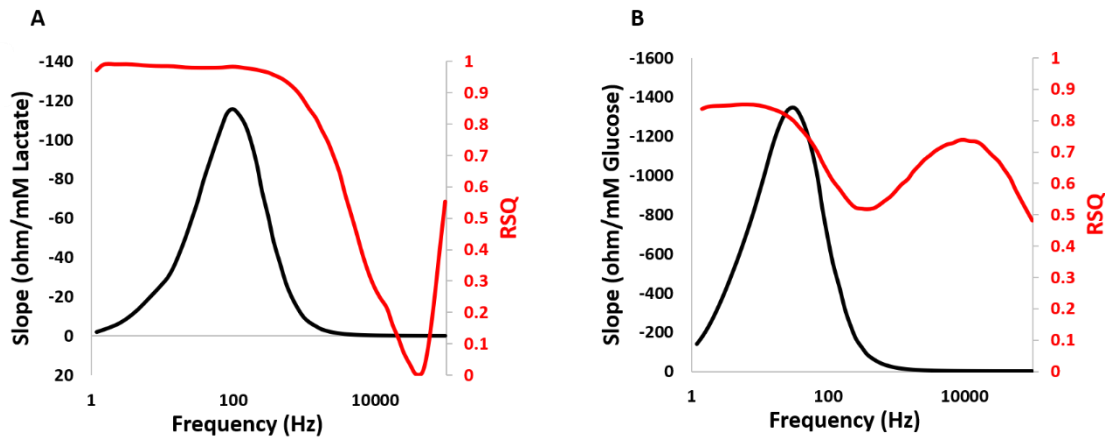


Figure 11: Electrochemical responses of lactate and glucose. Overlay of slope and RSQ values for A) lactate and B) glucose. Based on the imaginary impedance algorithm, the optimal frequency for lactate was found to be 97.66 Hz and glucose 31.5 Hz

Figure 12 shows the calibration curves of lactate and glucose at their respective optimal frequencies (97.66 Hz and 31.5 Hz, respectively). The concentrations tested for lactate were 0, 2.2 mM, 4.4 mM, 8.8 mM, 15 mM, and 30 mM and glucose 0, 0.06, 0.55, 1.5, 3.3, 5.5 mM (0, 1, 8, 25, 60, 100 mg/dL), respectively, both meeting the normal physiological levels<sup>156,157</sup>. Note that although glucose levels can be as high as 27.7 mM (500 mg/dL) in extreme hyperglycemia cases, a heavier emphasis is placed in hypoglycemia due to its clinical significance, as hospital admission rates for hypoglycemia exceeded those for hyperglycemia<sup>158</sup>. Therefore, the glucose concentration tested was between the 0 – 100 mg/dL. The LLDs of lactate and glucose were calculated to be 3.38 mM and 0.29 mM (6.23 mg/dL), respectively. While both are within the physiological values, the LLDs are similar to the amperometric approaches in author's other works<sup>10,12</sup>.

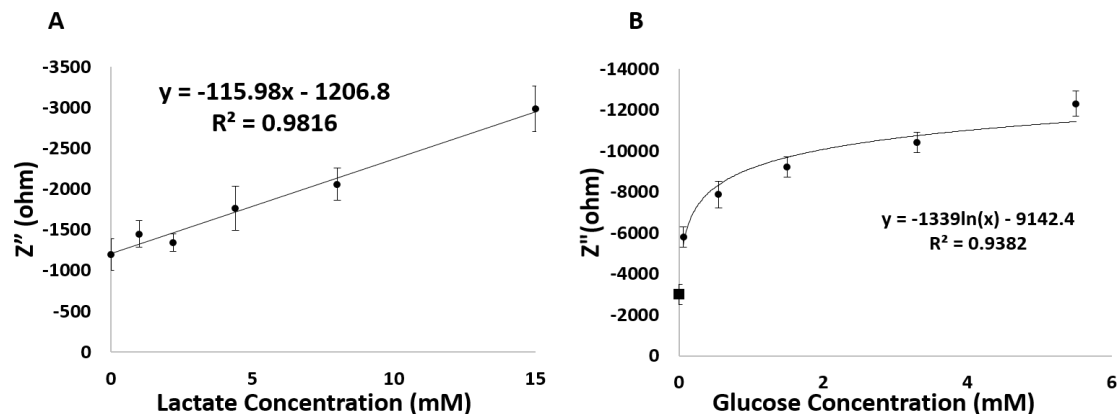


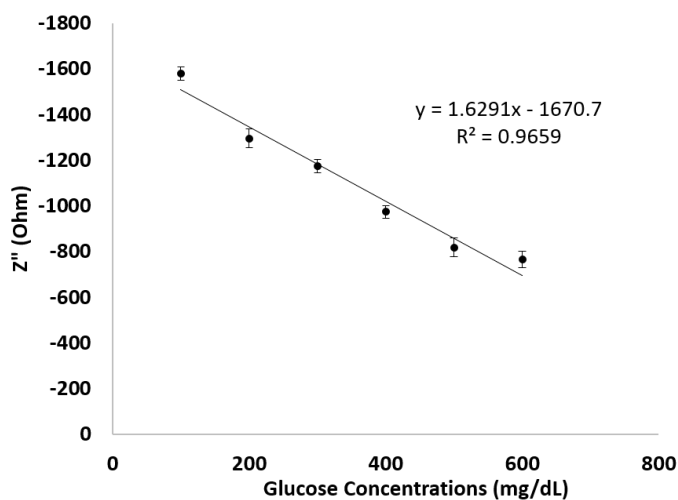
Figure 12: Calibration curves of A) lactate at 97.66 Hz and B) glucose at 31.5 Hz. Both lactate and glucose had N = 4 repetitions at each concentration. Error bars were calculated as 1 standard deviations.

As seen in Figure 12, the slope response for glucose was much higher than lactate. The larger response is not believed to be due to concentration difference, as the blank response of glucose is already higher than the response of 15 mM of lactate. One possible explanation is the difference in molecular weight. The molecular weights of lactate dehydrogenase and glucose oxidase are 115 kDa and 160 kDa, respectively. Glucose is also larger than lactate (180.156 g/mol and 89.07 g/mol, respectively). Therefore, the larger impedance from glucose sensors can be attributed to a larger obstruction of electrons from the immobilized glucose oxidase and the diffusion of glucose.

Considering the Ohm's Law and how the enzymatic reaction generates electrons, an increase in the current should result in a decrease in resistance. But in Figure 12, an opposite trend was observed: an increase in glucose or lactate concentration leads to an increase in impedance. This can be explained by EIS being a near-field technique and the presence of self-assembled monolayer. When glucose or lactate was oxidized, electrons were generated and were facilitated by the redox mediator, potassium ferricyanide. When a ferricyanide ( $[\text{Fe}(\text{CN})_6]^{3-}$ ) received an electron, it reduced to ferrocyanide ( $[\text{Fe}(\text{CN})_6]^{4-}$ ). The presence of SAM prevented the ferrocyanide from diffusing to the surface of electrode rapidly to pass off the electrons, causing a

local accumulation of ferrocyanide on the surface of SAM where the enzyme is immobilized. Since the reduced ferrocyanide is unable to take on more electrons, it became a barrier to impede the flow of electron, causing an increase in the impedance. Therefore, the impedance increased with an increase in glucose or lactate concentrations. The trend can be reverted when SAM is not present. Using the physical adsorption protocol described in Appendix A to immobilize the same amount of glucose oxidase on the screen-printed carbon electrodes, an increase in glucose concentration caused a decrease in impedance (Figure 13), suggesting the local accumulation of reduced ferrocyanide on SAM is indeed a reason for this phenomenon. Since glucose and lactate are not conductive, analyte accumulation near the surface of SAM can be impeding the electrons as well<sup>159</sup>.

Figure 13: Calibration curve of glucose sensors prepared by physical adsorption at 31.5 Hz. Error



bars were calculated as 1 standard deviation.

The EIS response of biosensors prepared by coimmobilizing glucose oxidase and lactate dehydrogenase can be found in Figure 14. Recall that the optimal frequency of lactate was found at 97.66 Hz and glucose 31.5 Hz. As seen in Figure 14, the imaginary impedance peaks at near 100 Hz for all scenarios, which is similar to the lactate's optimal frequency. However, as seen in Figure 14 A-C, low RSQ values at glucose's optimal frequency (31.5 Hz) indicated poor

correlation of impedance to glucose concentrations. One possible reason is the ubiquitous accumulation of ferrocyanide on SAM, which impedes the flow of electron onto sensor surface. As ferricyanide receives the electrons generated from enzymatic reactions from both biomarkers, they are reduced to ferrocyanide, which severely contaminates the signal in each biomarker's optimal frequency. From Figure 14D, high RSQ values at lactate's optimal frequency (97.66 Hz) suggested that lactate can still be detected in the presence of glucose. However, as described above, due to the accumulation of ferrocyanide on SAM, the correlation may not be lactate specific.

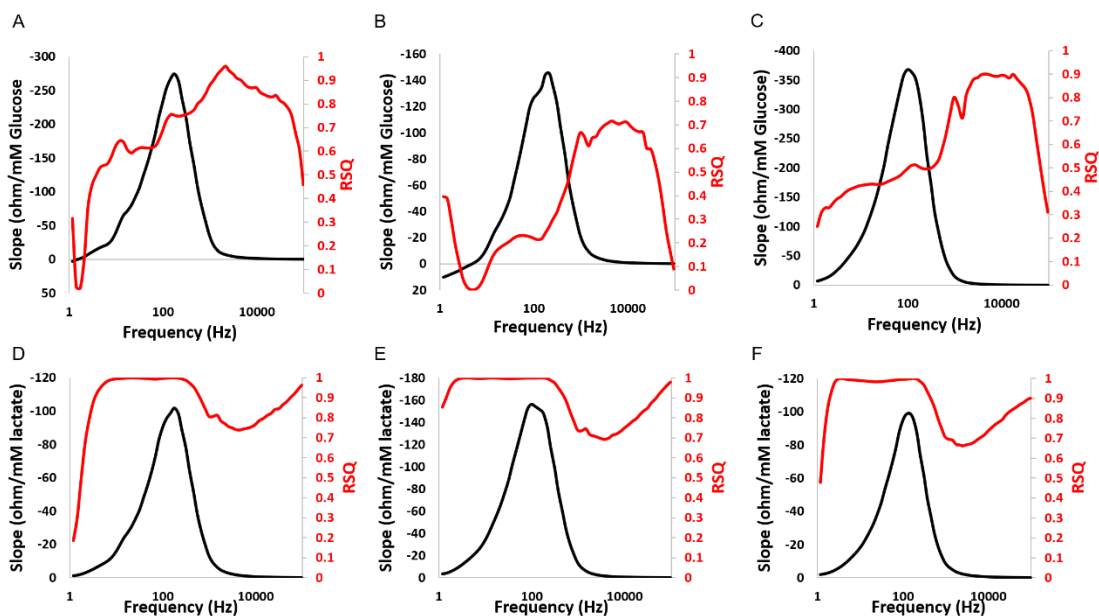


Figure 14: Coimmobilization of Lactate and Glucose. A) Glucose gradient in the presence of 1 mM lactate. B) Glucose gradient in the presence of 8 mM lactate. C) Glucose gradient in the presence of 30 mM lactate. D) Lactate gradient in the presence of 0.06 mM, E) 3.3 mM, and F) 5.5 mM glucose.

An experiment demonstrating how the change in concentrations of ferricyanide and ferrocyanide affects EIS impedance was performed by Yuka Ito and Dr. Koji Sode at the Tokyo University of Agriculture Technology (Appendix G, with permission). As ferricyanide is reduced to ferrocyanide, an trace amount of ferrocyanide (i.e. 1 mM) and an decrease in ferricyanide concentration can

cause a large increase in impedance. A potential solution is to avoid the use of SAM in identifying the optimal frequency of enzymatic biomarker. For example, the physical adsorption of MREs described in Appendix A can be adapted, see Chapter 3.1 for more details.

In an attempt to deconvolute the signal, the signal deconvolution algorithm described previously was implemented (Figure 15). However, the signal deconvolution failed to return two distinct peaks like the previous work<sup>1</sup> and no correlation could be drawn to either biomarker. One potential reason can be the accumulation of ferrocyanide on SAM as well, which contaminates the signals by blocking the flow of electrons on a system level.

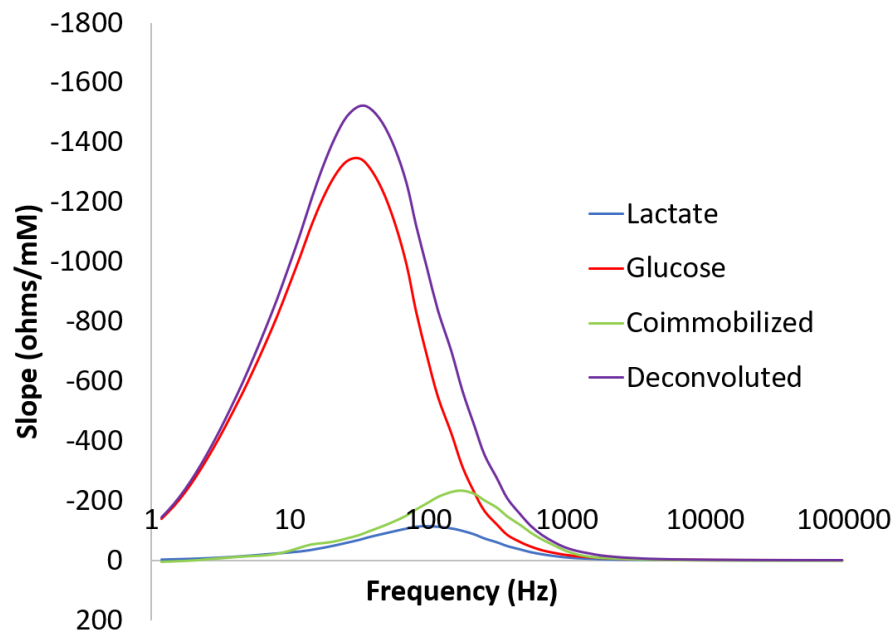


Figure 15: EIS deconvoluted response of coimmobilized glucose and lactate.

## CONCLUSION

Although EIS can detect individual enzymatic biomarker accurately, the increase in impedance is not due to the formation of biological complexes such as antibody-antigen, but the change in the ratio of ferricyanide and ferrocyanide. Therefore, detecting a glucose-lactate dual-marker sensor

using SAM was unsuccessful. To accurately detect the enzymatic biomarker's optimal frequency, an immobilization technique not involving the use of SAM (which is electronically insulating) may be more suitable for enzymatic biomarkers. As an alternative, amperometric sensors for glucose and lactate in author's previous work<sup>2,6-8,10,12</sup> can be integrated together to achieve the duo-marker detection.

*Acknowledgement:* The authors would like to thank David Probst and Yuka Ito for assisting with the experiments. The author would also like to thank Dr. Sode for the intellectual support regarding the local accumulation of ferrocyanide on SAM.

## CHAPTER 2.3

### A DUAL-MARKER PROTOTYPE: ONE ANTIBODY AND ONE ENZYME

#### INTRODUCTION

Continuing the effort of developing EIS multimarker sensors with dual-marker prototypes, this chapter investigates a dual-marker prototype with the combination of an antibody and an enzyme. To develop this prototype, insulin and glucose were selected as the 2 example biomarkers. As discussed in Chapter 1.1, insulin and glucose are 2 vital biomarkers for glycemic control. Insulin is particularly challenging to develop due to its small molecular size, low physiological concentrations, and self-aggregating property. In addition, recently, a study revealed a drastic difference between the actual and advertised insulin activities in commercial insulin vials<sup>67</sup>. Therefore, besides its clinical benefits, an insulin sensor can also serve as a rapid tool for quality control. For these reasons, since an EIS glucose sensor was already developed in previous chapter, this chapter focuses on the development of an insulin POC sensor. As discovered from the previous chapter, optimal frequency in enzymatic biosensors has unresolved challenges in multimarker detection. The coimmobilization of insulin antibody and glucose oxidase was thus not performed in this work. Instead, a model projecting the electrochemical response of insulin-glucose dual-marker sensor is investigated.

#### METHODS

A standard sensor preparation protocol utilizing the GDE and the self-assembled monolayer was used to prepare the insulin sensor (Appendix B). For the immobilization of molecular recognition elements, the concentration of insulin monoclonal antibody and glucose oxidase was 23.4 mg/mL and 10 mg/mL, respectively. For more details, please refer to the Appendix B. Final insulin and glucose samples were made in PBS and tested according to their respective physiological levels from 0  $\mu$ M to 1500  $\mu$ M and 0 – 5.5 mM (0 - 100 mg/dL), respectively. The imaginary impedance algorithm described previously was used to obtain the optimal frequencies of insulin and glucose. For modeling the dual-marker prototype's response, an Excel addon called XL-STAT was used to

model the individual biomarker's response and summed the two together to predict the co-immobilized response. All circuit modeling was performed with ZSimpWin software.

## RESULTS

Using the methods described above, the optimal frequencies of insulin and glucose were found to be 810.5 Hz and 31.5 Hz, respectively (Figure 16). It is also expected that glucose generates a much larger signal than insulin, as its concentration was much higher than insulin.

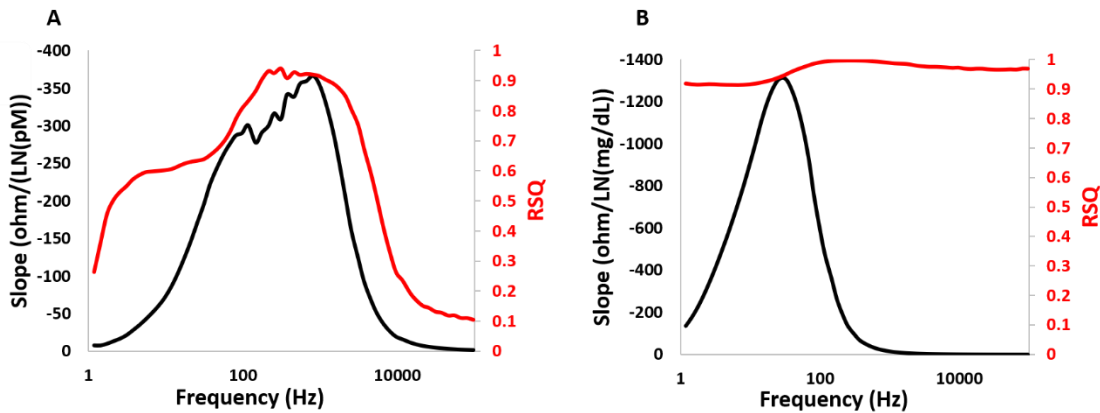


Figure 16: Electrochemical Responses of A) insulin and B) glucose. Based on the imaginary impedance algorithm, the optimal frequency for insulin was found to be 810.5 Hz and glucose 31.5 Hz

Figure 17 shows the calibration curves of insulin and glucose at their respective optimal frequencies (810.5 Hz and 31.5 Hz, respectively). The concentrations tested for insulin were 0, 50, 100, 200, 250, 500, 750, 1000, 1500  $\rho M$  and glucose 0, 0.06, 0.55, 1.5, 3.3, 5.5 mM (1, 8, 25, 60, 100 mg/dL), respectively, both meeting the normal physiological levels <sup>157,160</sup>. Using the standard 3.3 \* standard deviation / slope, the lower limits of detection (LLD) of insulin and glucose were calculated to be 2.64  $\rho M$  and 0.29 mM (6.23 mg/dL), respectively.



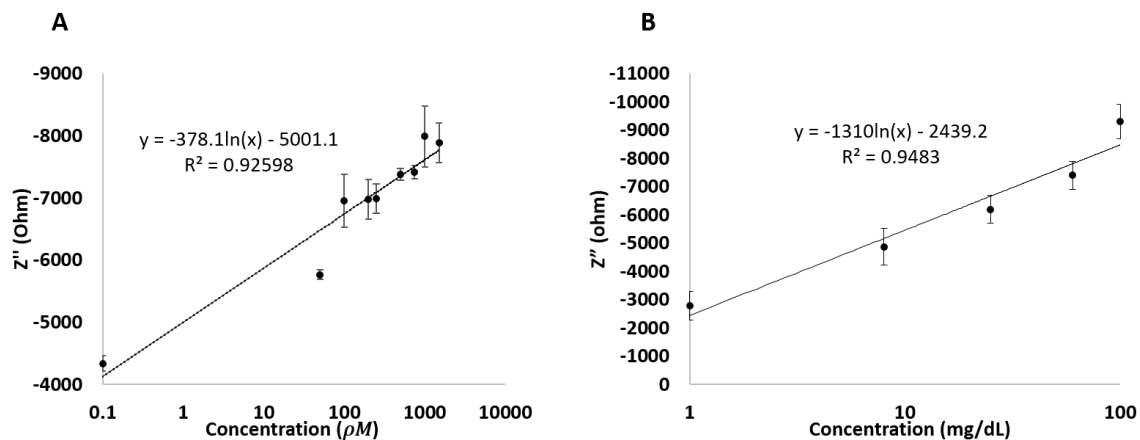


Figure 17: Calibration curves of A) insulin at 810.5 Hz and B) glucose at 31.5 Hz. Each insulin concentration was replicated 7 times and glucose 4 times at each concentration. Error bars were calculated as 1 standard deviations.

Using ZsimpWin, the ideal circuit model that best describes the electrochemical system of insulin sensor can be obtained (Figure 18). The solution resistance and the electron transfer resistance were both modeled as resistors and were labeled as  $R_{sol}$  and  $R_{et}$ , respectively. The pseudo-capacitor is modeled as  $Q$  and represents the piece of the system that can be correlated to the molecular recognition element being used<sup>1</sup>.

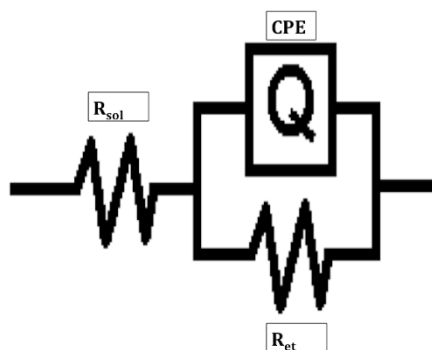


Figure 18: Electrochemical circuit modeling of the insulin sensor.  $R_{sol}$  is the resistance due to solution,  $R_{et}$  is the electron transfer resistance.  $Q$  is used to represent the constant phase element (CPE) or the imperfect capacitor of the system. Reprinted with permission from reference 5. © Diabetes Technology Society

Figure 19 shows the correlation between charge transfer resistance and target insulin concentrations derived from equivalent circuit modeling, a standard method of analyzing EIS data<sup>161</sup>. Using this approach, the LLD was found to be 14.46  $\rho M$ .

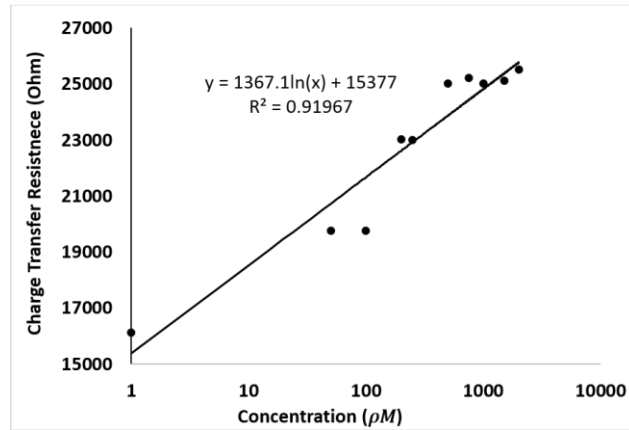


Figure 19: Insulin calibration curve relating the calculated charge transfer resistance against the change in concentration of insulin in  $\rho M$ . Reprinted with permission from reference 5. © Diabetes Technology Society

Using XL-STAT, the predicted glucose and insulin co-immobilized signal is shown in Figure 20. Two distinct peaks at 31.5 Hz and 810.5 Hz were observed, each representing the optimal frequency of glucose and insulin, respectively.

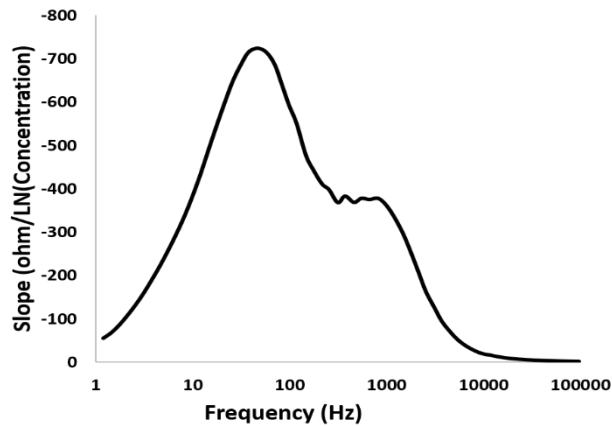


Figure 20: Modeled co-immobilization signal of insulin and glucose. The two distinct peaks at 31.5 Hz and 810.5 Hz represent the optimal frequency of glucose and insulin, respectively.

## DISCUSSION

The use of imaginary impedance successfully allowed the detection of insulin at its physiological level. Once the calibration curve was identified, a hand-held device could be programmed and upon running EIS on an unknown sample, the calibration curve would convert an imaginary impedance reading into an insulin concentration. The LLD was found to be  $2.64 \mu\text{M}$  and dynamic range from  $50 \text{ pM}$  to  $1500 \text{ pM}$ , which met clinical needs. From a clinical standard detection of insulin, ELISA can accurately detect labeled insulin at  $1.39 \mu\text{M}$ <sup>162</sup>, which is slightly higher than the insulin sensor prototype. However, with some more optimizations on parameters such as antibody concentration and sensor reproducibility, the LLD may be improved. Even more so, techniques such as ELISA or high-performance liquid chromatography have labeling steps and many associated techniques that can be performed only in laboratories. EIS on the other hand, is a label free technique, and the sensor prototype can be translated into screen printed sensors, allowing the possibility of POC with portable device and disposable test strips similar to the setup of self-monitoring of blood glucose<sup>126,163</sup>.

We have shown that the EIS method of using imaginary impedance can very well detect insulin in the physiological range. Future studies will look into replicating the trials with much smaller concentration interval sizes such as  $1 \text{ pM}$ , which is equivalent to a gold standard ELISA to distinguish between even the smallest changes in concentration. Interference and clinical samples will also be tested to evaluate robustness and optimize further toward a POC device. This will lay a solid foundation for the multi-marker platform sensor to truly enhance a person's glycemic control. Lastly, unlike other publications on insulin detection there was no modification to the insulin solution via pH<sup>122,143</sup>.

The FDA requires all glucose meters to be within 20% variance from standards<sup>164</sup>. Currently, the replicated results show that across all sample concentrations the %RSDs ranges from 5% to 26%, suggesting there are still room for improvements. Although batch analysis has helped

eliminate some of the variance between GDEs, polishing and reusing GDEs is a significant source of variance as surface roughness of gold can affect SAM formation<sup>165</sup>, affecting the capacitance of imperfect parallel plate capacitor explained in later section. Transition to screen printed sensors will reduce the variance of surface roughness under consistent manufacturing procedures and rigorous QC.

### *Circuit Analysis*

Generally, EIS is analyzed with equivalent circuit modeling. Typically, the best-fit circuit for a semi-circle looking Nyquist plot is the Randles circuit, which models the electrochemical interactions as a resistance-capacitor circuit in parallel. The electron transfer resistance can be used to derive a calibration curve linking back to input concentration<sup>162,166</sup>. However, recently some researchers have demonstrated the use of a modified Randles circuit that implements a constant phase element (CPE) to model the capacitance<sup>1,160,167</sup>. CPE is commonly referred to as either a leaky or imperfect parallel plate capacitor (IPPC). The bottom plate is the surface of electrode and the top plate is the top of the SAM with MREs immobilized owing to SAM's insulating property<sup>168</sup>. The MREs different shape, orientation and size alter the smoothness of SAM in various ways, constituting the IPPC. As binding occurs, the target-MRE complex further alters the capacitance of the IPPC, affecting the electron transferring properties and impedance signals, which is evident in Figure 6. This model gives a better description of the actual system when compared to the ideal Randles. Since imaginary impedance correlates to capacitance<sup>161</sup>, we used imaginary impedance to correlate target concentration to reflect the impedance signal generated from changes in CPE, which we believe to have less noise than using the complex impedance approach and omits the trouble of circuit modeling. Owing to this nature, it's no surprise that the LLD in imaginary impedance (2.64  $\rho M$ ) is lower than that of the charge transfer resistance approach (14.46  $\rho M$ ).

### *Dual-Marker Detection*

In terms of dual-marker detection, this insulin and glucose combination benefits from the large separation between the two biomarkers' optimal frequencies. Two biomarkers with distinct optimal frequencies are much easier to detect simultaneously. Based on the modeled co-immobilization response, a signal deconvolution may be unnecessary to detect insulin and glucose simultaneously. Although it is probable to measure insulin and glucose simultaneously by monitoring the signal from each biomarker's optimal frequency, actual co-immobilization is required to validate this claim. The accumulation of ferrocyanide on SAM from glucose's enzymatic reaction discussed in previous chapter is another challenge to overcome first. As a backup, the author's published work on the amperometric glucose sensor<sup>2,6,8,10</sup> can be employed in conjunction with an EIS insulin sensor to achieve dual-marker detection. The proposed endeavor will be continued in a \$1.5 million grant awarded by the Leona M. and Harry B. Helmsley Charitable Trust, which was mostly written by the author. The work in this chapter can be translated to a screen-printed sensor platform to develop the disposable insulin test strip suitable for rapid insulin testing.

### CONCLUSION

We have shown that the EIS method of using imaginary impedance can very well detect insulin in the physiological range. Future studies will look into replicating the trials with much smaller concentration interval sizes such as 1  $\mu\text{M}$ , which is equivalent to a gold standard ELISA to distinguish between even the smallest changes in concentration. Interference and clinical samples will also be tested to evaluate robustness and optimize further toward a POC device. The drastic difference in optimal frequencies between insulin and glucose suggests the likelihood of developing the EIS dual-marker sensor. Although it is pitiful that such co-immobilization was not accomplished in this work, the successful development of a rapid, label-free insulin sensor alone has a great impact in future glycemic management. The proposed insulin glucose dual-marker sensor will be continued in the author's \$1.5 million grant award from the Leona M. and

Harry B. Helmsley Charitable Trust. Should the EIS approach of developing an insulin and glucose dual-marker sensor become unsuccessful, an EIS insulin sensor with an amperometric glucose sensor still holds great novelty and practicality.

*Acknowledgement:* The contents in this chapter is adapted from the author's published work in reference 5 with permissions from the coauthors and the publisher. Although the author is the 3rd author on this manuscript, he was responsible for designing the experiments, mentoring the students, setting the protocols, analyzing the results, and writing the manuscripts. The author would also like to thank Dr. Jeffrey LaBelle and Dr. Curtiss Cook for guidance, and David Probst and Aldin Malkoc for assisting the experiments.

## CHAPTER 3

### FACTORS AFFECTING THE OPTIMAL FREQUENCY

#### CHAPTER 3.1

##### DIRECT MEASUREMENT OF A BIOMARKER'S NATIVE OPTIMAL FREQUENCY

###### INTRODUCTION

From Chapter 2.1, it appears that the optimal frequency (OF) allows simultaneous detection of two affinity-binding biomarkers (i.e. LDL and HDL), and has the potential to detect single affinity-binding biomarkers that are at  $\mu\text{M}$  concentrations (Chapter 2.3). Like many others, the OF has been advocated as an additional means of specificity to supplement the antibody-antigen reaction, while also reducing the assay time and hardware requirements for the measuring system<sup>142,144,146,163,169–172</sup>. However, many previous studies, including the author's own work, have studied the OFs of various proteomic biomarkers using self-assembled monolayers (SAMs) to supply the needed functional groups for immobilization<sup>142,144,146,163,169–172</sup>. The SAMs are long, electrically insulating spacers that are meant to increase sensor's sensitivity by altering the baseline capacitance and resistance of the electrochemical cell. Consequently, whether each biomarker still possess its native OF without the use SAM remains to be investigated. To study a biomarker's native OF, it is necessary to construct an experimental platform without potential interference from complex immobilization reactions.

To construct the experimental platform with the intention of developing a practical immunosensor for point-of-care (POC) applications, a simple yet reliable method of sensor fabrication is needed. Site-directed (oriented) immobilization is typically preferred over randomized immobilization due to its increased sensitivity and consistency<sup>173</sup>. However, oriented immobilization often requires complicated labeling procedures from antibody pretreatment to immobilization. Physical adsorption is generally the simplest immobilization technique, but it is often accompanied by a reduction in sensitivity<sup>174</sup>. Fortunately, the EIS measurement technique has demonstrated femto-

molar level sensitivity<sup>175</sup>. The combination of physical adsorption and EIS not only permits the study of a biomarker's native optimal frequency, but may also overcome the sensitivity disadvantages of physical adsorption-mediated immobilization.

To achieve these goals, two biomarkers are selected for investigation: lactoferrin (Lfn) and immunoglobulin E<sup>52</sup> (IgE). As discussed in Chapter 1.1, the IgE and Lfn analytes are two vastly different proteins. However, the commonalities amongst their MREs (both 150 kDa monoclonal IgG) permit a similar baseline for investigation. While suitable for investigating the native OF of a biomarker, Lfn and IgE also have strong clinical applications in ocular diseases such as disease DED and AC due to their common misdiagnosis (see Chapter 1.1 for more details). A POC biosensor facilitating the differential diagnosis of DED and AC remains in high demand<sup>31</sup>. To achieve this goal, under the generous funding from the Advanced Tear Diagnostics, LLC, the author not only developed an investigational platform for monitoring the native OF of two proteomic biomarkers, Lfn and IgE, but also integrated the tear sampler developed in previous works<sup>6,10,12</sup> to achieve a prototype for POC diagnostics.

This work aims to provide novel knowledge by investigating: i. the existence of a biomarker's native OF via direct measurement of biomolecules ii. the potential to overcome the limitations in physical adsorption-based immobilization with EIS. Physical adsorption is achieved through glutaraldehyde (GA) mediated crosslinking of MREs on screen printed carbon electrodes (SPCEs). The resulting stability and performance of the sensor in complex media are also evaluated. After building the testing platform, an integrated, disposable tear Lfn and IgE POC test strip prototype was accomplished



## METHODS

### *Chemicals and Biologicals*

All chemical reagents were purchased from Sigma-Aldrich, MO, unless otherwise stated. The antibodies utilized in the detection of IgE and Lfn were: mouse monoclonal IgG (Scripps Laboratories, CA) and human monoclonal IgG (Fitzgerald, MA), respectively. The IgE antigen supply was obtained from purified myeloma cells courtesy of Scripps Laboratories, CA (lot #2131302) and recombinant human Lfn was obtained from Agennix, TX (lot #803001/803001A). All solutions were prepared in phosphate buffer saline (PBS, pH 7.4) unless stated otherwise.

### *Preparation of Lactoferrin and IgE Sensor Platforms*

#### *Screen Printed Carbon Electrodes Setup (SPCE-alpha)*

The SPCE-alpha was designed for investigating the native OF of a biomarker. This platform was built on a commercially available disposable SPCE, Zensor (CH Instruments, TX), containing graphite working and counter electrodes and a silver/silver chloride reference electrode. The detailed protocol can be found in Appendix B but is included here for clarity. A schematic of the sensor preparation protocol is illustrated in Figure 21. First, 1  $\mu\text{g}$  of the respective antibody in PBS was deposited onto the working electrode and dried in a Thermocenter at 24 °C for 25 minutes. Once dry, the sensors were exposed to GA vapor generated from 1 mL of 25% GA in a parafilm-sealed vessel on an orbital shaker for 1 hour at 80 rpm<sup>176</sup>. This process permits covalent crosslinking of the deposited antibodies. The sensors were again dried at 24 °C for 25 minutes, allowing the cross-linked antibodies to adsorb onto the graphite working electrode. Blocking of unreacted aldehyde groups from GA-crosslinking was achieved by submerging the sensing well in 1 mM Trizma<sup>®</sup> and hydrochloric acid (TRIS-HCl) solution (pH 7.4) for 25 minutes<sup>177</sup>. Sensors were rinsed in PBS followed by DI and again dried at 24 °C. The sensors were either i. immediately subject to electrochemical testing or, ii. stored at 4 °C for future stability evaluation.

#### *Screen Printed Carbon Electrode with Integrated Tear Sampling Component (SPCE-beta)*

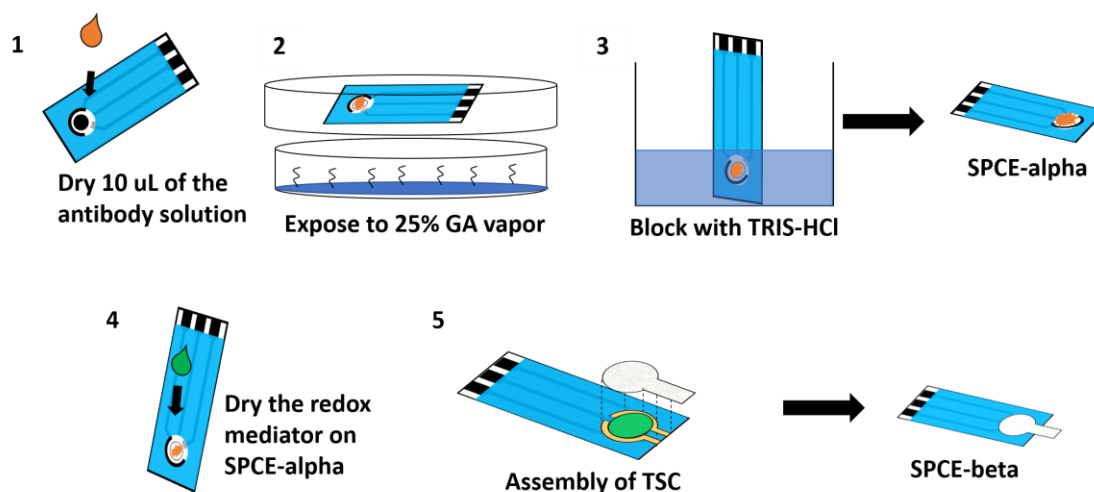


Figure 21. Sensor fabrication schematics using SPCE and TSC. Step 1 – 3 denotes the fabrication process of SPCE-alpha prototype while 4-5 show the additional manufacturing steps required to assemble the SPCE-beta prototype. Reprinted with permission from reference 9. © American Chemical Society.

To expand on the application potential of SPCE-alpha, a tear sampling component (TSC)-integrated form, SPCE-beta, was adopted. Whatman 41 ashless filter paper (Lot# 9585790) used in Schirmer's test strips<sup>178</sup> and an adhesive layer (3M 467MP/200MP, Grainger, AZ) were utilized to construct the TSC. Detailed laser cutting protocols can be found in Appendix E. The filter paper and the adhesive layer were cut into their respective shapes using a Universal Laser PLS 4.75 laser cutter. To construct the SPCE-beta, 30  $\mu\text{L}$  of 10 mM potassium ferricyanide (III) was dried onto the sensing well of the pre-fabricated SPCE-alpha at 24 °C for 45 minutes. To mount the TSC, the adhesive layer was carefully placed around the sensing well to prevent any contact with the counter, reference or working electrodes. The filter paper was then attached to the sensor with the adhesive tape. Completed sensors were stored dry at room temperature prior to testing. A schematic of the fabrication process is shown in Figure 21.

### *Electrochemical Evaluation*

All sensors were connected to an electrochemical CHI 660C analyzer (CH Instrument, TX) using a soldered gold-plated edge connector (Digikey, MN). Cyclic voltammetry (CV) was first

conducted to determine the formal potentials (input voltage for EIS) of SPCE-alpha and SPCE-beta. CV was performed by sweeping from -0.6 V to 0.6 V. EIS was then used as the primary means of evaluation. To conduct EIS, a sinusoidal input voltage with a 5 mV amplitude spanning a range of frequencies from 100 kHz to 1 Hz with a resolution of 12 points per decade was used.

### *SPCE-alpha*

#### *Electrochemical Testing of SPCE-alpha*

To conduct CV, 50  $\mu\text{L}$  of 10 mM potassium ferricyanide (III) was added to the SPCE-alpha sensing well. After obtaining the formal potential, all SPCE-alpha EIS measurements were performed by incubating 5  $\mu\text{L}$  of a known antigen concentration for 60 seconds on the working electrode surface. Next, 45  $\mu\text{L}$  of 10 mM potassium ferricyanide solution was added before initiating the EIS scan. A range of antigen concentrations were tested to cover the desired calibration range for the analyte in question. The clinical cutoffs for Lfn and IgE are 1.1 mg/mL 80 ng/mL, respectively<sup>31,33</sup>. Empirical testing was performed on the following antigen ranges: 0 – 0.2 mg/mL and 0 – 160 ng/mL for Lfn and IgE, respectively. To reduce potential discomfort on dry eye subjects, a 0.5  $\mu\text{L}$  sample volume on the final Lfn sensor was proposed. To accommodate this, the calibration range was intentionally lowered by a factor of 10 to mimic the total mass of Lfn in a 0.5  $\mu\text{L}$  sample. No adjustments were made for IgE as the sample volume for the final IgE sensor is expected to remain 5  $\mu\text{L}$ . All quantitative data is reported as an average signal obtained from 3 - 5 replicates.

#### *Specificity Testing of SPCE-alpha*

Specificity was demonstrated by exposing the anti-Lfn-modified sensors to IgE antigen and vice versa. In these experiments the concentrations of Lfn and IgE were 0.15 mg/mL and 200 ng/mL, respectively, to represent their higher physiological ranges<sup>31,33</sup>.

### *Stability Testing of SPCE-alpha*

After storing the sensors at 4 °C for 7 days, the sensors were electrochemically tested against 0 – 0.2 mg/mL and 0 – 160 ng/mL Lfn and IgE, respectively to evaluate sensor performance.

### *Complex Medium Testing of SPCE-alpha*

To assess the sensor's performance in a complex medium resembling human tears, a simulated tear recipe containing salts and large proteins was adopted<sup>179</sup>. The simulated tear fluid is made by mixing 2.68 mg/mL lysozyme, 6.5 mg/dL D-glucose, 1.34 gamma globulin, 6.5 mg/mL sodium chloride, 2.68 mg/mL bovine serum albumin, 0.08 mg/mL calcium chloride dihydrate in deionized water (pH 7.4). The solution was used to prepare the antigen concentration gradients immediately prior to testing. The sensors were tested against 0 – 0.2 mg/mL and 0 – 160 ng/mL Lfn and IgE, respectively.

### *SPCE-beta*

#### *Electrochemical Testing of SPCE-beta*

On average, the SPCE-beta collects 15  $\mu$ L of fluid with 6% relative standard deviation (RSD) (data not shown) in 20 seconds. Functional prototypes of TSCs capable of collecting 0.5  $\mu$ L samples were also investigated, but due to the surface area of the sensing well, a 15  $\mu$ L volume was the smallest feasible sample volume to avoid shorting. To collect the sample, the TSC of the SPCE-beta was submerged into an excess of antigen solution for 60 seconds to ensure adequate rewetting of the dried reagents and to permit analyte diffusion through the porous filter paper. An additional 60-second incubation was observed to permit analyte binding to the respective MRE absorbed to the working electrode surface. EIS testing began at  $t=120$  seconds. The sensors were tested against 0 – 0.2 mg/mL and 0 – 160 ng/mL Lfn and IgE, respectively.

### *Specificity Testing of SPCE-beta*

The specificity was validated on the SPCE-alpha and no significant differences were expected with the addition of the TSC.

### *Complex Medium Testing of SPCE-beta*

The functionality in complex medium was validated on the SPCE-alpha and no significant differences were expected with the addition of the TSC.

### *Determination of A Biomarker's Native OF*

To determine the native OF of a biomarker, a modified algorithm using the imaginary impedance ( $Z''$ ) response was employed<sup>129,169</sup>. The  $Z''$  values were correlated to target antigen concentrations across the entire frequency spectrum resulting in quantitative descriptors of the calibration line at each discrete frequency, such as slope and R-squared values (RSQ). Unlike other works that advocate the existence of an OF<sup>142,144,146,163,169-172</sup>, the native OF is defined as the single frequency at which the RSQ is highest and sufficient slope is displayed. The significance of an OF is described further in the discussion.

### *Analysis of Sensor Performance*

For reproducibility, the error bars are expressed as one standard error, calculated by  $\sigma/\sqrt{n}$ , where  $\sigma$  is the standard deviation of all replicates performed at that concentration, and  $\sqrt{n}$  is the square root of the total number of replicates. The limit of quantification (LOQ), is expressed as the lowest amount of analyte in a sample that can be quantitatively determined with suitable precision and accuracy (generally +/- 20% RSD)<sup>180</sup>.

## RESULTS AND DISCUSSION

### *Investigation of Optimal Frequencies Using SPCE-alpha*

#### *Electrochemical Response of Purified IgE and Lfn*

Figure 22 below displays the  $Z''$  plotted as a function of frequency over a range of antigen concentrations. Figure 22a and 22b show that the  $Z''$  trend increases with concentration for both biomarkers. Figures 22c and 22d depict the slope and RSQ response parameters across the frequency sweep. The native OFs for Lfn and IgE have been determined to be 57.44 Hz and 371.1 Hz, respectively. The calibration least-squares best fit lines in figures 1e and 1f are reflective of the sensor response at the native OF<sup>129</sup>. From figure 22a – 22d, it is evident that the overall impedance patterns are significantly different between the two biomarkers, confirming that the existence of a native OF is biomolecule-dependent (discussed later). Assuming the existence of a native resonant frequency describing the binding kinetics between a biomarker and its MRE, it is possible to constructively reinforce the reaction by delivering an input of the same frequency. Therefore, the impedance response of a biomarker at its native OF will be most precise (highest RSQ) as compared to other destructive frequencies.

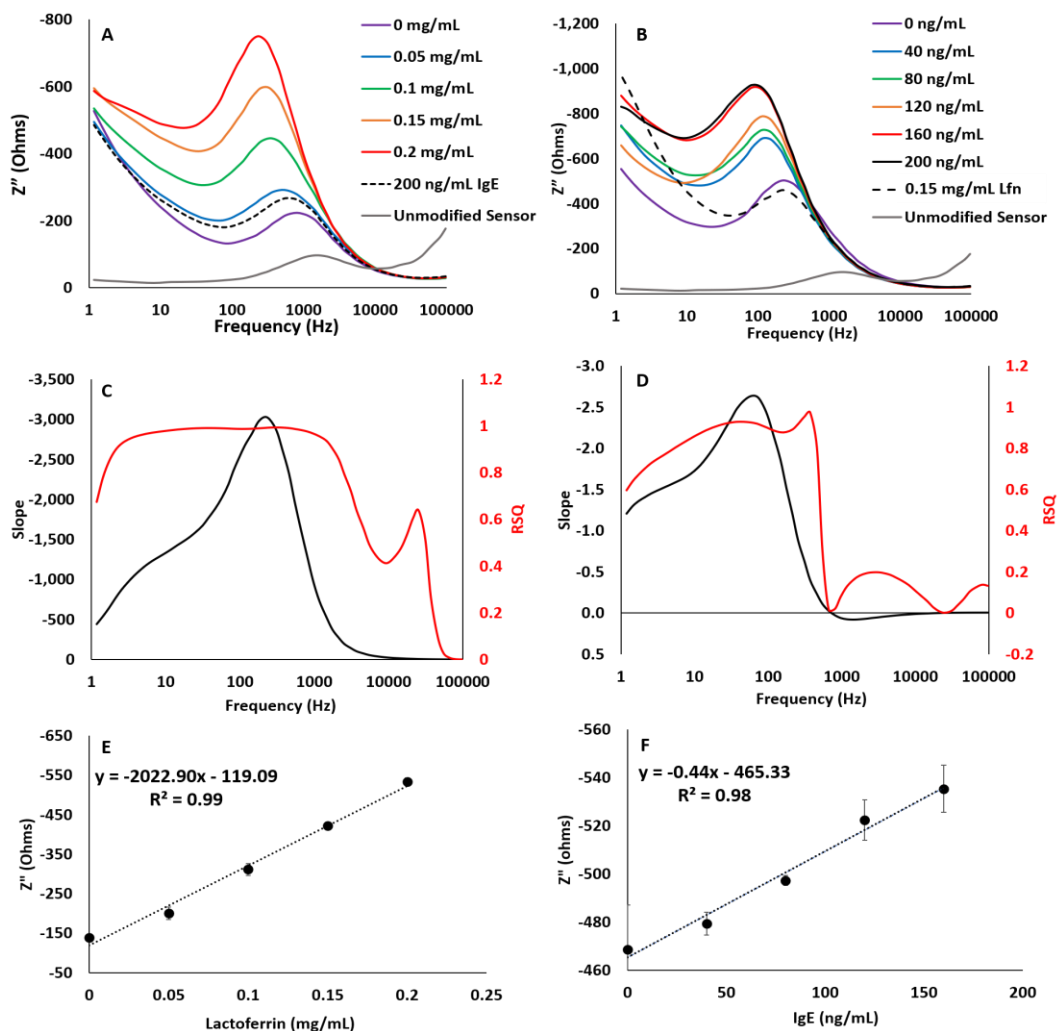


Figure 22: Imaginary impedance ( $Z''$ ) response of Lfn (A) and IgE (B) on the SPCE-alpha platform. Slope and RSQ overlays to determine native OFs of Lfn (C) and IgE (D). Purified calibration curves at each biomarker's optimal frequency Lfn (E) and IgE (F). The linear response across the physiological range of each analyte, can be described by the equations shown in E and F. Each concentration was replicated 5 times. Reprinted with permission from reference 9. © American Chemical Society.

### Specificity

The sensor response when subjected to nontarget proteins across the frequency spectrum is shown by the interrupted lines in Figures 22a and 22b. The specific response at each biomarker's

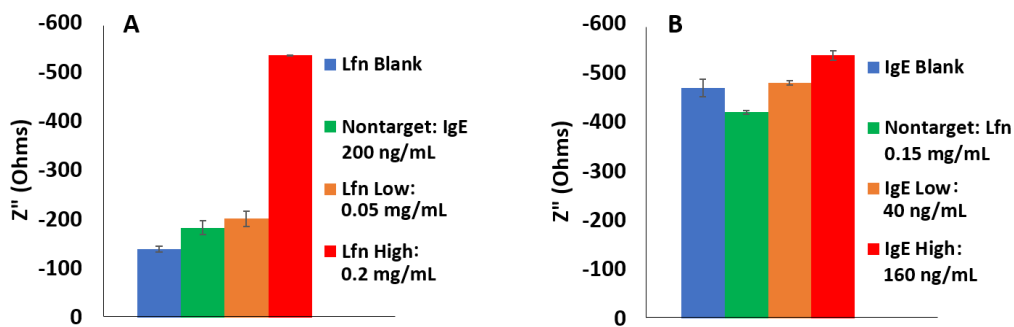


Figure 23: Specificity Testing of Lfn and IgE SPCE-Alpha. Assessment of the dynamic range of sensor responses across the physiological range for Lfn (A) and IgE (B), respectively. The signal magnitude generated by purified solutions containing the nontarget analyte is also shown. Each condition was replicated 5 times. Reprinted with permission from reference 9. © American Chemical Society.

native OF is shown by the nontarget bars of Figures 23a and 23b. The Lfn sensor platform was exposed to high concentrations of IgE (200 ng/mL) and vice versa (0.15 mg/mL Lfn). The signals generated from nontarget analytes suggest that the functionalized sensor is specific to the target at each biomarker's native OF. Additionally, it should be noted that the Lfn protein is present at 1000X the concentration of IgE. The minimal resulting signal suggests that the sensors are specific to their target analytes, with limited binding to undesired species. Although the signals from IgE's high and low concentrations (Figure 23B) are similar to blank, T-tests show that statistical difference ( $P$  value  $< 0.05$ ) exists among all data points in Figure 22F except the 120 ng/mL and 160 ng/mL combination. Further optimization of the surface chemistry is required to achieve clinical utility with this sensor. However, the current platform is sufficient for exploring the theory of native OF.

### Stability Testing

Given the simple yet crude immobilization approach, stability testing was performed to investigate the retainment of biological activity and functionality of the MREs after a specified duration. The calibration lines generated at the native OFs after one week of storage at 4°C are shown in Figures 24a and 24b. In comparison to the purified responses, both sensors exhibit increased



baseline impedance following storage. This can be explained by the concept of antibody permeation into the pores of the graphite working electrode creating a stronger barrier to electron flow. The increasing impedance magnitude has masked signal at the lowest antigen concentrations, increasing the LOQ, effectively decreasing sensitivity to low biomarker concentrations. This can be overcome by further optimization of the GA incubation conditions to adjust the degree of MRE crosslinking. Overall, the biological activity is retained after one week as supported by the performance similarity to purified responses.

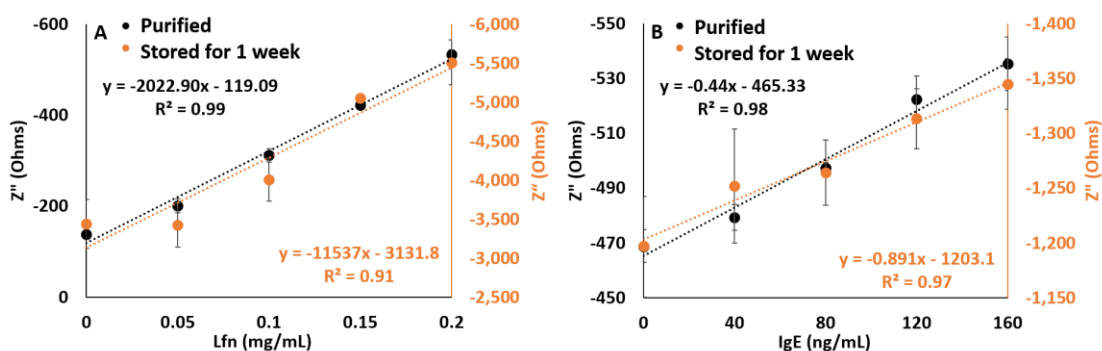


Figure 24: Stability Testing of the Lfn and IgE SPCE-Alpha. The SPCE-alpha responses in both purified (immediately tested) and one-week storage are shown for Lfn (A) and IgE (B), respectively. Each concentration was replicated 3 times. Reprinted with permission from reference 9. © American Chemical Society.

#### Complex Medium

To evaluate the ability to detect in complex samples, analyte testing in simulated tear fluid was performed using the SPCE-alpha platform. The sensor responses, depicted in Figure 25, validate the functionality of the platform in the presence of electroactive species and large proteins such as bovine serum albumin, lysozymes, and immunoglobulins. The calibration lines shown in Figures 25a and 25b were constructed at each biomarker's native OF. The calculated LOQs for Lfn and IgE sensors are 0.05 mg/mL and 40 ng/mL, respectively, satisfying the clinically relevant cut-off of 1.1 mg/mL and 80 ng/mL, respectively<sup>31,33</sup>. The reported Lfn sensor detection limit is comparable to other work<sup>181</sup>, however, superior IgE assays surpass the current capabilities of the simplistic, investigational platform described within<sup>54</sup>. Although the slopes vary in comparison to

purified samples, the correlations obtained at the native OFs suggest the clinical utility of this platform, and the imaginary impedance algorithm.

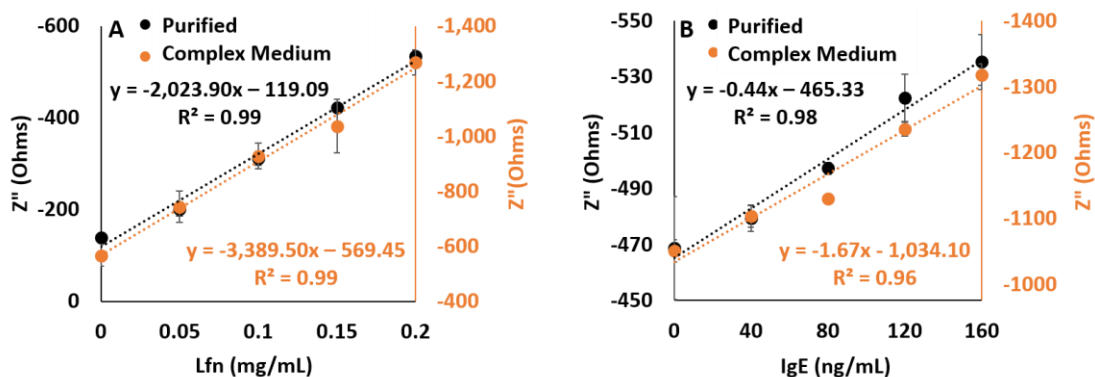


Figure 25: Complex Medium Testing of the Lfn and IgE SPCE-Alpha. The SPCE-alpha responses in both purified and complex solutions are shown for Lfn (A) and IgE (B). Each concentration was replicated 5 times. Reprinted with permission from reference 9. © American Chemical Society.

Notably, an increase in baseline impedance is present as compared to purified sample responses. This phenomenon can be attributed to the presence of electroactive species and large proteins causing an obstruction to electron flow through the system. Additionally, molecules such as BSA, have been previously incorporated into electrochemical applications for their effective blocking capabilities<sup>182</sup>. The non-specific adsorption of BSA to unabsorbed bare electrode and immobilized antibody is likely to raise the baseline impedance suggesting the need for additional calibration in complex medium prior to sample testing.

The results from Figures 22-25 also validate the potential of EIS to overcome the well-known weaknesses of physical adsorption-based immobilization. The GA-mediated physical adsorption is a well-studied immobilization technique achieved through primary amine cross-linking, which typically results in loss of antibody activity because of randomized orientation. Unlike other works that utilize GA crosslinking with SAMs<sup>183,184</sup>, the proposed approach directly immobilizes the antibody complex onto the carbon sensor surface. The reduction in antibody activity from physical adsorption seems to be compensated by the sensitivity of EIS at the native OF, as demonstrated

by the retainment of high slope and RSQ values. This combination has demonstrated success by achieving clinically relevant detection and shows potential in developing a much faster and simpler immobilization protocol to facilitate mass industrial fabrication.

### *Robustness of Biomarker's Native OF*

To investigate the robustness of a biomarker's native OF, the overlay of slope and RSQ values, under various testing conditions (purified buffer, simulated tears, and one week of storage) are presented in Figure 26. The results suggest that although the overall slope values vary with testing conditions, the native OFs remain consistent (vertical lines) as reflected by the RSQ values. This discovery suggests that the determination of native OF should not rely on the response alone, as the OF determined from these methods represent the entire electrochemical

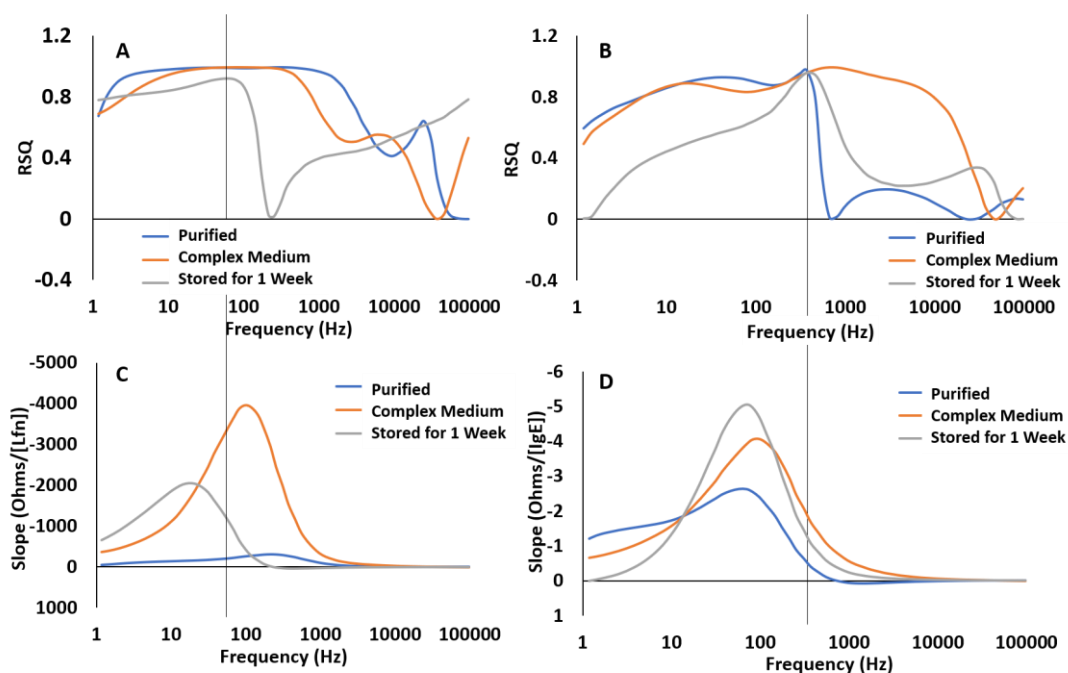


Figure 26: Robustness of the Native OF. Shows the robustness of native OFs in two mediums of varying electroactive properties (PBS and simulated tears) and after one week of storage using the SPCE-alpha platform. The optimal frequencies of Lfn (A,C) and IgE (B,D) remain 57.44 Hz and 371 Hz, respectively based on RSQ values (shown by vertical lines). Reprinted with permission from reference 9. © American Chemical Society 2018.

cell, which can change depending on the testing medium and other sensor conditions. The native OF should also not be the frequency at which the slope is significantly low. Although previously hypothesized, this is the first report that provides supporting evidence of the existence of a biomarker-specific OF<sup>170</sup>. The authors acknowledge the potential ambiguity of the RSQ-based algorithm when multiple frequencies exhibit very high RSQ values (i.e. 0.99). Further studies at the molecular level are needed to investigate the resonant frequency of a protein, and assess its comparison to the native OF discovered with EIS.

Nevertheless, IgE and Lfn can still be accurately detected in complex medium at each biomarker's native OF. By obtaining the response at a biomarker's native OF, the assay time and hardware requirements for the measuring system can be reduced.

#### *Factors that May Affect a Biomarker's Native OF*

OF measurements obtained across different immobilization methods are compared in Table 4. Previously, Lin *et al* used SAM-coated gold sensors to immobilize low-density lipoprotein (LDL) and high-density lipoprotein (HDL) antibodies. The algorithm used by Lin *et al* to identify the corresponding OF was maximum slope and RSQ greater than 0.95. The resulting OFs for LDL and HDL have been previously identified as 81.38 and 5.49 Hz, respectively. In comparing the LDL and HDL results with this work, it is interesting to note that biomarkers with larger combined molecular weight (antibody-antigen complex) exhibit higher OFs, irrespective of sensor substrate materials and immobilization chemistries. It is also interesting to note that, despite similar combined molecular weights of HDL and IgE antibody-antigen complexes, the reported OFs are hundreds of Hz apart (5.49 Hz and 371.1 Hz, respectively). Although molecular weight is unlikely the only factor affecting the native OF of a biomarker, the difference in OFs between HDL and IgE suggests that SAMs can influence the determination of a biomarker's native OF.

On the other hand, the association and dissociation constants do not hold the same correlation across both platforms. Immobilization strategies and chemistries interact with the antibodies on a molecular level. Randomized immobilization, such as the GA crosslinking method, can affect the kinetics of antigen binding sites, altering the association and dissociation constants to a greater extent than site-directed immobilization techniques<sup>185, 71,186</sup>

	<i>Lin et al</i>		This Work	
<b>Immobilization Chemistry</b>	<b>SAM with EDC/NHS coupling</b>		<b>GA-mediated physical adsorption</b>	
<b>Biomarkers</b>	<b>LDL</b>	<b>HDL</b>	<b>IgE</b>	<b>Lfn</b>
<b>Optimal Frequency (Hz)</b>	<b>81.38</b> <sup>[1]</sup>	<b>5.49</b> <sup>[1]</sup>	<b>371.1</b>	<b>57.44</b>
<b>Target Size (kDa)</b>	<b>512</b> <sup>[70]</sup>	<b>175</b> <sup>[70]</sup>	<b>190</b> <sup>[a]</sup>	<b>80</b> <sup>[185]</sup>
<b>Antibody Size (kDa)</b>	<b>150</b>	<b>150</b>	<b>150</b> <sup>[a]</sup>	<b>150</b>
<b>Combined Target-Antibody Size (kDa)</b>	<b>662</b>	<b>325</b>	<b>340</b>	<b>230</b>
<b>Association Constant (M<sup>-1</sup>)</b>	<b>1.3x10<sup>10</sup></b> <sup>[70]</sup>	<b>2.9x10<sup>10</sup></b> <sup>[70]</sup>	<b>3.0x10<sup>10</sup></b> <sup>[a]</sup>	<b>3.3x10<sup>8</sup></b> <sup>[185]</sup>
<b>Dissociation Constant (M)</b>	<b>7.7x10<sup>-11</sup></b>	<b>3.5x10<sup>-11</sup></b>	<b>3.3x10<sup>-11</sup></b> <sup>[a]</sup>	<b>3.0x10<sup>-9</sup></b> <sup>[185]</sup>

Table 4: Comparison of the OFs of low density lipoprotein (LDL), high density lipoprotein (HDL), IgE, and Lfn with respect to their antigen size, antibody size, association constant, and dissociation constant. Reprinted with permission from reference 9. © American Chemical Society. <sup>a</sup>: obtained from manufacturer specification sheet

## Transforming the Testing Platform to a POC Sensor Prototype (SPCE-beta)

### Electrochemical Evaluation

After verifying the specificity and stability of the sensor using SPCE-alpha platforms, the TSC was integrated to form the SPCE-beta, a large-scale prototype for the proposed POC application.

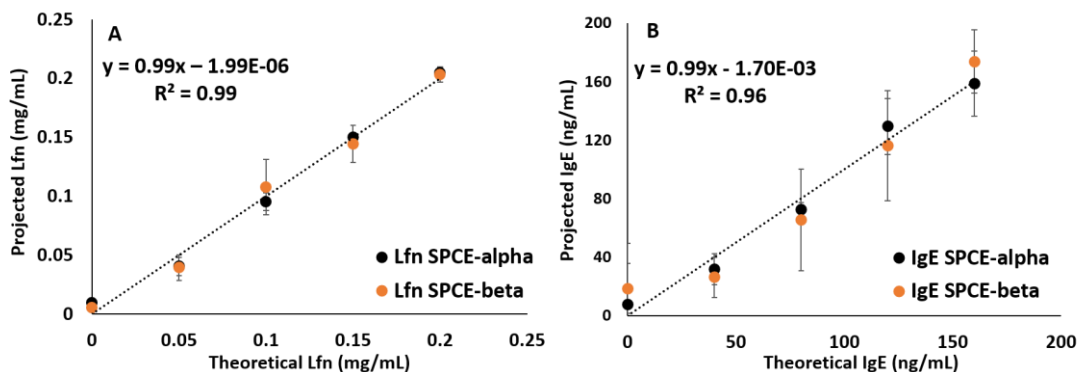


Figure 27: Calibration Curves of the IgE and Lfn Sensor Prototypes. Linear regression comparing the platform projected response to the theoretical analyte concentration for both biomarkers Lfn (A) and IgE (B). The error bars represent one standard error. Each concentration was replicated 5 times. Reprinted with permission from reference 9. © American Chemical Society.

Figure 27 shows the projected antigen concentrations by each respective calibration line for the SPCE-alpha and beta platforms, at each biomarker's native OF. The response of SPCE-beta is similar to that of SPCE-alpha, suggesting its capability in predicting analyte concentrations.

### Significance of the Integrated Sensor

The integration of TSCs onto a disposable sensor platform is a major improvement to the field of ocular diagnostics. Typically, the collection of tear samples is done using either glass capillary tubes or Schirmer's test strips. By utilizing the same material as a Schirmer's test strip, the safety and substantial equivalency of the TSC for FDA approval is well-supported. A hand-held meter that secures the test strip during sample collection and performs EIS is currently under development.

Schirmer's test strip applications have been thought to cause eye irritation and reflex tearing, causing changes in tear composition and protein concentrations<sup>187</sup>. However, a recent study found that the total amount of protein collected from Schirmer's strip is no different from those utilizing capillary tubes<sup>188</sup>, suggesting no ocular stress was inflicted. This is perhaps due to more sophisticated manufacturing developments in recent years resulting in enhanced biocompatibility of the paper<sup>188</sup>.

In light of these discoveries, the TSC prototype requires less than 20 seconds to collect 15  $\mu\text{L}$  of sample. The envisioned final Lfn integrated sensor design will collect 0.5  $\mu\text{L}$  of sample in less than a second, while the final IgE sensor will collect 5  $\mu\text{L}$  in 10 seconds (data not shown). The required ocular contact time is decreased from the standard 60 second collection time to 1-10 seconds, promising little to no risk of ocular irritation or discomfort.

We have also considered the potential for sample evaporation when a low (< 1  $\mu\text{L}$ ) volume is taken. Based on preliminary data, we estimate minimal evaporation (< 7%) after 60 seconds. The amount of evaporation is thus not believed to affect EIS results.

User or patient acceptance of the tear sampling technique is another important consideration in POC ocular diagnostics since stress and irritation can cause variations in concentrations of analytes, thereby increasing result variation<sup>189</sup>. In this regard, Schirmer's test strips are less risky, as capillary tube methods require well-trained personnel and potentially longer contact with the eye. According to one survey, almost all subjects were more apprehensive about rigid glass capillary tubes as compared to flexible filter paper<sup>188</sup>. In addition, samples collected using Schirmer's test strips demonstrated increased reproducibility as compared to those gathered using capillary tubes<sup>190,191</sup>. After miniaturization, we expect the proposed sensors with integrated TSCs to cause minimal stress and irritation, yielding high patient acceptance.

The proposed integrated sensor can also be translated to other diseases whose biomarkers are present in tears. Hagan *et al* reported that tear fluid contains many analytes related to diseases in areas as diverse as endocrinology, oncology, the central nervous system and others<sup>192</sup>. Tear fluid is easily accessible in comparison to blood and requires no sample preparation unlike serum or tissue samples. We believe that the proposed integrated sensor, once optimized and miniaturized, will be able to rapidly obtain an accurate biomarker concentration without the inconvenience associated with needle pricking and expensive, complicated test kits. This POC sensor platform is an economical means of screening, diagnosing, and managing many diseases.

## CONCLUSIONS

We have acquired deeper insight into the existence of a biomarker's native OF by directly measuring the Z" responses of two example biomarkers using a physical adsorption functionalization method. We confirmed the robustness of a biomarker's native OF in various testing conditions including complex medium, suggesting its utility as an additional means of detecting specific biomarkers. We found that the OFs may be dependent on the combined molecular weight of the MRE-target complex, and this relationship is upheld across two sensor preparation methods. We have also demonstrated that a sensitive technique, like EIS, can overcome the limitations of simplistic adsorption-based immobilization methods and achieve clinically relevant cutoff values. The transformation of the investigative platform into a practical POC sensor prototype through the novel integration of Schirmer's strip as a TSC, permitting a convenient, quantitative, and rapid sensor for two biomarkers commonly used in differentiating DED from ocular allergy, is also shown. The proposed GA-mediated immobilization may benefit from further optimization to make it an attractive technology for clinical use. Future efforts of this work are focused on the optimization and miniaturization of the system for manufacturing purposes and diversifying the range of biomarkers and diseases to which this technology can be adapted.



*Acknowledgement:* The content of this work was adapted from the submitted manuscript in reference 11, which was accepted by ACS *Sensors*. The author received permission to reproduce the content from the coauthors and the publisher should the manuscript is eventually published. The author would like to specially thank Mackenzie Honikel for assisting the experiments and editing the manuscript.

## CHAPTER 3.2

### THE EFFECT OF ZETA POTENTIAL, CONDUCTIVITY, AND MOLECULAR WEIGHT ON A BIOMARKER'S OPTIMAL FREQUENCY

#### INTRODUCTION

In the previous chapter, through the development of various multi-marker sensor prototypes, the identification of a biomarker's optimal frequency has enabled EIS to detect two proteomic biomarkers simultaneously<sup>1</sup>. The optimal frequency has also provided a rapid and sensitive means to detect target analytes<sup>5,9</sup>. It was also However, although the idea of optimal frequency is well accepted<sup>130–133,146</sup>, signal overlapping may prohibit the detection of multiple biomarkers if their optimal frequencies are too close together<sup>144,145,163,193,194</sup>. To overcome this, La Belle *et al* reported that nanoparticles conjugated to a biomarker's MRE can be used to tune its optimal frequency without affecting its biological activity<sup>166,170,195</sup>. Another alternative to signal overlapping is the use of imaginary impedance ( $Z''$ ) based algorithm for optimal frequency determination, which was used to measure two biomarkers simultaneously on a single working electrode without the use of nanomaterials<sup>1</sup>. However, as shown in the dual-enzymatic biomarker setup, signal decoupling with  $Z''$  impedance is not a remedy for all signal overlapping issues. Nevertheless, the  $Z''$  algorithm and the use of nanoparticles would be an interesting combination to explore for more options to separate the signal and achieve the multi-marker sensor.

In addition, since there is little understanding about the origin of a biomarker's optimal frequency, the engineering's Design of Experiment principle can be implemented to begin investigating potential factors that contribute to a biomarker's optimal frequency. Herein, we investigated three example factors: zeta potential, conductivity, and molecular weight. The zeta potential provides an estimation of a target molecule's surface charge with respect to the surrounding medium<sup>196</sup>. The conductivity measures the molecule's ability to conduct electrical current. The molecular weight measures how large or dense the molecules are. All three factors can potentially alter the

electrochemical properties of the target MRE-target complex and consequently the optimal frequencies. Using the Z" algorithm, we employed a dual approach to observe the changes in optimal frequency with respect to these three factors. The first approach was the biomarker setup, in which three distinct example biomarkers' optimal frequencies were investigated. The second approach was the nanoparticle setup, in which five types of nanoparticles were individually conjugated to an example biomarker's MRE to shift its optimal frequency as inspired by LaBelle *et al's* work<sup>166,170,195</sup>. Since the nanoparticles have very different properties compared to biomolecules, they are ideal candidates to expand the high and low levels of the three exemplary factors. Finally, analysis of variance (ANOVA) was used to conclude which factors are significantly affecting the optimal frequencies. This study also allowed the expansion of nanoparticle rosters for tuning the optimal frequency in addition to LaBelle *et al's* work<sup>166,170,195</sup>. The three exemplary factors could serve as a crucial explanation to the origin of a biomarker's optimal frequency and lay a solid foundation for further works. This work could be used to substantiate the design metrics of customizing a multi-marker detection platform toward various complex diseases. The knowledge can also be translated to expand the applications of EIS, such as the nondestructive quality assessments of biosensors and pharmaceutical drugs.

## METHODS

### *Materials*

All chemical reagents were purchased from Sigma (St Louis, MO) unless stated otherwise. The 10-mM phosphate buffer (PBS) tablets were purchased from Calbiochem (Gibbstown, NJ). The potassium hexacyanoferrate (III) was purchased from EMD Chemicals (Billerica, MA), and N-hydroxysulfosuccinimide sodium salt (NHS) from Toronto Research Chemicals (Toronto, Ontario, Canada). The streptavidin coated gold nanoparticles (AuNPs) and streptavidin coated magnetic nanoparticles (MagNP) were purchased from Nanocs (New York, NY). The streptavidin coated zinc sulfide/cadmium selenide quantum dots (Qdots) were purchased from Invitrogen (Waltham, MA). The biotinylated IL-12 antibody was purchased from Thermo Fisher (Waltham, MA). The

mouse monoclonal antibody specific to immunoglobulin E (IgE) and IgE antigen were obtained from Scripps Laboratories (San Diego, CA). The human monoclonal antibody for human lactoferrin was obtained from Fitzgerald (Acton, MA). The recombinant human lactoferrin was obtained from Agennix (Houston, TX).

### *Sensor Preparation*

#### *Sensors Used in The Biomarker Setup*

The electrochemical cell was made of a gold disc working electrode (GDE), a silver/silver chloride reference electrode, and a platinum (Pt) counter electrode. All electrodes were purchased from CH Instruments (Austin, TX). The electrochemical cell could hold 100  $\mu$ L with 2 mm being the diameter of a GDE. All sensor fabrication steps were performed at room temperature and in 7.4 pH. The GDE preparation protocol described in Appendix X was adapted. After the activation of carboxylic groups of the SAM, 10 mg/mL of glucose oxidase, 50  $\mu$ g/mL of IgE antibody, or 50  $\mu$ g/mL of lactoferrin antibody were immobilized onto the GDEs. After rinsing with PBS, 1% ethanolamine was used to block the unreacted SAM. The sensors were used immediately. Each biomarker's antibody concentration was previously optimized to detect the target at its physiological range.

#### *Sensors Used in The Nanoparticle Setup*

The sensors used in the nanoparticle setup were prepared in a similar manner described above until the activation of SAM. After activating the carboxylic groups, 50  $\mu$ g/mL of biotinylated IL-12 antibody prepared in 10 mM PBS at pH 7.4 was incubated with the GDEs for 1 hour. After antibody immobilization,  $3.89 \times 10^{11}$  particles/mL of various streptavidin coated nanomaterials were incubated for 1 hour, followed by a 30-minute incubation with 1% ethanolamine to block the unreacted SAM. The streptavidin coated nanomaterials used were 5 nm AuNP, 10 nm AuNP, 20 nm AuNP, 25 nm MagNP, and 20 nm QDot. The sensors were used immediately. All nanomaterials' concentrations were kept at the same concentration ( $3.89 \times 10^{11}$  particles/mL) to

expand on Demirok et al and LaBelle et al's preliminary work on shifting the optimal frequency<sup>166,170,195</sup>. A schematic of all sensor setups can be found in Figure 28.

### Electrochemical Measurements

All electrochemical measurements were performed at room temperature using a CHI660C Electrochemical Analyzer from CH Instrument. The cyclic voltammetry from -1.0V to 1.0V was performed to determine the formal potential of each GDE in 100  $\mu$ L of 100 mM potassium ferricyanide. All EIS measurements were performed at each GDE's formal potential with 5 mV

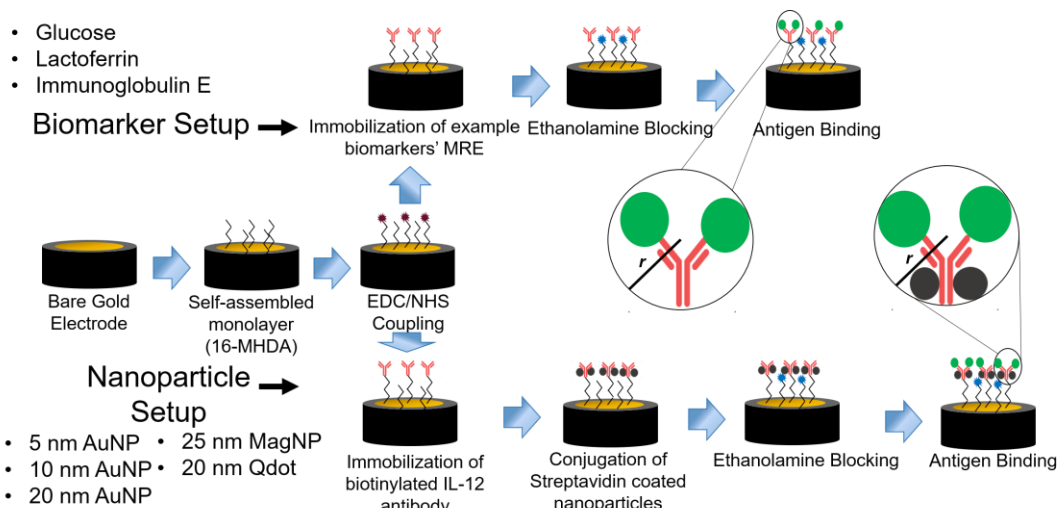


Figure 28: Sensor setup for the investigation of optimal frequency. Schematic presentation of sensor preparation methods for the biomarker setup and the nanoparticle setup, as well as the biomarkers tested, and the nanoparticles utilized. The zoom-in represents the boundary condition of the local system and its hydrodynamic radius.

amplitude sweeping from 100,000 Hz to 1 Hz in a resolution of 12 points per decade. The testing solution for each EIS measurement was made of 50  $\mu$ L of sample and 50  $\mu$ L of 200 mM potassium ferricyanide. All measurements were performed at pH 7.4 and replicated 3 times using 3 separate GDEs.

#### *Biomarker Setup: Measuring the Optimal Frequencies of Various Example Biomarkers*

To measure the optimal frequency of each biomarker, the sensors immobilized with each biomarker's MREs were tested against their respective targets. The tested concentrations of glucose, lactoferrin, and IgE were 0 – 100 mg/dL, 0 – 2.5 mg/mL, and 0 – 1 mg/mL, respectively. All biomarkers' concentrations were tested at their physiological ranges<sup>33,48,197</sup>. The glucose concentrations are intentionally expressed in mg/dL because of its wide clinical practice. The biomarkers were selected based on their drastic differences in molecular weight.

#### *Nanoparticle Setup: Measuring the Optimal Frequencies of Various Nanoparticle-Antibody Conjugations*

To validate successful conjugations, after conjugating the IL-12 antibodies with various nanoparticles, a "blank EIS" was performed using PBS without the presence of IL-12 antigens, and the results were compared to an unconjugated control. To evaluate the subsequent optimal frequency of each nanoparticle-antibody conjugation, 0 – 5000 pg/mL gradient of IL-12 antigen was added to the sensors and tested electrochemically. The IL-12 concentration covers its physiological levels<sup>198</sup>.

#### *Determination of Optimal Frequency*

The optimal frequency was determined by the frequency at which maximum slope occurs after correlating the "Z" values against target biomolecule's concentrations. This method is selected to allow the use of cutoff frequency for modeling and data analysis.

#### *Characterization of Nanomaterials and Biomolecules*

The molecular weight of each nanomaterial was calculated based on manufacturers' specifications. The molecular weight of each biomarker's antigens was obtained from manufacturers. A Delsa Nano C from Beckman Coulter (Brea, CA) was used to measure the zeta potential and conductivity of the nanoparticles and biomolecules. One mL of each sample was

brought to room temperature prior to measurements. To achieve stable measurements of zeta potential that are independent from concentrations, all nanomaterials were kept above 1E-4 %w/v as suggested by previous works<sup>199,200</sup>. The glucose, lactoferrin, and IgE were all tested at 1 mg/mL. All measurements were repeated 10 times per the instrument's built-in protocol and were performed at pH 7.4. The zeta potential and conductivities were calculated using the built-in software of Delsa Nano C.

#### *Modeling of Optimal Frequencies*

An Excel Add-on called XLSTAT was used to perform the ANOVA for modeling the zeta potential, conductivity, and molecular weight against the optimal frequency.

## RESULTS AND DISCUSSIONS

#### *Studying the Optimal Frequencies Using the Biomarker Setup*

The electrochemical responses and optimal frequencies of the example biomarkers are presented in Figure 29. The  $Z''$  values were dependent on the concentrations of each biomarker's analyte as demonstrated in Figure 29A – 29C. Figure 29D and 29E shows the optimal frequencies of individual biomarkers after correlating the  $Z''$  values with corresponding antigens' concentration gradients. The optimal frequencies enabled the detection of these distinctly different biomarkers at their physiological ranges. The optimal frequencies for IgE, lactoferrin, and glucose are 371.1 Hz, 175.8 Hz, and 37.6 Hz, respectively. It appeared that larger biomarkers (IgE > lactoferrin > glucose) have higher optimal frequency as discovered previously<sup>1</sup>, which will be further elaborated in later sections.

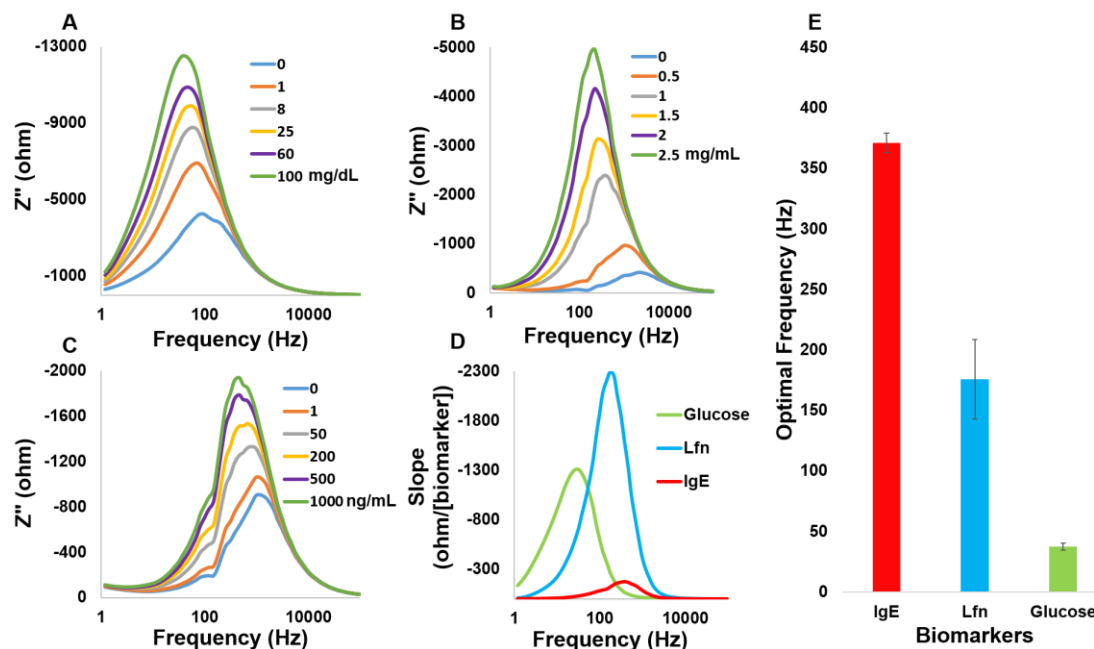


Figure 29: Determination of example biomarkers' optimal frequencies. A) Overlay of  $Z''$  response on glucose sensors with varying glucose concentrations. B) Overlay of  $Z''$  response of lactoferrin sensors with varying lactoferrin concentrations. C) Overlay of  $Z''$  response of IgE sensors with varying lactoferrin concentrations. D) Overlay of slopes. E) Comparison of optimal frequencies of example biomarkers.

### *Studying the Optimal Frequencies Using the Nanoparticle Setup*

#### *Confirming the Conjugation of Nanoparticles*

The  $Z''$  responses of the antibody-nanoparticle complexes in a solution containing only PBS and the potassium ferricyanide are shown in Figure 30. The result suggests that successful conjugation of nanoparticles changed the capacitance and resistance of the electrochemical cell, causing a system-wide effect that can be observed in: 1) the shift in the cutoff frequency ( $f_c$ , the frequency at which  $-Z''$  is maximum, summarized in Table 5); 2) either sharper or broader  $Z''$  concave across the frequency spectrum; and 3) different magnitudes of  $Z''$ .



Nanoparticle-Antibody Conjugation	Without IL-12 Antigen: Cutoff Frequency (Hz)	With IL-12 Antigen: Optimal Frequency (Hz)
Control	37.56	14.36
5 nm AuNP	253.9	69.75
10 nm AuNP	69.75	21.23
20 nm AuNP	14.36	3.09
25 nm MagNP	81.38	81.38
20 nm Qdot	371.1	214.8

Table 5: Summary of the cutoff frequencies and the optimal frequencies of each nanoparticle conjugates.

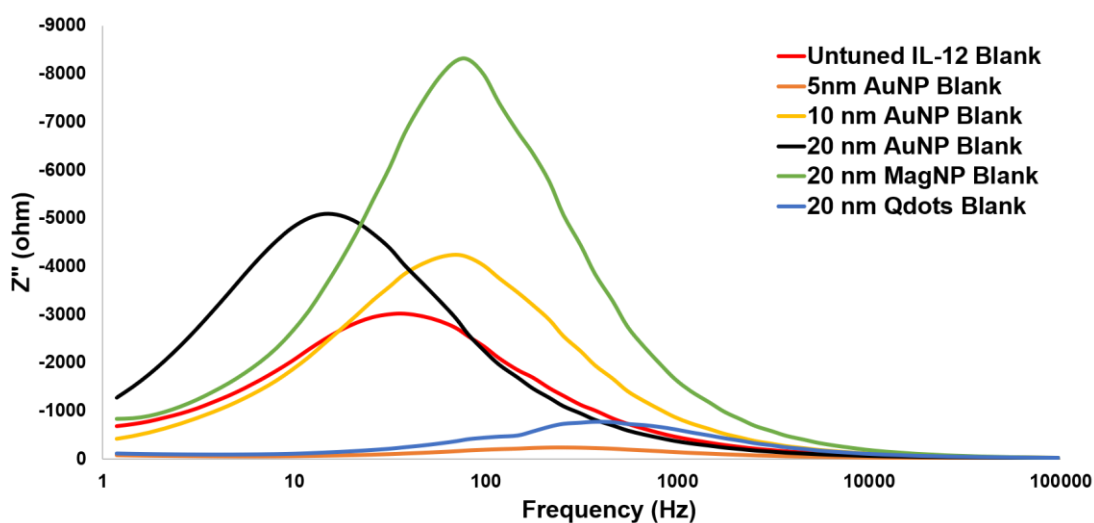


Figure 30: EIS responses of various types of nanoparticle conjugations to the IL-12 antibody.

#### Characterization of the Nanoparticle-Antibody Complexes

Following the successful conjugation of nanoparticles, the optimal frequencies of various nanoparticle-antibody complexes were characterized. Using the 20 nm AuNP conjugation as an example, Figure 31A shows an example  $Z''$  response of the 20 nm AuNP conjugation after

introducing a concentration gradient of IL-12 antigen (0 – 5000 pg/mL). The  $Z''$  response increased proportionally with IL-12 antigen concentrations, but the cut-off frequencies decreased gradually. The full results can be found in supplementary information. For each type of nanoparticle-antibody conjugation, after correlating the  $Z''$  values at each frequency to the IL-12 antigen concentrations, the resulting slopes are shown in Figure 31B. The optimal frequency of each type of antibody-nanoparticle conjugation is shown in Figure 31C. The cut-off frequencies from Figure 30 and the optimal frequencies from Figure 31C are summarized in Table 5 for comparison.

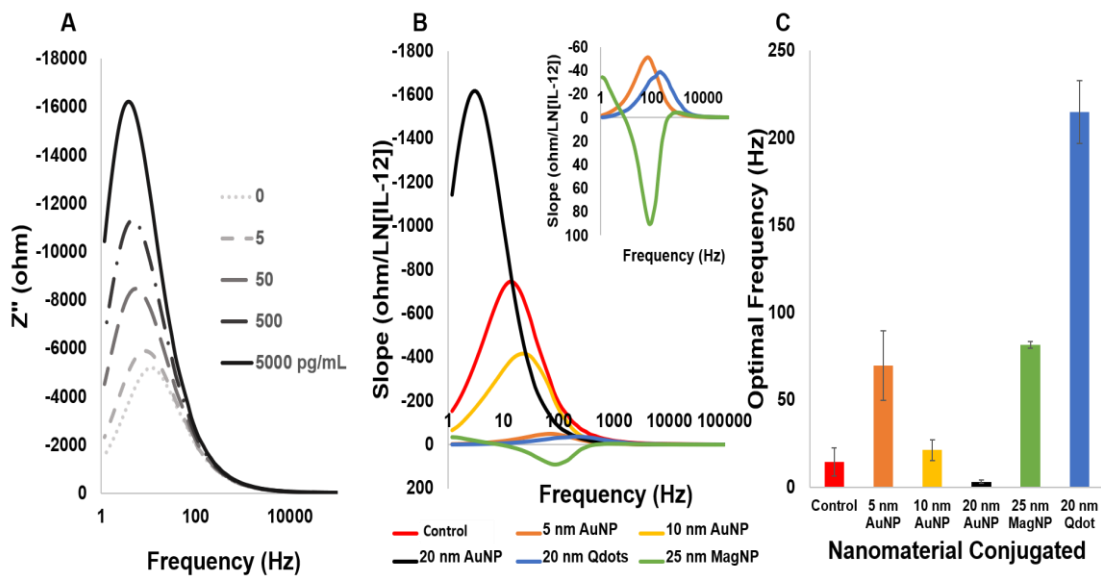


Figure 31: EIS responses of various nanomaterials in the presence of IL-12 antigen. A) Exemplary  $Z''$  overlay of the IL-12 antibody conjugated with 20 nm AuNP showing the change in  $Z''$  and the shift in cut-off frequencies when exposed to 0 – 5000 ng/mL gradient of IL-12 antigen. The  $Z''$  at each frequency was correlated to IL-12 antigen to obtain slopes. B) Overlay of slopes of each type of nanoparticle-antibody conjugations after correlating the  $Z''$  values to the IL-12 antigen concentrations. The inset represents the zoom-in for 5 nm AuNP, 20 nm Qdots, and 25 nm MagNP. C) Comparison of optimal frequency after conjugating the IL-12 antibody with various types of nanoparticles.

Figure 31B suggests that the slope from MagNP conjugation is reversed compared to other nanomaterials. Generally, the  $Z''$  values are negative because of the complex number  $j$ , as shown in the equation below.

$$Z(j\omega) = Z_r(\omega) + jZ_i(\omega) \quad \text{Equation 13}$$

The binding of IL-12 to the antibody is expected to restrict the flow of electrons, resulting in an increase in  $Z''$  (more negative) and a negative slope. The increase in  $Z''$  values are typically proportional to the increase in IL-12 concentration. The only exception was MagNP, which had a positive  $Z''$  slope and a poor R-square (RSQ) value at the optimal frequency, suggesting that the  $Z''$  values did not correlate with IL-12 antigen concentrations (see Figures 32 and 33). The result was unexpected because the MagNPs have been widely used in the development of biosensors, as they enhance electron transfer and increase the shelf-life of electrodes<sup>201,202</sup>. Besides the potential of forming large agglomerates due to magnetic dipole-dipole interactions between particles<sup>203</sup>, another possible explanation is the competitive reaction. At the formal potential, the potassium ferricyanide is converted back and forth between its oxidized (ferricyanide) and reduced (ferrocyanide) states to constantly facilitate electron flows in the electrochemical cell. Iron oxide can exchange electrons between the Fe centers, going back and forth from Fe<sup>II</sup> to Fe<sup>III</sup> based on the potential applied<sup>204</sup>. The MagNPs of iron oxide are also known for enhancing spin-spin T2 relaxation time by dephasing the spins of water protons nearby<sup>205</sup>. Therefore, there may be competition of electrons between the ferron ions in the iron oxide of MagNP and that in the potassium ferricyanide. Subsequently, the presence of electron competitions may affect the electron flow and the charge distribution around the immobilized MagNP-antibody complex, preventing the change in  $Z''$  from correlating with IL-12 binding.

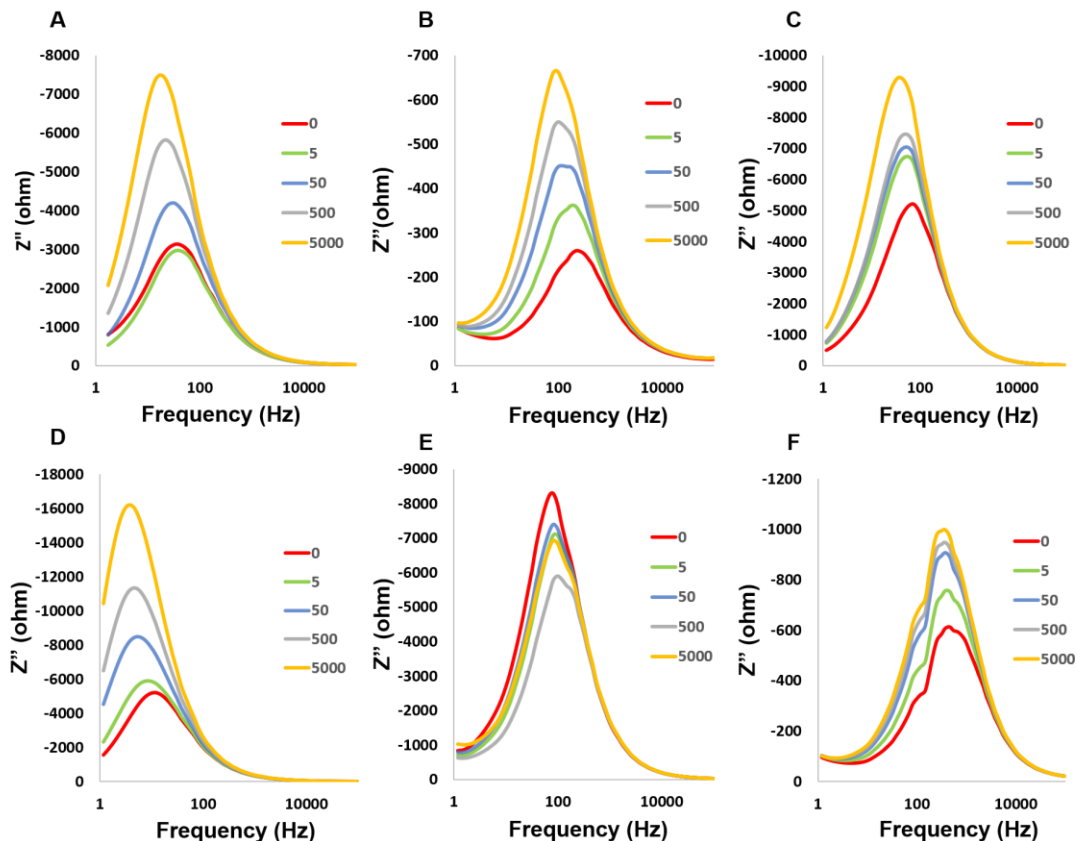


Figure 32: Overlay of imaginary impedance ( $Z''$ ) responses of biotinylated IL-12 antibody that are conjugated with A) no nanoparticles (NP), B) 5 nm gold NP, C) 10 nm gold NP, D) 20 nm gold NP, E) 25 nm magnetic NP, and F) 20 nm quantum dots before applying a gradient (0-5000 pg/mL) of IL-12 antigens.

Despite reducing the slope drastically, the Qdots seem to have tuned the optimal frequency furthest from the control when compared to the other nanoparticles. Due to its two-metal layer design (zinc sulfide shell and cadmium selenide core), the Qdots may be represented as a double layer capacitor and cause a charge bias on the surface of the nanoparticle-antibody complex. The capacitive effect may explain why Qdots had the greatest impact on the optimal frequency compared to other homogeneous nanoparticles, as further elaborated later.

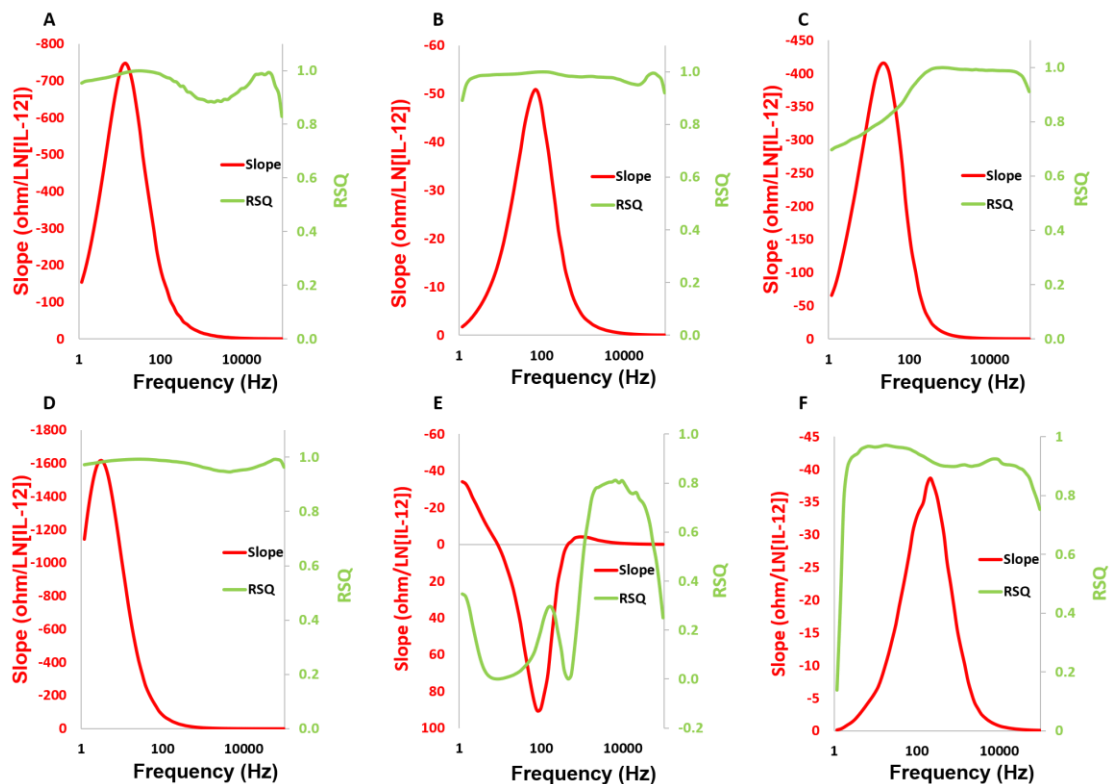


Figure 33: Overlay of slope and R-square (RSQ) values of biotinylated IL-12 antibody that are conjugated with A) no nanoparticles (NP), B) 5 nm gold NP, C) 10 nm gold NP, D) 20 nm gold NP, E) 25 nm magnetic NP, and F) 20 nm quantum dots after correlating the  $Z''$  values with IL-12 concentrations.

Judging from the shift of optimal frequencies in the antibody-NP complexes of 5 nm AuNP, 10 nm AuNP, and 20 nm AuNP when compared to the control, the  $Z''$  algorithm confirmed Demirok *et al's* work in that the size of AuNPs have an inversely proportional effect on tuning the optimal frequency<sup>195</sup>. However, as evident in Figure 31C, the relationship was nonlinear when involving magnetic and quantum nanoparticles, suggesting additional factors should be examined.

#### *Measuring Zeta Potential, Conductivity, and Molecular Weight*

The values of zeta potential, conductivity, and molecular weight for each nanoparticle and biomarker's analyte can be found in Table 6. Their individual correlations with the optimal frequency can be found in Figure 34. The result in Figure 34A suggests that although the

conductivity seems to be affecting the optimal frequency, because of its parabolic relationship, there may be interactions among the 3 exemplary factors. The result in Figure 34B suggests that the zeta potential is positively correlated with the optimal frequency, meaning that when the zeta potential increases (less negative), the optimal frequency increases. The result in Figure 34C suggests that the molecular weight is negatively correlated with the optimal frequency. As the molecular weight decreases, the optimal frequency increases. Note that the values from glucose were consistently found to be outliers. This could be attributed to the enzymatic reaction between glucose and glucose oxidase. Besides glucose, all other MRE-target reactions were either through the covalent binding between biotin and streptavidin, or the affinity-based binding between the antibody and antigen. The enzymatic reaction of glucose is not only different in the nature of MRE-target interaction, but also generates electrons, which could significantly alter the flux of electrons in the electrochemical system, causing an undesirable contamination for this modeling. In a hindsight, although glucose was able to provide the smallest molecular weight for this design of experiment, the result suggested that since the enzymatic reactions followed a different mechanism, a separate design of experiment using only the enzymatic-based biomarkers would be more appropriate to study their optimal frequencies. The zeta potential,

conductivity, and molecular weight values of glucose were thus removed from the subsequent ANOVA study but were kept in Figure 34 as references.

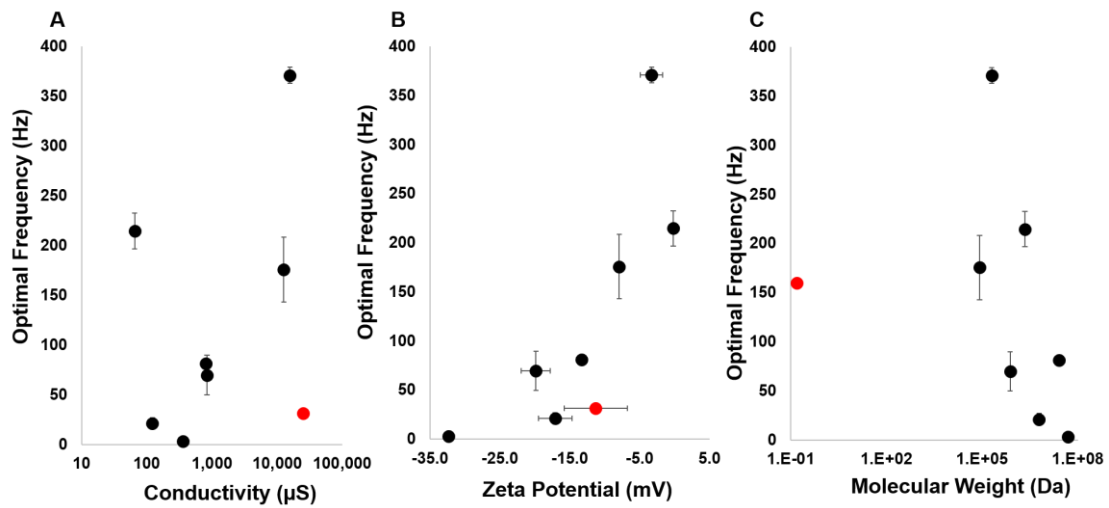


Figure 34: The effect of conductivity, zeta, and molecular weight on the optimal frequency. A) the parabolic relationship between the conductivity and the optimal frequency, B) the positive correlation between the zeta potential and optimal frequency, and C) the negative correlation between the molecular weight and the optimal frequency. The red dots represent data points from glucose.

<b>Material</b>	<b>Zeta Potential (mV)</b>	<b>Conductivity (<math>\mu</math>S)</b>	<b>Molecular Weight (Da)</b>	<b>Optimal Frequency (Hz)</b>
<b>5 nm AuNP</b>	-19.84	840.00	761,494	69.75
<b>10 nm AuNP</b>	-17.09	122.00	6,091,951	21.23
<b>20 nm AuNP</b>	-32.34	360.10	48,735,608	3.09
<b>25 nm MagNP</b>	-13.31	811.93	25,816,692	81.38
<b>20 nm Qdot</b>	-0.185	65.00	2,182,003	214.8
<b>Glucose</b>	-11.31	24955.07	160	37.60
<b>Lactoferrin</b>	-7.93	12599.85	80,000	175.80
<b>IgE</b>	-3.29	15660.57	200,000	371.10

Table 6: Summary of each nanoparticle and biomarker analyte's zeta, conductivity, molecular weight, and optimal frequency.

*Using ANOVA to Determine the Factors and Interactions that Contribute to the Optimal Frequency*

Finally, ANOVA was used to examine which factors and interactions among the zeta potential, conductivity, and molecular weight were significantly affecting the optimal frequency. A complete table summarizing the details of ANOVA can be found in Table 7. All factors and interactions were found to be statistically significant (P value < 0.05). The regression analysis yielded a model that predicts the optimal frequency:



$$LN(F_o) = 6.26 - 8.15E^{-5}\sigma + 0.11\zeta - 4.14E^{-7}m - 4.07E^{-6}\sigma\zeta + 3.64E^{-10}\sigma m - 7.62E^{-9}\zeta m$$

Equation 14

where  $LN(F_o)$  is the natural log of optimal frequency,  $\sigma$  the conductivity,  $\zeta$  the zeta potential, and  $m$  the molecular weight. The model is statistically significant (P value < 0.0001) and unbiased, as supported by the randomized pattern in the residual plot (Figure 35A) and good linearity ( $R^2 = 0.99$ , Figure 35B).

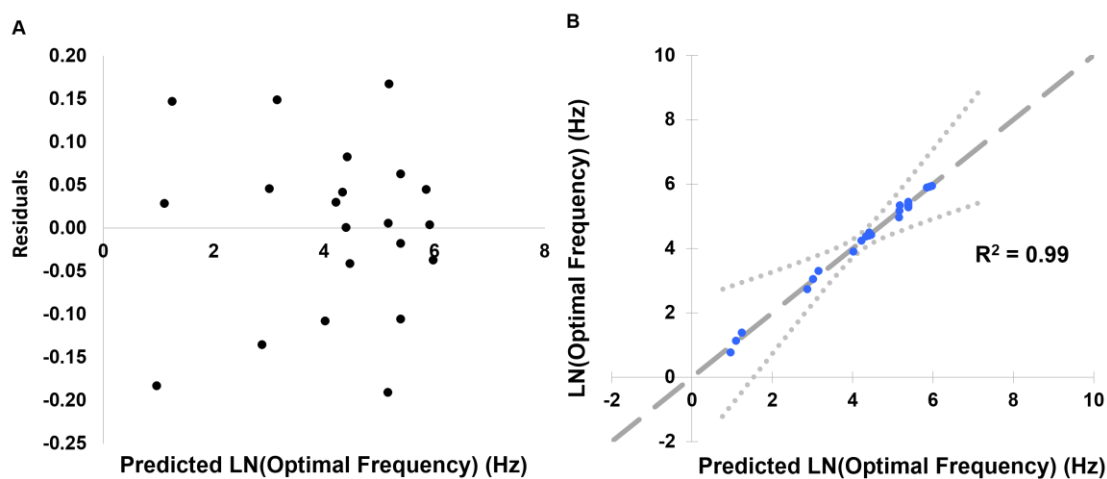


Figure 35: Modeling of optimal frequency. Linear regression results showing: A) residual plots with random pattern and B) the modeled response compared to the experimental data. Dotted grey lines represent 95% confidence interval.

Analysis of Variance					
Source	Degree of Freedom	Sum of Squares	Mean Squares	F Value	P Value
<b>Model</b>	6	49.174	8.196	561.447	< 0.0001
<b>Conductivity</b>	1	0.594	0.594	40.689	< 0.0001
<b>Zeta</b>	1	6.195	6.195	424.387	< 0.0001
<b>Molecular Weight</b>	1	2.752	2.752	188.552	< 0.0001
<b>Conductivity X Zeta</b>	1	0.110	0.110	7.557	0.016
<b>Conductivity X Molecular Weight</b>	1	3.240	3.240	221.955	< 0.0001
<b>Zeta X Molecular Weight</b>	1	1.941	1.941	132.989	< 0.0001
<b>Error</b>	14	0.204	0.015	N/A	N/A

Table 7: Summary of the ANOVA results

*An Unbiased Means for Studying the Optimal Frequency*

The optimal frequency differs from the cutoff frequency in that it is the frequency at which the biomarker can be quantified sensitively and accurately (Figure 29D and Figure 31B). Some researchers interpreted it as a native optimal frequency between the antibody and the antigen (and thus independent from nonspecific binding or biofouling)<sup>138,166</sup>, while others interpreted it merely as a single-frequency that reflects system-wide changes<sup>130–133</sup>. Although the idea of optimal frequency is well advocated, there is no universally agreed method to determine a biomarker's optimal frequency. The scope of this manuscript is not to establish the optimal method for determining the optimal frequency, but to provide an unbiased means to study the factors that can affect the optimal frequency. The Z" algorithm used in this work is beneficial in

providing a visual presentation as the cut-off frequency is easily observable. Although the cut-off frequency is slightly different from the optimal frequency in that the cut-off frequency is concentration dependent, it is a well-understood concept describing the electrochemical system and is in close resemblance to the optimal frequency regardless of the algorithm used, making it an unbiased model for explaining the factors that contribute to the optimal frequency. Binding of antigens gradients will change the local accumulation of charges around the antibody-antigen complex, causing a shift in the cut-off frequency observed in Figure 29A – 29C, and Figure 31A. The cut-off frequency ( $f_c$ ) can be modeled as:

$$f_c = \frac{1}{RC2\pi} \quad \text{Equation 15}$$

where R is resistance and C the capacitance. The equation can be used to explain the changes of optimal frequencies discovered in both the biomarker and nanoparticle setups with respect to zeta potential, molecular weight, and conductivity, as the binding of nanomaterials and target analytes to the antibody is expected to change the complex's overall resistance and the capacitance. The inset of Figure 28 can be used as the boundary condition for the following discussions.

#### *Factors that Significantly Affect the Optimal Frequency*

The values of zeta potential and conductivity of nanoparticles and biomarker analytes were measured in a free-flowing model, which was different from the immobilized model used herein. This was partly because measuring these values after the immobilization would be technically challenging. However, by keeping the control factors as consistent as experimentally possible, such as the concentration of immobilized antibodies, molecular weight of the MREs (all MREs utilized in this study were between 150 kDa to 160 kDa), and the concentration of the nanoparticles, the changes in optimal frequencies could be attributed from mainly the binding of antigens and/or the nanoparticle conjugations. Besides being popular biocompatible materials in

many biomedical applications, the nanoparticles also have very different characteristics. They're expected to vary the antibody-antigen complex's zeta, conductivity, and molecular weight drastically, allowing us to study which factors significantly contribute to the optimal frequency. From the results in Figure 34 and 35, zeta potential, conductivity, and molecular weight are all factors that can significantly impact the optimal frequency, suggesting that the local charge accumulation and distribution around the antibody-antigen complex can be responsible for a biomarker's optimal frequency. In the following sections we discuss each parameter individually with respect to Equation 15.

### *Zeta Potential*

Zeta potential is generally defined as the electrostatic potential at the interfacial double layer between the particles and the surrounding mediums. It is often measured to estimate the stability of the nanoparticles, as nanoparticles with high zeta potential tend to repulse instead of coagulating<sup>206</sup>. It can also be extended to provide a simple estimation of a molecule's surface charge. The large error bars on the zeta potentials could be attributed to the coating of streptavidin, a 55 kDa protein. According to manufacturer information, due to the polydispersity of size (around 15%~20% coefficient of variation), the number of streptavidin on the nanoparticles are also expected to vary. The presence of streptavidin extended the double layer and consequently affected the zeta potential, so variance in the number of streptavidin could cause variance in the zeta potential. The excitation wavelength of the dynamic light scattering instrument (Delsa Nano C) was also very close to the emission maximum of Qdots (655 nm), potentially causing an underestimation of its zeta potential. Nevertheless, as shown in Figure 34B, a P value of < 0.0001 suggested that zeta potential can significantly affect the optimal frequency. In general, higher negative charge on the surface of particles might restrict the flow of electrons and thus increase the charge transfer resistance, therefore corresponding to the lower optimal frequency recorded<sup>207</sup> according to Equation 15 and the trend observed in Figure 34B.

### *Molecular weight*

According to Figure 34C, an increase in the molecular weight of a molecule results in a decrease in the optimal frequency. The increase in molecular weight may cause steric hindrance and close packing limitations near the electrode surface. As the electron flows through the antibody-antigen or nanoparticle-antibody-antigen complexes are obstructed. A larger molecular weight can be attributed to the size and/or density of the molecule. Assuming both the antigen-antibody and the nanoparticles-antibody-antigen complexes (referred to as antibody complex herein) are spheres with a hydrodynamic radius of  $r$  (Figure 28), their resistance and capacitance can be modeled as:

$$R = \rho \frac{2\pi r}{\pi r^2} = \rho \frac{2}{r} \quad \text{Equation 16}$$

$$C = \frac{2\pi\epsilon_0\epsilon_r}{1+\frac{d}{r}} \quad \text{Equation 17. Adopted from Chaki *et al*^{208}}$$

where  $\rho$  is the resistivity,  $\epsilon_0$  the dielectric constant of the sphere,  $\epsilon_r$  the permittivity of the medium, and  $d$  the distance between the antibody-antigen complex and the surface of the electrode. According to Equation 16 and 17, when the molecular weight changes, the change in size and/or density can be reflected in  $r$  and  $d$ , resulting in a change in the resistance and capacitance.

However, changing the molecular weight can also affect the  $\rho$  and  $\epsilon_0$  of the antibody complex due to the alternating current applied in the EIS and a change in the close packing factor<sup>209–211</sup>, affecting the resistance and capacitance of the antibody complex. Since  $r$  and  $d$  are in the denominator and  $\rho$  and  $\epsilon_0$  the numerator, altering the molecular weight will have trade-off effects depending on the magnitudes of these factors. Judging from Equation 15 and the trend in Figure 34C, an increase in the molecular weight suggests an overall increase in the resistance and the capacitance, meaning that the growths in  $\rho$  and  $\epsilon_0$  are more dominant than that of  $r$  and  $d$ . In other words, an increase in the molecular weight would affect the electron flows inside the antibody

complex, increase both its resistance and the capacitance, and thus lower the cutoff frequency and consequently the optimal frequency according to Equation 15.

Increasing the molecular weight can also lead to a larger surface area for charge accumulation, affecting the zeta potential around the particles and consequently the antibody complex.

Therefore, there is a significant interaction between the zeta potential and molecular weight according to Table 7.

### *Conductivity*

According to Figure 34A, conductivity is also a factor that significantly affects the optimal frequency. The conductivity measures how the electrons flow through a material and is the reciprocal of resistivity. Using the similar boundary conditions above, the conductivity of the antigen and the nanoparticles can also affect the conductivity of the overall complex.

Subsequently, the flow of electrons through the complex to the electrode is affected. Therefore, conductivity of the overall system can affect the resistance in the equivalent circuit, consequently affecting the optimal frequency.

In addition, according to Figure 34A and Table 7, the significant interaction between the conductivity and zeta can also affect the optimal frequency. Since zeta potential is an estimation of the surface charge between the molecule and the surrounding medium, the repulsion among molecules can affect the electron flow through the antibody complex as well. Therefore, the interaction between conductivity and zeta can affect the resistance and capacitance of the antibody complex, and consequently the optimal frequency.

Lastly, the significant interaction between the conductivity and molecular weight can also affect the optimal frequency. The conductivity of the antibody complex can be modeled as:

$$\sigma = \sigma_0 e^{-Ea/RT} \quad \text{Equation 18, obtained from Brust } et al^{12}$$

$$E_a = \frac{e^2}{8\pi\epsilon_0\epsilon_r} \left( \frac{1}{r} - \frac{1}{r+d} \right) \text{ Equation 19, derived from Brust et al}^{12}$$

where  $\sigma_0$  is the conductivity constant,  $E_a$  the activation energy,  $R$  the universal gas constant,  $T$  the temperature, and  $e$  the charge of an electron. As described above, since a change in the molecular weight may also affect  $\rho$ ,  $\epsilon_0$ ,  $r$ , and  $d$ , the conductivity of the entire antibody complex is also expected to change, affecting the resistance and consequently the optimal frequency.

#### *Limitation of the Work*

This work did not investigate other potential factors that could impact the optimal frequency, such as pH, temperature, protein integrity, medium, molecule orientation, and many others. The three factors studied in this work was assumed to be the three strongest candidates based on literature search and available resources. Further studies are required to gain deeper understanding on the origin of optimal frequencies and what exactly they are.

#### *Applications of Optimal Frequencies*

There are various applications for leveraging the optimal frequency. First, it shortens the hardware requirement and assay time to detect target analytes without sacrificing specificity. This is especially attractive when detecting molecules at very low physiological concentration such as insulin, which resides as low as 50 pM in the body<sup>5</sup>, making it possible to develop point-of-care biosensors for biomarkers which are otherwise very costly and time-consuming to measure. Second, it offers a means to measure various analytes simultaneously on a single electrode, which helps improve the specificity and sensitivity of many assays with improved cost-efficiencies<sup>1</sup>. Furthermore, by understanding the factors that contribute to the optimal frequency, it can be used in many applications from interrogating the different interfaces and membranes<sup>213</sup> to the aggregation of biomolecules, providing a rapid and nondestructive means for quality control. A great example application would be the quality control in commercialized insulin vials, which was found to be as low as 40.2 U/mL versus the advertised 95 U/mL<sup>67</sup>.

## CONCLUSION

In conclusion, we have demonstrated the effect of zeta potential, conductivity, and molecular weight on a biomarker's optimal frequency through the studies containing five types of nanoparticles and three biomarkers. The ability to model and predict a biomarker's optimal frequency would serve great use in the design of next generation sensors. However, we have not yet fully understood and validated the concept of optimal frequency. First, different binding mechanisms that generate electrical signal or conformational changes should be explored as they can significantly alter the resistance and capacitance of the electrochemical system and consequently the optimal frequencies. Second, different space groups and lattice structures can be explored to better understand how structure orientations and stacking can affect the optimal frequency. By understanding what constitutes the optimal frequency of a biomarker, it can emerge as an additional means of rapid characterization of biomolecules with countless applications.

*Acknowledgement:* The content of this work was submitted to *ACS Analytical Chemistry* on 2/16/18, in which the author is the first author. The author has received the consents from coauthors to reproduce the material. The author would like to thank Dr. Duong Nguyen, Dr. Brittany Cardinell, David Probst, and Aldin Malkoc for assisting with the experiments. The author would also like to thank B. Sullivan, NIH Library Editing Service, for manuscript editing assistance.



## CHAPTER 4

### SUMMARY AND FUTURE WORK

Monitoring complex diseases and their comorbidities requires accurate and convenient measurements of multiple biomarkers. However, many state-of-the-art bioassays not only require complicated and time-consuming procedures, but also measure only one biomarker at a time. To achieve the label free, multi-marker electrochemical sensing platform for the management of complex diseases and their comorbidities, seven biomarkers representing DM, CVD, and DED were investigated. An imaginary impedance-based algorithm for the determination of optimal frequency and signal deconvolution was first developed to enable EIS multi-marker detection and the study of biomarkers' optimal frequencies. It was found that, by monitoring the imaginary impedance response at the biomarker's optimal frequency, sensitive single-marker detection (glucose, lactate, insulin, lactoferrin, and immunoglobulin E) can be achieved. The Mayo Clinic sponsored EIS insulin sensor was especially a major development as it not only has the potential to improve glycemic control, but can also serve as a rapid, nondestructive quality control of commercial insulin vials. The Advanced Tears Diagnostic sponsored lactoferrin and immunoglobulin E biosensors also provided a practical means for point-of-care dry eye diagnostic. Besides the academic research of investigating factors that contribute to the optimal frequencies, the sponsorship from hospital and industry has transformed these single-marker biosensors into practical experiences in designing for manufacturing, business presentations, and design of experiments.

The imaginary impedance algorithm has also overcome the signal overlapping in the multi-marker detection, resulting in the development of a dual-proteomic marker (low-density lipoprotein and high density lipoprotein) sensor. The dual-enzymatic marker (glucose and lactate) sensor was not successful due to the local accumulation of reduced redox mediator on the self-assembled monolayer (SAM). SAM is a long, electrically insulating spacer intended to provide the chemical group for protein immobilization. It works fine in proteomic biomarkers, but for enzymatic

biomarkers that generate electrons as enzymatic reaction occurs, the electron insulating character of SAM was found to limit the electron transport of redox mediator, causing a local accumulation of reduced redox mediator on SAM, and thus contaminated the impedance signal generated from enzymatic reactions. Study platforms not involving the use of SAM may be warranted to accurately study the optimal frequencies of enzymatic biomarkers.

Throughout the exploration, three exemplary factors were found to contribute to the optimal frequency of a biomarker: zeta potential, conductivity, and molecular weight. Amperometric, disposable test strips integrated with samplers were also developed for lactate and glucose as a backup to the multi-marker platform. This work has resulted in a national award (U.S. Metrohm Young Chemist Award), a \$1.5 million grant from the Leona M. and Harry B. Helmsley Charitable Trust, 9 publications, 4 patents, and 4 submitted manuscripts. However, despite these successes, complex medium in many developed biosensors (except lactoferrin and Immunoglobulin E biosensors) have not been tested. The LDL-HDL dual-marker sensor has also not been tested in complex medium either. These biosensors should be tested in blood to validate its clinical utility.

The author plans to continue the investigation of proteomic and enzymatic biomarkers' optimal frequency in the grant award from the Helmsley Trust by developing the dual insulin-glucose sensor. In this endeavor, not only an animal study will be performed to validate the developed EIS insulin and glucose sensors, it has the opportunity to mature and commercialize the EIS multimarker technology.

## REFERENCES

- (1) Lin, C.; Ryder, L.; Probst, D.; Caplan, M.; Spano, M.; LaBelle, J. Feasibility in the Development of a Multi-Marker Detection Platform. *Biosens. Bioelectron.* **2016**, *89*, 743–749.
- (2) Lin, C.; Pratt, B.; Honikel, M.; Jenish, A.; Ramesh, B.; Alkhan, A.; La Belle, J. T. Toward the Development of a Glucose Dehydrogenase-Based Saliva Glucose Sensor Without the Need for Sample Preparation. *J. Diabetes Sci. Technol.* **2017**, 1932296817712526.
- (3) Lin, C.-E.; Honikel, M. M.; LaBelle, J. A Multi-Marker Approach for Improved Glycemic Management in Diabetes Mellitus. *J. Diabetes Metab. Disord. Control* **2017**, *4* (5).
- (4) Aldin Malkoc; Chi Lin; David Probst; Mackenzie Honikel; Jeffrey T. La Belle. Towards the Future Development of an Electrochemical Continuous Multimarker Biosensor for Enhanced Glycemic Management. *J. Diabetes Sci. Technol.* **2017**, *11* (5), 1053–1054.
- (5) Malkoc, A.; Probst, D.; Lin, C.; Khanwalker, M.; Beck, C.; Cook, C. B.; La Belle, J. T. Enhancing Glycemic Control via Detection of Insulin Using Electrochemical Impedance Spectroscopy. *J. Diabetes Sci. Technol.* **2017**, 1932296817699639.
- (6) La Belle, J. T.; Adams, A.; Lin, C.-E.; Engelschall, E.; Pratt, B.; Cook, C. B. Self-Monitoring of Tear Glucose: The Development of a Tear Based Glucose Sensor as an Alternative to Self-Monitoring of Blood Glucose. *Chem. Commun.* **2016**, *52* (59), 9197–9204.
- (7) Hiraka, K.; Kojima, K.; Lin, C.-E.; Tsugawa, W.; Asano, R.; La Belle, J. T.; Sode, K. Minimizing the Effects of Oxygen Interference on L-Lactate Sensors by a Single Amino Acid Mutation in *Aerococcus Viridans* L-Lactate Oxidase. *Biosens. Bioelectron.* **2018**, *103*, 163–170.
- (8) Lee, I.; Loew, N.; Tsugawa, W.; Lin, C.-E.; Probst, D.; La Belle, J. T.; Sode, K. The Electrochemical Behavior of a FAD Dependent Glucose Dehydrogenase with Direct Electron Transfer Subunit by Immobilization on Self-Assembled Monolayers. *Bioelectrochemistry* **2018**, *121*, 1–6.
- (9) Lin, C.-E.; Honikel, M.; Cardinell, B.; Penman, A.; La Belle, J. Direct Measurement of a Biomarker's Native Optimal Frequency with Physical Adsorption Based Immobilization. *ACS Sens.* **2018**, *3* (4), 823-831.
- (10) Lin, C.-E.; Ito, Y.; Deng, A.; Johns, J.; Matloff, D.; Cook, C.; Sode, K.; La Belle, J. A Disposable Tear Glucose Biosensor - Part 5: Improvements in Reagents and Design. *J. Diabetes Sci. Technol.* **2018**, *1* (5).
- (11) Honikel, M.; Lin, C.-E.; Probst, D.; La Belle, J. Facilitating Earlier Diagnosis of Cardiovascular Disease Through Point-of-Care Biosensors: A Review. *Crit. Rev. Biomed. Eng.* **2018**, *46* (1), 53-82.
- (12) Lin, C.-E.; Hiraka, K.; Matloff, D.; Johns, J.; Deng, A.; Sode, K.; La Belle, J. A Disposable Tear Lactate Sensor Integrated with Tear Capturing Component. *Sens. Actuators B Chem.* *In Press*.
- (13) Lin, C.-E.; Nguyen, D.; Probst, D.; La Belle, J. The Effects of Zeta Potential, Conductivity, and Molecular Weight on A Biomarker's Optimal Frequency. *Anal. Chem.* *Submitted*.

- (14) Olokoba, A. B.; Obateru, O. A.; Olokoba, L. B. Type 2 Diabetes Mellitus: A Review of Current Trends. *Oman Med. J.* **2012**, *27* (4), 269–273.
- (15) Centers for Disease Control. Number of Americans with Diabetes Expected to Double or Triple by 2050. *Retrieved April 2010*, 20, 2011.
- (16) American Diabetes Association. Economic Costs of Diabetes in the US in 2012. *Diabetes Care* **2013**, *36* (4), 1033–1046.
- (17) American Diabetes Association. Diagnosis and Classification of Diabetes Mellitus. *Diabetes Care* **2010**, *33* (Supplement 1), S62–S69.
- (18) Alberti, K. G. M. M.; Zimmet, P. ft. Definition, Diagnosis and Classification of Diabetes Mellitus and Its Complications. Part 1: Diagnosis and Classification of Diabetes Mellitus. Provisional Report of a WHO Consultation. *Diabet. Med.* **1998**, *15* (7), 539–553.
- (19) Struijs, J. N.; Baan, C. A.; Schellevis, F. G.; Westert, G. P.; van den Bos, G. A. Comorbidity in Patients with Diabetes Mellitus: Impact on Medical Health Care Utilization. *BMC Health Serv. Res.* **2006**, *6* (1), 84.
- (20) Santulli, G. Epidemiology of Cardiovascular Disease in the 21st Century: Updated Numbers and Updated Facts. *J Cardiovasc Dis* **2013**, *1* (1), 1–2.
- (21) Kelly, B. B.; Fuster, V. *Promoting Cardiovascular Health in the Developing World: A Critical Challenge to Achieve Global Health*; National Academies Press, 2010.
- (22) Hom, M. M.; Nguyen, A. L.; Bielory, L. Allergic Conjunctivitis and Dry Eye Syndrome. *Ann. Allergy Asthma Immunol. Off. Publ. Am. Coll. Allergy Asthma Immunol.* **2012**, *108* (3), 163–166.
- (23) Farrand, K. F.; Fridman, M.; Stillman, I. Ö.; Schaumberg, D. A. Prevalence of Diagnosed Dry Eye Disease in the United States among Adults Aged 18 Years and Older. *Am. J. Ophthalmol.* **2017**, *182*, 90–98.
- (24) Olokoba, A. B.; Obateru, O. A.; Olokoba, L. B. Type 2 Diabetes Mellitus: A Review of Current Trends. *Oman Med. J.* **2012**, *27* (4), 269–273.
- (25) Manaviat, M. R.; Rashidi, M.; Afkhami-Ardekani, M.; Shoja, M. R. Prevalence of Dry Eye Syndrome and Diabetic Retinopathy in Type 2 Diabetic Patients. *BMC Ophthalmol.* **2008**, *8* (1), 10.
- (26) AJ, J. A.; Colburn, W. A.; DeGruttola, V. G.; DeMets, D. L.; Downing, G. J.; Hoth, D. F.; Oates, J. A.; Peck, C. C.; Schooley, R. T.; Spilker, B. A. Biomarkers and Surrogate Endpoints: Preferred Definitions and Conceptual Framework. *Clin. Pharmacol. Ther.* **2001**, *69* (3), 89–95.
- (27) Sullivan, S. D.; Garrison Jr, L. P.; Rinde, H.; Kolberg, J.; Moler, E. J. Cost-Effectiveness of Risk Stratification for Preventing Type 2 Diabetes Using a Multi-Marker Diabetes Risk Score. *J. Med. Econ.* **2011**, *14* (5), 609–616.
- (28) Urdea, M.; Kolberg, J.; Wilber, J.; Gerwien, R.; Moler, E.; Rowe, M.; Jorgensen, P.; Hansen, T.; Pedersen, O.; Jørgensen, T. Validation of a Multimarker Model for Assessing Risk of Type 2 Diabetes from a Five-Year Prospective Study of 6784 Danish People (Inter99). **2009**.

- (29) Turksoy, K.; Samadi, S.; Feng, J.; Littlejohn, E.; Quinn, L.; Cinar, A. Meal Detection in Patients With Type 1 Diabetes: A New Module for the Multivariable Adaptive Artificial Pancreas Control System. *IEEE J. Biomed. Health Inform.* **2016**, *20* (1), 47–54.
- (30) Expert Panel on Detection, E. Executive Summary of the Third Report of the National Cholesterol Education Program (NCEP) Expert Panel on Detection, Evaluation, and Treatment of High Blood Cholesterol in Adults (Adult Treatment Panel III). *Jama* **2001**, *285* (19), 2486.
- (31) D'Souza, S.; Tong, L. Practical Issues Concerning Tear Protein Assays in Dry Eye. *Eye Vis.* **2014**, *1* (1), 6.
- (32) Qureshi, A.; Gurbuz, Y.; Niazi, J. H. Biosensors for Cardiac Biomarkers Detection: A Review. *Sens. Actuators B Chem.* **2012**, *171*, 62–76.
- (33) Baudouin, C.; Bourcier, T.; Brignole, F.; Bertel, F.; Moldovan, M.; Goldschild, M.; Goguel, A. Correlation between Tear IgE Levels and HLA-DR Expression by Conjunctival Cells in Allergic and Nonallergic Chronic Conjunctivitis. *Graefes Arch. Clin. Exp. Ophthalmol.* **2000**, *238* (11), 900–904.
- (34) Halade, G. V.; Jin, Y.-F.; Lindsey, M. L. Matrix Metalloproteinase (MMP)-9: A Proximal Biomarker for Cardiac Remodeling and a Distal Biomarker for Inflammation. *Pharmacol. Ther.* **2013**, *139* (1), 32–40.
- (35) Mahajan, R. Blood Test to Help Diagnose Type 1 Diabetes Approved by Food and Drug Administration. *Int. J. Appl. Basic Med. Res.* **2015**, *5* (1), 1.
- (36) Ling, J. C. Y.; Mohamed, M. N. A.; Jalaludin, M. Y.; Rampal, S.; Zaharan, N. L.; Mohamed, Z. Determinants of High Fasting Insulin and Insulin Resistance among Overweight/Obese Adolescents. *Sci. Rep.* **2016**, *6*, 36270.
- (37) Nikolaus, N.; Strehlitz, B. Amperometric Lactate Biosensors and Their Application in (Sports) Medicine, for Life Quality and Wellbeing. *Microchim. Acta* **2008**, *160* (1), 15–55.
- (38) Nagi, D. *Exercise and Sport in Diabetes*; John Wiley & Sons, 2006.
- (39) Sallach, S. M.; Nowak, R.; Hudson, M. P.; Tokarski, G.; Khoury, N.; Tomlanovich, M. C.; Jacobsen, G.; de Lemos, J. A.; McCord, J. A Change in Serum Myoglobin to Detect Acute Myocardial Infarction in Patients with Normal Troponin I Levels. *Am. J. Cardiol.* **2004**, *94* (7), 864–867.
- (40) Florvall, G.; Basu, S.; Larsson, A. Apolipoprotein A1 Is a Stronger Prognostic Marker than Are HDL and LDL Cholesterol for Cardiovascular Disease and Mortality in Elderly Men. *J. Gerontol. A. Biol. Sci. Med. Sci.* **2006**, *61* (12), 1262–1266.
- (41) Langsted, A.; Freiberg, J. J.; Nordestgaard, B. G. Fasting and Nonfasting Lipid Levels: Influence of Normal Food Intake on Lipids, Lipoproteins, Apolipoproteins, and Cardiovascular Risk Prediction. *Circulation* **2008**, *118* (20), 2047–2056.
- (42) Walldius, G.; Jungner, I. The ApoB/ApoA-I Ratio: A Strong, New Risk Factor for Cardiovascular Disease and a Target for Lipid-lowering Therapy—a Review of the Evidence. *J. Intern. Med.* **2006**, *259* (5), 493–519.

- (43) Stull, C.; Valdes-Rodriguez, R.; Shafer, B. M.; Shevchenko, A.; Nattkemper, L. A.; Chan, Y.-H.; Tabaac, S.; Schardt, M. J.; Najjar, D. M.; Foster, W. J. The Prevalence and Characteristics of Chronic Ocular Itch: A Cross-Sectional Survey. *Itch* **2017**, *2* (1), e4.
- (44) Leonardi, A.; Bogacka, E.; Fauquert, J. L.; Kowalski, M. L.; Groblewska, A.; Jedrzejczak-Czechowicz, M.; Doan, S.; Marmouz, F.; Demoly, P.; Delgado, L. Ocular Allergy: Recognizing and Diagnosing Hypersensitivity Disorders of the Ocular Surface. *Allergy* **2012**, *67* (11), 1327–1337.
- (45) Rosario, N.; Bielory, L. Epidemiology of Allergic Conjunctivitis. *Curr. Opin. Allergy Clin. Immunol.* **2011**, *11* (5), 471–476.
- (46) Hom, M. M.; Nguyen, A. L.; Bielory, L. Allergic Conjunctivitis and Dry Eye Syndrome. *Ann. Allergy. Asthma. Immunol.* **2012**, *108* (3), 163–166.
- (47) Sullivan, D. A.; Dartt, D. A.; Meneray, M. A. *Lacrimal Gland, Tear Film, and Dry Eye Syndromes 2: Basic Science and Clinical Relevance*; Springer Science & Business Media, 2012; Vol. 438.
- (48) Beckman, K. A.; Luchs, J.; Milner, M. S. Making the Diagnosis of Sjögren's Syndrome in Patients with Dry Eye. *Clin. Ophthalmol. Auckl. NZ* **2016**, *10*, 43.
- (49) Gupta, A. *Clinical Ophthalmology: Contemporary Perspectives*; Elsevier Health Sciences, 2012.
- (50) Fujishima, H.; Toda, I.; Shimazaki, J.; Tsubota, K. Allergic Conjunctivitis and Dry Eye. *Br. J. Ophthalmol.* **1996**, *80* (11), 994–997.
- (51) Hamilton, R. G. Accuracy of US Food and Drug Administration–cleared IgE Antibody Assays in the Presence of Anti-IgE (Omalizumab). *J. Allergy Clin. Immunol.* **2006**, *117* (4), 759–766.
- (52) La Rosa, M.; Lionetti, E.; Reibaldi, M.; Russo, A.; Longo, A.; Leonardi, S.; Tomarchio, S.; Avitabile, T.; Reibaldi, A. Allergic Conjunctivitis: A Comprehensive Review of the Literature. *Ital. J. Pediatr.* **2013**, *39* (1), 18.
- (53) Chin, C. D.; Linder, V.; Sia, S. K. Commercialization of Microfluidic Point-of-Care Diagnostic Devices. *Lab. Chip* **2012**, *12* (12), 2118–2134.
- (54) Kreuzer, M.; O'Sullivan, C.; Pravda, M.; Guilbault, G. Development of an Immunosensor for the Determination of Allergy Antibody (IgE) in Blood Samples. *Anal. Chim. Acta* **2001**, *442* (1), 45–53.
- (55) Su, X.; Chew, F. T.; Li, S. F. Self-Assembled Monolayer-Based Piezoelectric Crystal Immunosensor for the Quantification of Total Human Immunoglobulin E. *Anal. Biochem.* **1999**, *273* (1), 66–72.
- (56) American Diabetes Association. Diagnosis and Classification of Diabetes Mellitus. *Diabetes Care* **2010**, *33* (Supplement 1), S62–S69.
- (57) Bakker, J.; Nijsten, M. W.; Jansen, T. C. Clinical Use of Lactate Monitoring in Critically Ill Patients. *Ann. Intensive Care* **2013**, *3* (1), 12.

- (58) Faude, O.; Kindermann, W.; Meyer, T. Lactate Threshold Concepts: How Valid Are They? *Sports Med.* **2009**, *39* (6), 469.
- (59) Rassaei, L.; Olthuis, W.; Tsujimura, S.; Ernst, J.; Sudhölter, R.; van den Berg, A. Lactate Biosensors: Current Status and Outlook. *Anal. Bioanal. Chem.* **2014**, *406* (1), 123.
- (60) Nguyen, H. B.; Rivers, E. P.; Knoblich, B. P.; Jacobsen, G.; Muzzin, A.; Ressler, J. A.; Tomlanovich, M. C. Early Lactate Clearance Is Associated with Improved Outcome in Severe Sepsis and Septic Shock. *Crit. Care Med.* **2004**, *32* (8), 1637–1642.
- (61) Thent, Z. C.; Das, S.; Henry, L. J. Role of Exercise in the Management of Diabetes Mellitus: The Global Scenario. *PLoS One* **2013**, *8* (11), e80436.
- (62) Goodwin, M. L.; Harris, J. E.; Hernández, A.; Gladden, L. B. Blood Lactate Measurements and Analysis during Exercise: A Guide for Clinicians. *J. Diabetes Sci. Technol.* **2007**, *1* (4), 558–569.
- (63) Hovorka, R.; Canonico, V.; Chassin, L. J.; Haueter, U.; Massi-Benedetti, M.; Federici, M. O.; Pieber, T. R.; Schaller, H. C.; Schaupp, L.; Vering, T. Nonlinear Model Predictive Control of Glucose Concentration in Subjects with Type 1 Diabetes. *Physiol. Meas.* **2004**, *25* (4), 905.
- (64) Cameron, F.; Bequette, B.; Wilson, D.; Buckingham, B. Detecting Insulin Infusion Set Failure. *Adv. Technol. Treat. Diabetes* **2012**.
- (65) Baysal, N.; Cameron, F.; Buckingham, B. A.; Wilson, D. M.; Bequette, B. W. Detecting Sensor and Insulin Infusion Set Anomalies in an Artificial Pancreas; IEEE, 2013; pp 2929–2933.
- (66) Del Favero, S.; Monaro, M.; Facchinetti, A.; Tagliavini, A.; Sparacino, G.; Cobelli, C. Real-Time Detection of Glucose Sensor and Insulin Pump Faults in an Artificial Pancreas. *IFAC Proc. Vol.* **2014**, *47* (3), 1941–1946.
- (67) Carter, A. W.; Heinemann, L. Insulin Concentration in Vials Randomly Purchased in Pharmacies in the United States: Considerable Loss in the Cold Supply Chain. *J. Diabetes Sci. Technol.* **2017**, 1932296817747292.
- (68) Harfenist, E. J.; Craig, L. C. The Molecular Weight of Insulin. *J. Am. Chem. Soc.* **1952**, *74* (12), 3087–3089.
- (69) Benjamin, E. J.; Blaha, M. J.; Chiuve, S. E.; Cushman, M.; Das, S. R.; Deo, R.; Floyd, J.; Fornage, M.; Gillespie, C.; Isasi, C. Heart Disease and Stroke Statistics-2017 Update: A Report from the American Heart Association. *Circulation* **2017**, *135* (10), e146–e603.
- (70) Fernandez, M. L.; Webb, D. The LDL to HDL Cholesterol Ratio as a Valuable Tool to Evaluate Coronary Heart Disease Risk. *J. Am. Coll. Nutr.* **2008**, *27* (1), 1–5.
- (71) Miller, Y. I.; Shaklai, N. Kinetics of Hemin Distribution in Plasma Reveals Its Role in Lipoprotein Oxidation. *Biochim. Biophys. Acta BBA-Mol. Basis Dis.* **1999**, *1454* (2), 153–164.
- (72) Sharrett, A. R.; Ballantyne, C.; Coady, S.; Heiss, G.; Sorlie, P.; Catellier, D.; Patsch, W. Coronary Heart Disease Prediction from Lipoprotein Cholesterol Levels, Triglycerides, Lipoprotein (a), Apolipoproteins AI and B, and HDL Density Subfractions: The

- Atherosclerosis Risk in Communities (ARIC) Study. *Circulation* **2001**, *104* (10), 1108–1113.
- (73) Timofeev, V.; Chuprov-Netochin, R.; Samigina, V.; Bezuglov, V.; Miroshnikov, K.; Kuranova, I. X-Ray Investigation of Gene-Engineered Human Insulin Crystallized from a Solution Containing Polysialic Acid. *Acta Crystallograph. Sect. F Struct. Biol. Cryst. Commun.* **2010**, *66* (3), 259–263.
- (74) Doré, K. A.; Davies, A. M.; Drinkwater, N.; Beavil, A. J.; McDonnell, J. M.; Sutton, B. J. Thermal Sensitivity and Flexibility of the Cε3 Domains in Immunoglobulin E. *Biochim. Biophys. Acta BBA-Proteins Proteomics* **2017**, *1865* (11), 1336–1347.
- (75) Zweig, S. E. Dual Glucose-Turbidimetric Analytical Sensors. **2010**.
- (76) Eggers, M. D.; Hogan, M. E.; Beattie, K. L.; Shumaker, J.; Ehrlich, D. J.; Hollis, M. Multi Site Molecule Detection Method. **1997**.
- (77) Lu, W.; Fu, C.; Chen, Y.; Lu, J.; Yao, Y.; Shen, C.; Gu, Z. Multiplex Detection of B-Type Natriuretic Peptide, Cardiac Troponin I and C-Reactive Protein with Photonic Suspension Array. *PLoS ONE* **2012**, *7* (7), e41448.
- (78) Magliulo, M.; Simoni, P.; Guardigli, M.; Michelini, E.; Luciani, M.; Lelli, R.; Roda, A. A Rapid Multiplexed Chemiluminescent Immunoassay for the Detection of Escherichia Coli O157: H7, Yersinia Enterocolitica, Salmonella Typhimurium, and Listeria Monocytogenes Pathogen Bacteria. *J. Agric. Food Chem.* **2007**, *55* (13), 4933–4939.
- (79) Damborský, P.; Švitel, J.; Katrlík, J. Optical Biosensors. *Essays Biochem.* **2016**, *60* (1), 91–100.
- (80) Zenneck, J. Über Die Fortpflanzung Ebener Elektromagnetischer Wellen Längs Einer Ebenen Leiterfläche Und Ihre Beziehung Zur Drahtlosen Telegraphie. *Ann. Phys.* **1907**, *328* (10), 846–866.
- (81) Lausted, C.; Hu, Z.; Hood, L. Quantitative Serum Proteomics from Surface Plasmon Resonance Imaging. *Mol. Cell. Proteomics* **2008**, *7* (12), 2464–2474.
- (82) Wark, A. W.; Lee, H. J.; Corn, R. M. Advanced Methods for SPR Imaging Biosensing. In *Handbook of Surface Plasmon Resonance*; Royal Society of Chemistry, 2008; pp 246–274.
- (83) Smith, E.; Dent, G. *Modern Raman Spectroscopy: A Practical Approach*; John Wiley & Sons, 2013.
- (84) Wang, G.; Park, H.-Y.; Lipert, R. J.; Porter, M. D. Mixed Monolayers on Gold Nanoparticle Labels for Multiplexed Surface-Enhanced Raman Scattering Based Immunoassays. *Anal. Chem.* **2009**, *81* (23), 9643–9650.
- (85) Ingram, A.; Stokes, R. J.; Redden, J.; Gibson, K.; Moore, B.; Faulds, K.; Graham, D. 8-Hydroxyquinolinyl Azo Dyes: A Class of Surface-Enhanced Resonance Raman Scattering-Based Probes for Ultrasensitive Monitoring of Enzymatic Activity. *Anal. Chem.* **2007**, *79* (22), 8578–8583.



- (86) Kahraman, M.; Wachsmann-Hogiu, S. Label-Free and Direct Protein Detection on 3D Plasmonic Nanovoid Structures Using Surface-Enhanced Raman Scattering. *Anal. Chim. Acta* **2015**, *856*, 74–81.
- (87) Li, B.; Ju, H. Label-Free Optical Biosensors Based on a Planar Optical Waveguide. *BioChip J.* **2013**, *7* (4), 295–318.
- (88) Arlett, J.; Myers, E.; Roukes, M. Comparative Advantages of Mechanical Biosensors. *Nat. Nanotechnol.* **2011**, *6* (4), 203.
- (89) McNaught, A. D.; McNaught, A. D. *Compendium of Chemical Terminology*; Blackwell Science Oxford, 1997; Vol. 1669.
- (90) Ahmed, A.; Rushworth, J. V.; Hirst, N. A.; Millner, P. A. Biosensors for Whole-Cell Bacterial Detection. *Clin. Microbiol. Rev.* **2014**, *27* (3), 631–646.
- (91) Sader, J. E.; Larson, I.; Mulvaney, P.; White, L. R. Method for the Calibration of Atomic Force Microscope Cantilevers. *Rev. Sci. Instrum.* **1995**, *66* (7), 3789–3798.
- (92) Lam, D. C.; Yang, F.; Chong, A.; Wang, J.; Tong, P. Experiments and Theory in Strain Gradient Elasticity. *J. Mech. Phys. Solids* **2003**, *51* (8), 1477–1508.
- (93) Chen, G.; Thundat, T.; Wachter, E.; Warmack, R. Adsorption-induced Surface Stress and Its Effects on Resonance Frequency of Microcantilevers. *J. Appl. Phys.* **1995**, *77* (8), 3618–3622.
- (94) Johnson, B. N.; Mutharasan, R. Biosensing Using Dynamic-Mode Cantilever Sensors: A Review. *Biosens. Bioelectron.* **2012**, *32* (1), 1–18.
- (95) Rodahl, M.; Höök, F.; Krozer, A.; Brzezinski, P.; Kasemo, B. Quartz Crystal Microbalance Setup for Frequency and Q-factor Measurements in Gaseous and Liquid Environments. *Rev. Sci. Instrum.* **1995**, *66* (7), 3924–3930.
- (96) Grieshaber, D.; MacKenzie, R.; Vörös, J.; Reimhult, E. Electrochemical Biosensors - Sensor Principles and Architectures. *Sensors* **2008**, *8* (3).
- (97) Bard, A. J.; Faulkner, L. R.; Leddy, J.; Zoski, C. G. *Electrochemical Methods: Fundamentals and Applications*; Wiley New York, 1980; Vol. 2.
- (98) Bishop, D. K.; La Belle, J. T.; Vossler, S. R.; Patel, D. R.; Cook, C. B. A Disposable Tear Glucose Biosensor—part 1: Design and Concept Testing. *J. Diabetes Sci. Technol.* **2010**, *4* (2), 299–306.
- (99) La Belle, J. T.; Bishop, D. K.; Vossler, S. R.; Patel, D. R.; Cook, C. B. A Disposable Tear Glucose Biosensor—part 2: System Integration and Model Validation. *J. Diabetes Sci. Technol.* **2010**, *4* (2), 307–311.
- (100) Lan, K.; McAferty, K.; Shah, P.; Lieberman, E.; Patel, D. R.; Cook, C. B.; La Belle, J. T. A Disposable Tear Glucose Biosensor—part 3: Assessment of Enzymatic Specificity. *J. Diabetes Sci. Technol.* **2011**, *5* (5), 1108–1115.
- (101) La Belle, J. T.; Engelschall, E.; Lan, K.; Shah, P.; Saez, N.; Maxwell, S.; Adamson, T.; Abou-Eid, M.; McAferty, K.; Patel, D. R. A Disposable Tear Glucose Biosensor—Part 4

- Preliminary Animal Model Study Assessing Efficacy, Safety, and Feasibility. *J. Diabetes Sci. Technol.* **2014**, *8* (1), 109–116.
- (102) Altintas, Z.; Fakanya, W. M.; Tothill, I. E. Cardiovascular Disease Detection Using Bio-Sensing Techniques. *Talanta* **2014**, *128*, 177–186.
- (103) Adams, R. N.; Marsden, C. A. Electrochemical Detection Methods for Monoamine Measurements in Vitro and in Vivo. In *Handbook of psychopharmacology*; Springer, 1982; pp 1–74.
- (104) Schenk, J. O.; Miller, E.; Rice, M. E.; Adams, R. N. Chronoamperometry in Brain Slices: Quantitative Evaluations of in Vivo Electrochemistry. *Brain Res.* **1983**, *277* (1), 1–8.
- (105) Chaubey, A.; Malhotra, B. D. Mediated Biosensors. *Biosens. Bioelectron.* **2002**, *17* (6), 441–456.
- (106) Bratov, A.; Abramova, N.; Ipatov, A. Recent Trends in Potentiometric Sensor Arrays—A Review. *Anal. Chim. Acta* **2010**, *678* (2), 149–159.
- (107) Bakker, E.; Pretsch, E. Potentiometric Sensors for Trace-Level Analysis. *Trace-Met. Anal.* **2005**, *24* (3), 199–207.
- (108) Reid, I. R.; Birstow, S. M.; Bolland, M. J. Calcium and Cardiovascular Disease. *Endocrinol. Metab.* **2017**, *32* (3), 339–349.
- (109) Yan, R.; Qiu, S.; Tong, L.; Qian, Y. Review of Progresses on Clinical Applications of Ion Selective Electrodes for Electrolytic Ion Tests: From Conventional ISEs to Graphene-Based ISEs. *Chem. Speciat. Bioavailab.* **2016**, *28* (1–4), 72–77.
- (110) Zong, X.; Wu, C.; Wu, X.; Lu, Y.; Wang, P. A Non-Labeled DNA Biosensor Based on Light Addressable Potentiometric Sensor Modified with TiO<sub>2</sub> Thin Film. *J. Zhejiang Univ. Sci. B* **2009**, *10* (11), 860–866.
- (111) Wu, J.; Chumbimuni-Torres, K. Y.; Galik, M.; Thammakhet, C.; Haake, D. A.; Wang, J. Potentiometric Detection of DNA Hybridization Using Enzyme-Induced Metallization and a Silver Ion Selective Electrode. *Anal. Chem.* **2009**, *81* (24), 10007–10012.
- (112) Sarkar, D.; Liu, W.; Xie, X.; Anselmo, A. C.; Mitragotri, S.; Banerjee, K. MoS<sub>2</sub> Field-Effect Transistor for next-Generation Label-Free Biosensors. *ACS Nano* **2014**, *8* (4), 3992–4003.
- (113) Schöning, M. J.; Poghosian, A. Recent Advances in Biologically Sensitive Field-Effect Transistors (BioFETs). *Analyst* **2002**, *127* (9), 1137–1151.
- (114) Cheng, Y.; Chen, K.-S.; Meyer, N. L.; Yuan, J.; Hirst, L. S.; Chase, P. B.; Xiong, P. Functionalized SnO<sub>2</sub> Nanobelt Field-Effect Transistor Sensors for Label-Free Detection of Cardiac Troponin. *Biosens. Bioelectron.* **2011**, *26* (11), 4538–4544.
- (115) Ibupoto, Z. H.; Jamal, N.; Khun, K.; Willander, M. Development of a Disposable Potentiometric Antibody Immobilized ZnO Nanotubes Based Sensor for the Detection of C-Reactive Protein. *Sens. Actuators B Chem.* **2012**, *166–167*, 809–814.
- (116) Lippa, P. B.; Sokoll, L. J.; Chan, D. W. Immunosensors—principles and Applications to Clinical Chemistry. *Clin. Chim. Acta* **2001**, *314* (1), 1–26.

- (117) Schöning, M. J.; Poghossian, A. Bio FEDs (Field-Effect Devices): State-of-the-Art and New Directions. *Electroanalysis* **2006**, *18* (19-20), 1893–1900.
- (118) Luo, X.; Davis, J. J. Electrical Biosensors and the Label Free Detection of Protein Disease Biomarkers. *Chem. Soc. Rev.* **2013**, *42* (13), 5944–5962.
- (119) Elnathan, R.; Kwiat, M.; Pevzner, A.; Engel, Y.; Burstein, L.; Khatchourints, A.; Lichtenstein, A.; Kantaev, R.; Patolsky, F. Biorecognition Layer Engineering: Overcoming Screening Limitations of Nanowire-Based FET Devices. *Nano Lett.* **2012**, *12* (10), 5245–5254.
- (120) Prodromidis, M. I. Impedimetric Immunosensors—A Review. *Sens. Sens. Technol.* **2010**, *55* (14), 4227–4233.
- (121) Bahadır, E. B.; Sezgintürk, M. K. A Review on Impedimetric Biosensors. *Artif. Cells Nanomedicine Biotechnol.* **2016**, *44* (1), 248–262.
- (122) Xu, M.; Luo, X.; Davis, J. J. The Label Free Picomolar Detection of Insulin in Blood Serum. *Biosens. Bioelectron.* **2013**, *39* (1), 21–25.
- (123) Lin, Z.; Chen, L.; Zhang, G.; Liu, Q.; Qiu, B.; Cai, Z.; Chen, G. Label-Free Aptamer-Based Electrochemical Impedance Biosensor for 17 $\beta$ -Estradiol. *Analyst* **2012**, *137* (4), 819–822.
- (124) Hu, Y.; Zuo, P.; Ye, B.-C. Label-Free Electrochemical Impedance Spectroscopy Biosensor for Direct Detection of Cancer Cells Based on the Interaction between Carbohydrate and Lectin. *Biosens. Bioelectron.* **2013**, *43*, 79–83.
- (125) Cardinell, B. Towards a Hand-Held Multi-Biomarker Point-of-Care Diagnostic to Quantify Traumatic Brain Injury. **2017**.
- (126) Malkoc, A.; Sanchez, E.; Caplan, M. R.; La Belle, J. T. Electrochemical-Nucleic Acid Detection with Enhanced Specificity and Sensitivity. *J. Biosens. Bioelectron.* **2015**, *6* (2), 1.
- (127) Shalini Prasad; Anjan Panneer Selvam; Ravikiran K. Reddy; Adrian Love. Silicon Nanosensor for Diagnosis of Cardiovascular Proteomic Markers. *J. Lab. Autom.* **2012**, *18* (2), 143–151.
- (128) Lin, K.-C.; Kunduru, V.; Bothara, M.; Rege, K.; Prasad, S.; Ramakrishna, B. L. Biogenic Nanoporous Silica-Based Sensor for Enhanced Electrochemical Detection of Cardiovascular Biomarkers Proteins. *Biosens. Bioelectron.* **2010**, *25* (10), 2336–2342.
- (129) Cardinell, B. A.; La Belle, J. T. Enzymatic Detection of Traumatic Brain Injury Related Biomarkers. *Biosens. Biodetection Methods Protoc. Vol. 2 Electrochem. Bioelectron. Piezoelectric Cell. Mol. Biosens.* **2017**, 89–112.
- (130) Boonyasit, Y.; Chailapakul, O.; Laiwattanapaisal, W. A Multiplexed Three-Dimensional Paper-Based Electrochemical Impedance Device for Simultaneous Label-Free Affinity Sensing of Total and Glycated Haemoglobin: The Potential of Using a Specific Single-Frequency Value for Analysis. *Anal. Chim. Acta* **2016**, *936*, 1–11.
- (131) Esfandyarpour, R.; Yang, L.; Koochak, Z.; Harris, J. S.; Davis, R. W. Nanoelectronic Three-Dimensional (3D) Nanotip Sensing Array for Real-Time, Sensitive, Label-Free Sequence Specific Detection of Nucleic Acids. *Biomed. Microdevices* **2016**, *18* (1), 7.

- (132) Rinaldi, A. L.; Carballo, R. Impedimetric Non-Enzymatic Glucose Sensor Based on Nickel Hydroxide Thin Film onto Gold Electrode. *Sens. Actuators B Chem.* **2016**, *228*, 43–52.
- (133) Hui, G.-H.; Ji, P.; Mi, S.-S.; Deng, S.-P. Electrochemical Impedance Spectrum Frequency Optimization of Bitter Taste Cell-Based Sensors. *Biosens. Bioelectron.* **2013**, *47*, 164–170.
- (134) Yuan, X.-Z.; Song, C.; Wang, H.; Zhang, J. *EIS Equivalent Circuits*; Springer, 2010.
- (135) He, Z.; Mansfeld, F. Exploring the Use of Electrochemical Impedance Spectroscopy (EIS) in Microbial Fuel Cell Studies. *Energy Environ. Sci.* **2009**, *2* (2), 215–219.
- (136) Macdonald, D. D. Reflections on the History of Electrochemical Impedance Spectroscopy. *Electrochem. Impedance Spectrosc.* **2006**, *51* (8), 1376–1388.
- (137) Biela, A.; Watkinson, M.; Meier, U. C.; Baker, D.; Giovannoni, G.; Becer, C. R.; Krause, S. Disposable MMP-9 Sensor Based on the Degradation of Peptide Cross-Linked Hydrogel Films Using Electrochemical Impedance Spectroscopy. *Biosens. Bioelectron.* **2015**, *68*, 660–667.
- (138) La Belle, J. T.; Gerlach, J. Q.; Svarovsky, S.; Joshi, L. Label-Free Impedimetric Detection of Glycan–Lectin Interactions. *Anal. Chem.* **2007**, *79* (18), 6959–6964.
- (139) Zhang, D.; Jiang, J.; Chen, J.; Zhang, Q.; Lu, Y.; Yao, Y.; Li, S.; Liu, G. L.; Liu, Q. Smartphone-Based Portable Biosensing System Using Impedance Measurement with Printed Electrodes for 2, 4, 6-Trinitrotoluene (TNT) Detection. *Biosens. Bioelectron.* **2015**, *70*, 81–88.
- (140) Kiilerich-Pedersen, K.; Daprà, J.; Cherré, S.; Rozlosnik, N. High Sensitivity Point-of-Care Device for Direct Virus Diagnostics. *Biosens. Bioelectron.* **2013**, *49*, 374–379.
- (141) Canbaz, M. Ç.; Şimşek, Ç. S.; Sezgintürk, M. K. Electrochemical Biosensor Based on Self-Assembled Monolayers Modified with Gold Nanoparticles for Detection of HER-3. *Anal. Chim. Acta* **2014**, *814*, 31–38.
- (142) Özcan, B.; Demirbakan, B.; Yeşiller, G.; Sezgintürk, M. K. Introducing a New Method for Evaluation of the Interaction between an Antigen and an Antibody: Single Frequency Impedance Analysis for Biosensing Systems. *Talanta* **2014**, *125*, 7–13.
- (143) Luo, X.; Xu, M.; Freeman, C.; James, T.; Davis, J. J. Ultrasensitive Label Free Electrical Detection of Insulin in Neat Blood Serum. *Anal. Chem.* **2013**, *85* (8), 4129–4134.
- (144) Adamson, T. L.; Eusebio, F. A.; Cook, C. B.; LaBelle, J. T. The Promise of Electrochemical Impedance Spectroscopy as Novel Technology for the Management of Patients with Diabetes Mellitus. *Analyst* **2012**, *137* (18), 4179–4187.
- (145) Haselwood, B. A.; La Belle, J. T. Development of Electrochemical Methods to Enzymatically Detect Traumatic Brain Injury Biomarkers. *Biosens. Bioelectron.* **2015**, *67*, 752–756.
- (146) Patil, A. V.; Bedatty Fernandes, F. C.; Bueno, P. R.; Davis, J. J. Immittance Electroanalysis in Diagnostics. *Anal. Chem.* **2014**, *87* (2), 944–950.

- (147) Rowe, A. A.; Miller, E. A.; Plaxco, K. W. Reagentless Measurement of Aminoglycoside Antibiotics in Blood Serum via an Electrochemical, Ribonucleic Acid Aptamer-Based Biosensor. *Anal. Chem.* **2010**, *82* (17), 7090–7095.
- (148) La Belle, J. T.; Fairchild, A.; Demirok, U. K.; Verma, A. Method for Fabrication and Verification of Conjugated Nanoparticle-Antibody Tuning Elements for Multiplexed Electrochemical Biosensors. *Methods* **2013**, *61* (1), 39–51.
- (149) Expert Panel on Detection, E. Executive Summary of the Third Report of the National Cholesterol Education Program (NCEP) Expert Panel on Detection, Evaluation, and Treatment of High Blood Cholesterol in Adults (Adult Treatment Panel III). *Jama* **2001**, *285* (19), 2486.
- (150) Lu, Y.; Li, H.; Zhuang, S.; Zhang, D.; Zhang, Q.; Zhou, J.; Dong, S.; Liu, Q.; Wang, P. Olfactory Biosensor Using Odorant-Binding Proteins from Honeybee: Ligands of Floral Odors and Pheromones Detection by Electrochemical Impedance. *Sens. Actuators B Chem.* **2014**, *193*, 420–427.
- (151) Lu, Y.; Zhang, D.; Zhang, Q.; Huang, Y.; Luo, S.; Yao, Y.; Li, S.; Liu, Q. Impedance Spectroscopy Analysis of Human Odorant Binding Proteins Immobilized on Nanopore Arrays for Biochemical Detection. *Biosens. Bioelectron.* **2016**, *79*, 251–257.
- (152) Kochowski, S.; Nitsch, K. Description of the Frequency Behaviour of Metal–SiO<sub>2</sub>–GaAs Structure Characteristics by Electrical Equivalent Circuit with Constant Phase Element. *Thin Solid Films* **2002**, *415* (1–2), 133–137.
- (153) Campos, H.; Blijlevens, E.; McNamara, J.; Ordovas, J.; Posner, B.; Wilson, P.; Castelli, W.; Schaefer, E. LDL Particle Size Distribution. Results from the Framingham Offspring Study. *Arterioscler. Thromb. Vasc. Biol.* **1992**, *12* (12), 1410–1419.
- (154) Jeyarajah, E. J.; Cromwell, W. C.; Otvos, J. D. Lipoprotein Particle Analysis by Nuclear Magnetic Resonance Spectroscopy. *Clin. Lab. Med.* **2006**, *26* (4), 847–870.
- (155) Gamero, M.; Pariente, F.; Lorenzo, E.; Alonso, C. Nanostructured Rough Gold Electrodes for the Development of Lactate Oxidase-Based Biosensors. *Biosens. Bioelectron.* **2010**, *25* (9), 2038–2044.
- (156) Arbeláez, A. M.; Cryer, P. E. Lactate and the Mechanism of Hypoglycemia-Associated Autonomic Failure in Diabetes. *Diabetes* **2013**, *62* (12), 3999–4001.
- (157) American Diabetes Association. Diagnosis and Classification of Diabetes Mellitus. *Diabetes Care* **2006**, *29* (1), S43.
- (158) Lipska, K. J.; Ross, J. S.; Wang, Y.; Inzucchi, S. E.; Minges, K.; Karter, A. J.; Huang, E. S.; Desai, M. M.; Gill, T. M.; Krumholz, H. M. National Trends in US Hospital Admissions for Hyperglycemia and Hypoglycemia among Medicare Beneficiaries, 1999 to 2011. *JAMA Intern. Med.* **2014**, *174* (7), 1116–1124.
- (159) Wang, H.-C.; Zhou, H.; Chen, B.; Mendes, P. M.; Fossey, J. S.; James, T. D.; Long, Y.-T. A Bis-Boronic Acid Modified Electrode for the Sensitive and Selective Determination of Glucose Concentrations. *Analyst* **2013**, *138* (23), 7146–7151.
- (160) Lu, Y.; Li, H.; Zhuang, S.; Zhang, D.; Zhang, Q.; Zhou, J.; Dong, S.; Liu, Q.; Wang, P. Olfactory Biosensor Using Odorant-Binding Proteins from Honeybee: Ligands of Floral

Odors and Pheromones Detection by Electrochemical Impedance. *Sens. Actuators B Chem.* **2014**, *193*, 420–427.

- (161) Barsoukov, E.; Macdonald, J. R. *Impedance Spectroscopy: Theory, Experiment, and Applications*; John Wiley & Sons, 2005.
- (162) Kuznetsov, B.; Shumakovich, G.; Koroleva, O.; Yaropolov, A. On Applicability of Laccase as Label in the Mediated and Mediatorless Electroimmunoassay: Effect of Distance on the Direct Electron Transfer between Laccase and Electrode. *Biosens. Bioelectron.* **2001**, *16* (1), 73–84.
- (163) Adamson, T. L.; Cook, C. B.; LaBelle, J. T. Detection of 1,5-Anhydroglucitol by Electrochemical Impedance Spectroscopy. *J. Diabetes Sci. Technol.* **2014**, *8* (2), 350–355.
- (164) Freckmann, G.; Schmid, C.; Baumstark, A.; Pleus, S.; Link, M.; Haug, C. System Accuracy Evaluation of 43 Blood Glucose Monitoring Systems for Self-Monitoring of Blood Glucose According to DIN EN ISO 15197. *J. Diabetes Sci. Technol.* **2012**, *6* (5), 1060–1075.
- (165) Hajisalem, G.; Min, Q.; Gelfand, R.; Gordon, R. Effect of Surface Roughness on Self-Assembled Monolayer Plasmonic Ruler in Nonlocal Regime. *Opt. Express* **2014**, *22* (8), 9604–9610.
- (166) La Belle, J. T.; Fairchild, A.; Demirok, U. K.; Verma, A. Method for Fabrication and Verification of Conjugated Nanoparticle-Antibody Tuning Elements for Multiplexed Electrochemical Biosensors. *Methods* **2013**, *61* (1), 39–51.
- (167) Lu, Y.; Zhang, D.; Zhang, Q.; Huang, Y.; Luo, S.; Yao, Y.; Li, S.; Liu, Q. Impedance Spectroscopy Analysis of Human Odorant Binding Proteins Immobilized on Nanopore Arrays for Biochemical Detection. *Biosens. Bioelectron.* **2016**, *79*, 251–257.
- (168) Boubour, E.; Lennox, R. B. Insulating Properties of Self-Assembled Monolayers Monitored by Impedance Spectroscopy. *Langmuir* **2000**, *16* (9), 4222–4228.
- (169) Lin, C.; Ryder, L.; Probst, D.; Caplan, M.; Spano, M.; LaBelle, J. Feasibility in the Development of a Multi-Marker Detection Platform. *Biosens. Bioelectron.* **2017**, *89*, 743–749.
- (170) La Belle, J. T.; Demirok, U. K.; Patel, D. R.; Cook, C. B. Development of a Novel Single Sensor Multiplexed Marker Assay. *Analyst* **2011**, *136* (7), 1496–1501.
- (171) Esfandyarpour, R.; Yang, L.; Harris, J. S.; Davis, R. W. Nanoelectronic Three-Dimensional (3D) Nanotip Sensing Array for Real-Time, Sensitive, Label-Free Sequence Specific Detection of Nucleic Acids. *Biomed. Microdevices* **2016**, *18* (1), 7.
- (172) Boonyasit, Y.; Chailapakul, O.; Laiwattanapaisal, W. A Multiplexed Three-Dimensional Paper-Based Electrochemical Impedance Device for Simultaneous Label-Free Affinity Sensing of Total and Glycated Haemoglobin: The Potential of Using a Specific Single-Frequency Value for Analysis. *Anal. Chim. Acta* **2016**, *936*, 1–11.
- (173) Hernandez, K.; Fernandez-Lafuente, R. Control of Protein Immobilization: Coupling Immobilization and Site-Directed Mutagenesis to Improve Biocatalyst or Biosensor Performance. *Enzyme Microb. Technol.* **2011**, *48* (2), 107–122.

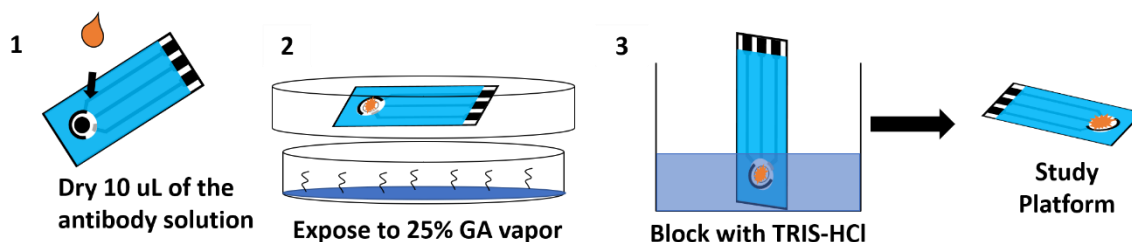
- (174) Makaraviciute, A.; Ramanaviciene, A. Site-Directed Antibody Immobilization Techniques for Immunosensors. *Biosens. Bioelectron.* **2013**, *50*, 460–471.
- (175) Orazem, M. E.; Tribollet, B. *Electrochemical Impedance Spectroscopy*; John Wiley & Sons, 2011; Vol. 48.
- (176) German, N.; Kausaite-Minkstiniene, A.; Ramanavicius, A.; Semashko, T.; Mikhailova, R.; Ramanaviciene, A. The Use of Different Glucose Oxidases for the Development of an Amperometric Reagentless Glucose Biosensor Based on Gold Nanoparticles Covered by Polypyrrole. *Electrochimica Acta* **2015**, *169*, 326–333.
- (177) Minter, S. D. *Microfluidic Techniques: Reviews and Protocols*; Springer Science & Business Media, 2006; Vol. 321.
- (178) Savini, G.; Prabhawasad, P.; Kojima, T.; Grueterich, M.; Espana, E.; Goto, E. The Challenge of Dry Eye Diagnosis. *Clin. Ophthalmol. Auckl. NZ* **2008**, *2* (1), 31–55.
- (179) Marques, M. R.; Loebenberg, R.; Almukainzi, M. Simulated Biological Fluids with Possible Application in Dissolution Testing. *Dissolution Technol* **2011**, *18* (3), 15–28.
- (180) Food and Drug Administration. Guidance for Industry on Bioanalytical Method Validation. *Fed. Regist.* **2001**, *66* (100), 28526.
- (181) Yamada, K.; Henares, T. G.; Suzuki, K.; Citterio, D. Distance-Based Tear Lactoferrin Assay on Microfluidic Paper Device Using Interfacial Interactions on Surface-Modified Cellulose. *ACS Appl. Mater. Interfaces* **2015**, *7* (44), 24864–24875.
- (182) Xiao, Y.; Isaacs, S. N. Enzyme-Linked Immunosorbent Assay (ELISA) and Blocking with Bovine Serum Albumin (BSA)—not All BSAs Are Alike. *J. Immunol. Methods* **2012**, *384* (1), 148–151.
- (183) Mattos, A.; Freitas, T.; Silva, V.; Dutra, R. A Dual Quartz Crystal Microbalance for Human Cardiac Troponin T in Real Time Detection. *Sens. Actuators B Chem.* **2012**, *161* (1), 439–446.
- (184) Fomo, G.; Waryo, T. T.; Sunday, C. E.; Baleg, A. A.; Baker, P. G.; Iwuoha, E. I. Aptameric Recognition-Modulated Electroactivity of Poly (4-Styrenesulfonic Acid)-Doped Polyaniline Films for Single-Shot Detection of Tetrodotoxin. *Sensors* **2015**, *15* (9), 22547–22560.
- (185) Olson, W. C.; Spitznagel, T. M.; Yarmush, M. L. Dissociation Kinetics of Antigen-Antibody Interactions: Studies on a Panel of Anti-Albumin Monoclonal Antibodies. *Mol. Immunol.* **1989**, *26* (2), 129–136.
- (186) van Berkel, P. H.; van Veen, H. A.; Geerts, M. E.; Nuijens, J. H. Characterization of Monoclonal Antibodies against Human Lactoferrin. *J. Immunol. Methods* **2002**, *267* (2), 139–150.
- (187) Pandolfi, M.; Astrup, T. A Histochemical Study of the Fibrinolytic Activity: Cornea, Conjunctiva, and Lacrimal Gland. *Arch. Ophthalmol.* **1967**, *77* (2), 258–264.
- (188) Posa, A.; Bräuer, L.; Schicht, M.; Garreis, F.; Beileke, S.; Paulsen, F. Schirmer Strip vs. Capillary Tube Method: Non-Invasive Methods of Obtaining Proteins from Tear Fluid. *Ann. Anat.-Anat. Anz.* **2013**, *195* (2), 137–142.

- (189) Van Setten, G.-B.; Stephens, R.; Tervo, T.; Salonen, E.-M.; Tarkkanen, A.; Vaheri, A. Effects of the Schirmer Test on the Fibrinolytic System in the Tear Fluid. *Exp. Eye Res.* **1990**, *50* (2), 135–141.
- (190) Dumortier, G.; Chaumeil, J. Lachrymal Determinations: Methods and Updates on Biopharmaceutical and Clinical Applications. *Ophthalmic Res.* **2004**, *36* (4), 183–194.
- (191) Small, D.; Hevy, J.; Tang-Liu, D. Comparison of Tear Sampling Techniques for Pharmacokinetic Analysis: Ofloxacin Concentrations in Rabbit Tears after Sampling with Schirmer Tear Strips, Capillary Tubes, or Surgical Sponges. *J. Ocul. Pharmacol. Ther.* **2000**, *16* (5), 439–446.
- (192) Hagan, S.; Martin, E.; Enríquez-de-Salamanca, A. Tear Fluid Biomarkers in Ocular and Systemic Disease: Potential Use for Predictive, Preventive and Personalised Medicine. *EPMA J.* **2016**, *7*.
- (193) Fairchild, A. B.; McAferty, K.; Demirok, U. K.; La Belle, J. T. A Label-Free, Rapid Multimarker Protein Impedance-Based Immunosensor. *IEEE* **2009**, 1–5.
- (194) Bhavsar, K.; Fairchild, A.; Alonas, E.; Bishop, D. K.; La Belle, J. T.; Sweeney, J.; Alford, T.; Joshi, L. A Cytokine Immunosensor for Multiple Sclerosis Detection Based upon Label-Free Electrochemical Impedance Spectroscopy Using Electroplated Printed Circuit Board Electrodes. *Biosens. Bioelectron.* **2009**, *25* (2), 506–509.
- (195) Demirok, U. K.; Verma, A.; La Belle, J. T. The Development of a Label-Free Electrochemical Impedance Based Point-of-Care Technology for Multimarker Detection. *J. Biosens. Bioelectron.* **2013**, *2013*.
- (196) Hunter, R. J. *Zeta Potential in Colloid Science: Principles and Applications*; Academic press, 2013; Vol. 2.
- (197) American Diabetes Association. Diagnosis and Classification of Diabetes Mellitus. *Diabetes Care* **2004**, *27* (suppl 1), s5–s10.
- (198) Arican, O.; Aral, M.; Sasmaz, S.; Ciragil, P. Serum Levels of TNF- $\alpha$ , IFN- $\gamma$ , IL-6, IL-8, IL-12, IL-17, and IL-18 in Patients with Active Psoriasis and Correlation with Disease Severity. *Mediators Inflamm.* **2005**, *2005* (5), 273–279.
- (199) Kaszuba, M.; Corbett, J.; Watson, F. M.; Jones, A. High-Concentration Zeta Potential Measurements Using Light-Scattering Techniques. *Philos. Trans. R. Soc. Lond. Math. Phys. Eng. Sci.* **2010**, *368* (1927), 4439–4451.
- (200) Tantra, R.; Schulze, P.; Quincey, P. Effect of Nanoparticle Concentration on Zeta-Potential Measurement Results and Reproducibility. *Particuology* **2010**, *8* (3), 279–285.
- (201) Lefebure, S.; Dubois, E.; Cabuil, V.; Neveu, S.; Massart, R. Monodisperse Magnetic Nanoparticles: Preparation and Dispersion in Water and Oils. *J. Mater. Res.* **1998**, *13* (10), 2975–2981.
- (202) Livingston, J.; Bean, C. Specific Heat of Superparamagnetic Particles. *J. Appl. Phys.* **1961**, *32* (10), 1964–1966.



- (203) Reddy, K. R.; Lee, K.; Iyengar, A. G. Synthesis and Characterization of Novel Conducting Composites of Fe<sub>3</sub>O<sub>4</sub> Nanoparticles and Sulfonated Polyanilines. *J. Appl. Polym. Sci.* **2007**, *104* (6), 4127–4134.
- (204) Greenwood, N. N.; Earnshaw, A. *Chemistry of the Elements*; Elsevier, 2012.
- (205) Perez, J. M.; Josephson, L.; O'Loughlin, T.; Högemann, D.; Weissleder, R. Magnetic Relaxation Switches Capable of Sensing Molecular Interactions. *Nat. Biotechnol.* **2002**, *20* (8), 816–820.
- (206) Lu, G. W.; Gao, P. Emulsions and Microemulsions for Topical and Transdermal Drug Delivery. In *Handbook of Non-Invasive Drug Delivery Systems*; Elsevier, 2010; pp 59–94.
- (207) Solanki, P. R.; Kaushik, A.; Agrawal, V. V.; Malhotra, B. D. Nanostructured Metal Oxide-Based Biosensors. *NPG Asia Mater.* **2011**, *3* (1), 17–24.
- (208) Chaki, N. K.; Aslam, M.; Gopakumar, T.; Sharma, J.; Pasricha, R.; Mulla, I.; Vijayamohanan, K. Effect of Chain Length and the Nature of the Monolayer on the Electrical Behavior of Hydrophobically Organized Gold Clusters. *J. Phys. Chem. B* **2003**, *107* (49), 13567–13574.
- (209) Kasaliwal, G. R.; Göldel, A.; Pötschke, P.; Heinrich, G. Influences of Polymer Matrix Melt Viscosity and Molecular Weight on MWCNT Agglomerate Dispersion. *Polymer* **2011**, *52* (4), 1027–1036.
- (210) Koops, C. On the Dispersion of Resistivity and Dielectric Constant of Some Semiconductors at Audiofrequencies. *Phys. Rev.* **1951**, *83* (1), 121.
- (211) Cole, K. S.; Cole, R. H. Dispersion and Absorption in Dielectrics I. Alternating Current Characteristics. *J. Chem. Phys.* **1941**, *9* (4), 341–351.
- (212) Brust, M.; Bethell, D.; Kiely, C. J.; Schiffrin, D. J. Self-Assembled Gold Nanoparticle Thin Films with Nonmetallic Optical and Electronic Properties. *Langmuir* **1998**, *14* (19), 5425–5429.
- (213) Coster, H. G.; Chilcott, T. C.; Coster, A. C. Impedance Spectroscopy of Interfaces, Membranes and Ultrastructures. *Bioelectrochem. Bioenerg.* **1996**, *40* (2), 79–98.

APPENDIX A  
PHYSICAL ADSORPTION BASED FABRICATION OF BIOSENSORS WITH  
GLUTARALDEHYDE CROSSLINKING



The protocol was originally built to investigate the native optimal frequency of a biomarker. It was built on a commercially available disposable SPCE, Zensor (CH Instruments, TX), containing graphite working and counter electrodes and a silver/silver chloride reference electrode. The protocol will work on all graphite-based sensors. A schematic of the sensor preparation protocol is illustrated above. First, a desired amount of the respective antibody (1  $\mu\text{g}$  total is a good start) in PBS was deposited onto the working electrode and dried in an oven at 24 °C for 25 minutes. Once dry, the sensors were exposed to glutaraldehyde fumes generated from 1 mL of 25% GA in a parafilm-sealed vessel on an orbital shaker for 1 hour at 80 rpm. The sensors were again dried at 24 °C for 25 minutes, allowing the cross-linked antibodies to adsorb onto the graphite working electrode. Blocking of unreacted aldehyde groups from GA-crosslinking was achieved by submerging the sensing well in 1 mM Trizma<sup>®</sup> and hydrochloric acid (TRIS-HCl) solution (pH 7.4) for 25 minutes<sup>177</sup>. Sensors were rinsed in PBS followed by deionized water and dried at 24 °C. The sensors were either i. immediately subject to electrochemical testing or, ii. stored at 4 °C for future testing.

#### *Chemicals and Biologicals*

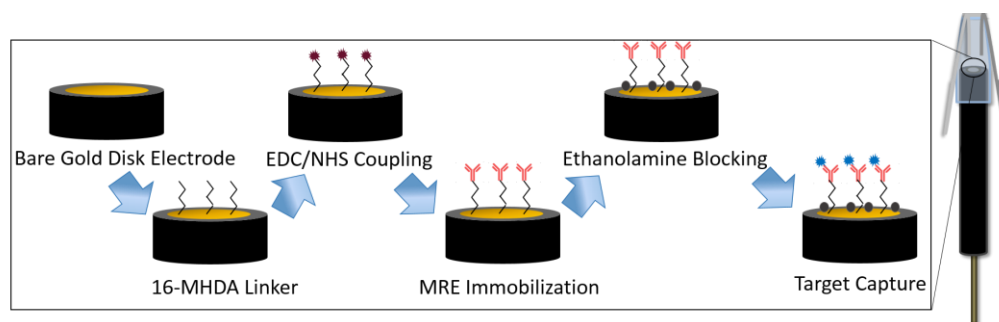
All chemical reagents could be purchased from Sigma-Aldrich, MO. The glutaraldehyde stock came in 25% w/w in DI and is light- and air-sensitive

## APPENDIX B

### COVALENT BINDING BASED SENSOR FABRICATION USING PRIMARY AMINES

The sensors consist of GDEs, silver/silver chloride reference electrodes, and platinum counter electrodes (CH Instrument, USA). The gold surface thickness of a GDE is approximately 2.5 mm. GDEs were polished with 100 figure-eight motions on Buehler felt pads using 3.0, 1.0, and 0.05  $\mu\text{m}$  grit alumina oxide in distilled water (DI) followed by sonication in DI for 15 min. After sonication, the formal potential was obtained by performing cyclic voltammetry from -1.0 V to 1.0 V in a solution of 100 mM potassium ferricyanide prepared in pH 7.4 phosphate buffer saline (PBS). EIS was then performed using the formal potential and a 5 mV AC sine wave sweeping from 1 Hz to 100 kHz to measure the bare impedance of GDEs, which helps determine GDEs' surface topography. After rinsing the GDEs with DI, 1 mM of 16-mercaptohexadecanoic acid (16-MHDA) in ethanol was incubated onto the GDEs for 1 hr to form a self-assembly monolayer (SAM), allowing the thiol group of SAM to bind onto gold. Post-MHDA impedance was measured at the formal potential of each GDE for quality control. The carboxylate groups on the tail end of 16-MHDA were then activated by incubating the sensor with 40 mM 1-ethyl-3-(3-dimethylaminopropyl) carbodiimide (EDC) and 20 mM sulfo-derivative of N-hydroxysuccinimide (NHS) for 1 hr. After washing the sensor with DI, 100  $\mu\text{L}$  of the desired concentration of molecular recognition elements prepared in pH 7.4 PBS could be immobilized onto the sensor at room temperature for 1 hr. The sensors were then washed with PBS following the immobilization and the remaining reactive sites were blocked with 1% ethanolamine for 30 min. After rinsing the sensors with PBS, they were stored at 4°C until further use.

The reagents and solvents, 16-MHDA, EDC, NHS, and potassium ferricyanide were all obtained from Sigma-Aldrich, USA. PBS was purchased from VWR International, USA.



Schematic of sensor fabrication and setup. Reprinted with permission from reference 1

APPENDIX C  
QUALITY CONTROL

#### First Level:

After rinsing the bare electrodes, measure the impedance of each electrode by submerging the electrodes in 100 mM potassium ferricyanide. The submersion of electrode helps eliminate the variance generated from pipetting and thus give a true estimation of the fundamental variance of the sensor. Calculate the %RSD and average impedance in all spectrums ( $Z$ ,  $Z''$ ,  $Z'$ , and phase).

#### Second Level:

After coating the sensor with functional chemicals, measure the impedance of each electrode by either submerging the electrode in 100 mM potassium ferricyanide, or pipetting the 100 mM potassium ferricyanide onto the working electrode. The sensing well should be well-covered to minimize pipetting errors. Calculate the %RSD and average impedance in all spectrums ( $Z$ ,  $Z''$ ,  $Z'$ , and phase). For GDEs, select the sensors that give smallest %RSD. If using  $Z''$  algorithm, in addition to the smallest %RSD, select the sensors that have the same cutoff frequency. Proceed with immobilization of molecular recognition elements with these screened sensors.

#### Third Level:

After the fabrication of sensor completes, measure the impedance of each electrode in a 50:50 mixture containing 100 mM ferricyanide and a blank solution (buffer solution with no target analytes). Measure the impedance and calculate %RSD and average impedance in all impedance spectrums.

Ideally, sensors should not surpass 20% RSD.

APPENDIX D

SAMPLE PREPARTION AND TESTING PROTOCOL



All analyte samples were freshly prepared prior to testing. For affinity binding-based biomarkers, all analyte samples were prepared 15 minutes prior to testing. For enzymatic biomarker, glucose was prepared a day in advance to allow stabilization. Lactate was prepared 15 minutes prior to testing. All diluted samples were stored either in an ice box or a cooler until tested.

To test the analytes, prepare the analytes 2X more concentrated than the intended concentration. Add 50  $\mu\text{L}$  of sample to 50  $\mu\text{L}$  of 200 mM potassium ferricyanide to reach the intended analyte concentration and 100 mM potassium.

For co-immobilized testing, prepare the analytes 4X more concentrated than the intended concentration. Add 25  $\mu\text{L}$  of sample A to 25  $\mu\text{L}$  of sample B and 50  $\mu\text{L}$  of 200 mM potassium ferricyanide to reach the intended analyte concentration and 100 mM potassium.

Special attention is required when diluting the lactoferrin proteins. It is very unstable, and the stock solution contains StabilZyme. After diluting to the desired concentration, use the sample within 5 minutes.

APPENDIX E  
LASER CUTTING PROTOCOL

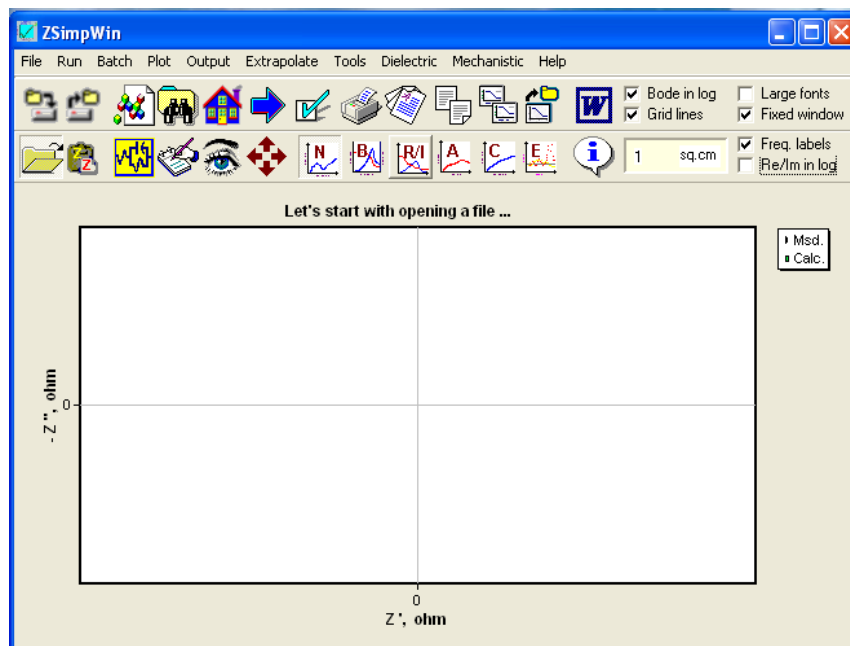
- Laser cutter initiation
  - Turn on the air compressor
  - Turn on the input power button on the laser cutter
  - Adjust air to 50%
  - Use the white stud to adjust the Z axis of laser to 0.075 inch
- Transferring CAD file to laser cutter
  - Open the CAD file using Corel
  - Click "Print" -> PLS 4.75
  - Make sure the printed files use "red hairline" for each job
- Laser cut the filter papers
  - Make sure to use Whatman 41 grade filter paper.
  - Adjust the laser setting to cut as much pieces out of a filter paper stack
    - 70% power, 50% speed, PPI 500
    - 5 filter paper stack per cut area. Populate 6 devices per cut area. Cut 1 cut area at once and harvest. Adjust X&Y coordinates when appropriate
- Laser cut the 3M adhesive tape
  - Place a layer of 3M tape onto a paper board to serve as the sacrificial layer
  - Place a 2<sup>nd</sup> layer of 3M tape onto the 1<sup>st</sup> layer
  - Adjust the laser setting to cut only the top layer through
    - 0.062 thick mat board
    - Red laser, 10% power, 18% speed, PPI 500, air flow 75%
      - Reduce power or increase speed to get a clean cut on 1<sup>st</sup> layer. If you see burn mark it means it's cutting the paper board already.

APPENDIX F  
ELECTROCHEMICAL CIRCUIT MODELING PROTOCOL

Start ZsimpWin using Fairchild's account (make sure the registration key file is inside the installation folder)



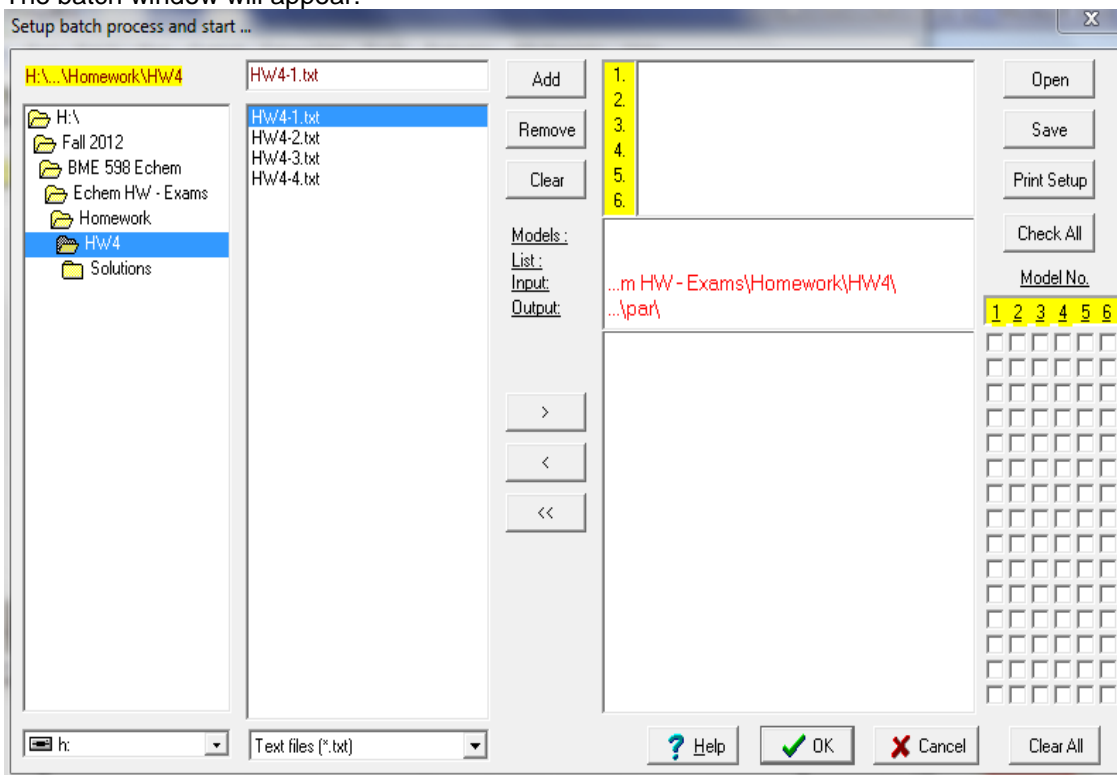
Click ok, you should get



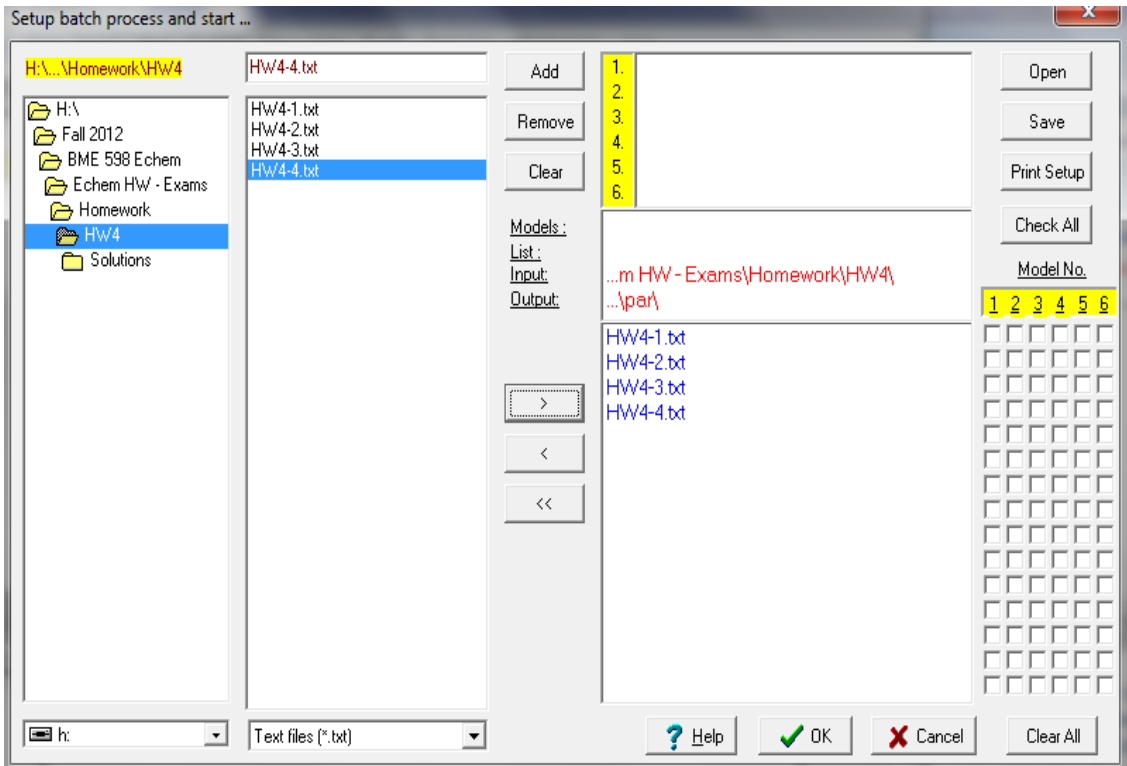
First you might want to compare models, so you will batch process the blank to the concentration gradient high. Click batch (third button on left top-see below for picture of button)



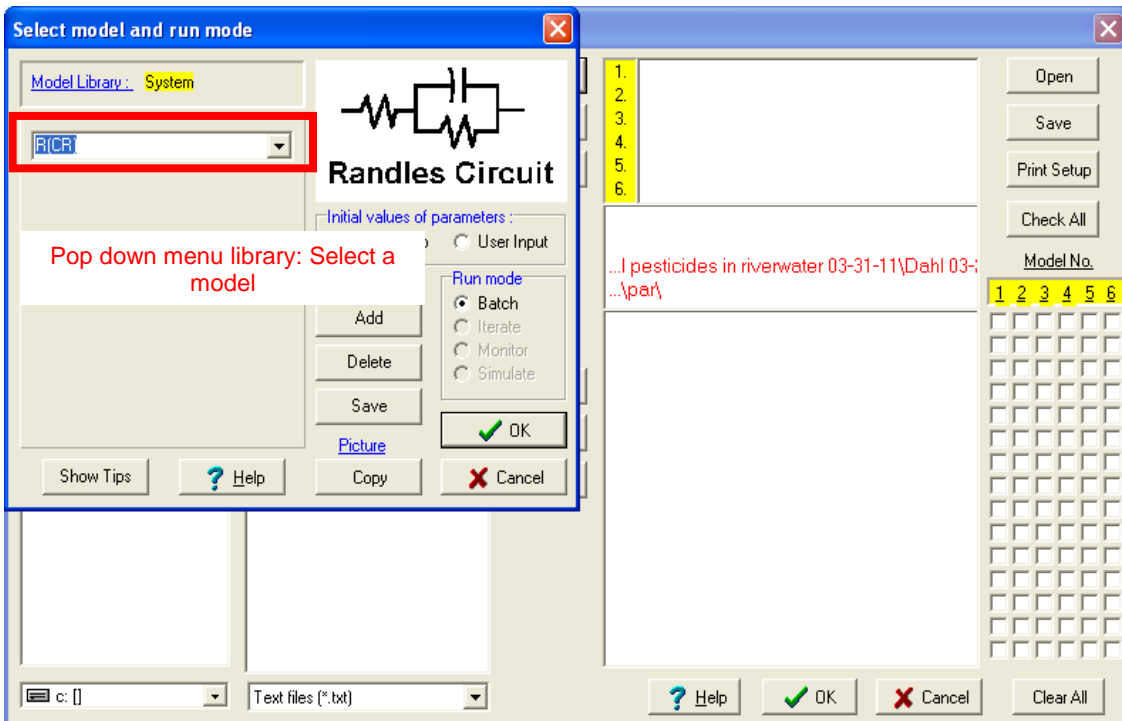
The batch window will appear:



In the left pane, find the files you want to examine (files must be already be saved to your computer, flashdrive, etc.), once you got them in the middle pane where it says “Readme.txt” you can click on them (clicking the file will highlight it), then hit “Enter” on the keyboard or click the “>” button there in the middle to load the files. The files will appear in the right pane when they are added (see below).

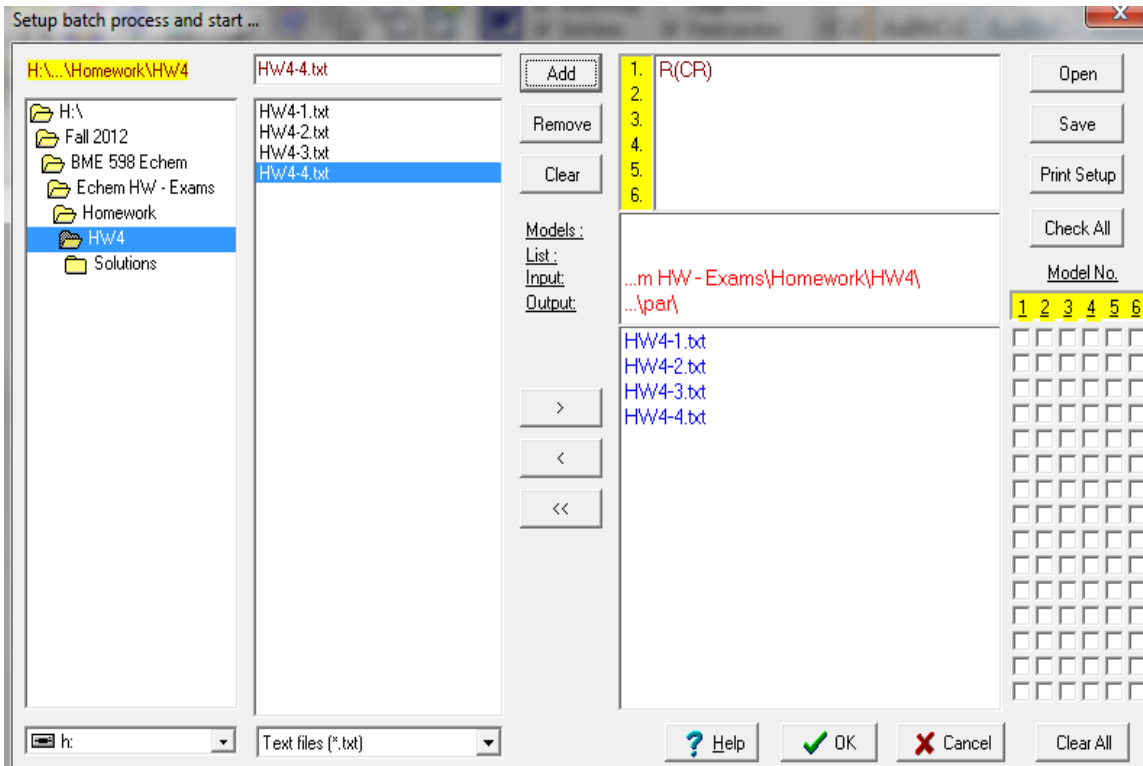


Now you need to “Add” models (upper middle button- highlighted above). You can only add one model at a time, so you will have to click the “Add” button in the upper middle (highlighted above) to add all four models. You are looking for four basic models: the Randles, the Warburg, the Warburg with CPE and A CPE without a Warburg. They have a crazy way of delineating them, if I click on the R(CR) on the pop down menu library (see below):



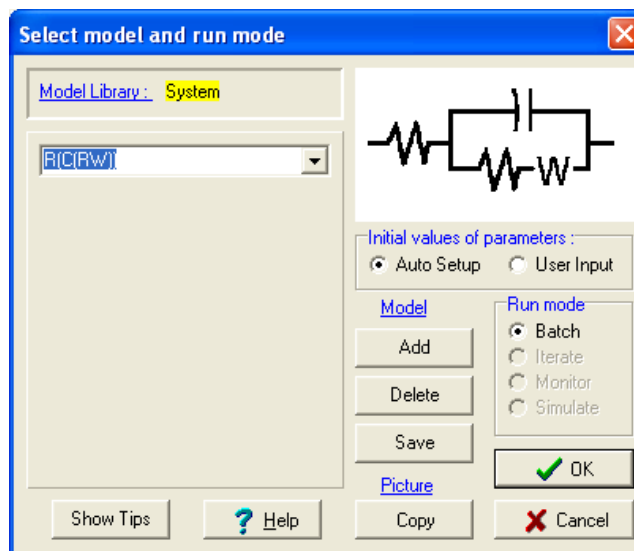
I get the Randles R(CR) model, click "ok". \*ALTERNATIVELY, you can type in R(CR) into the drop down field to select the Randles model. The model is added when the model is listed in the top part of the right pane, see below:



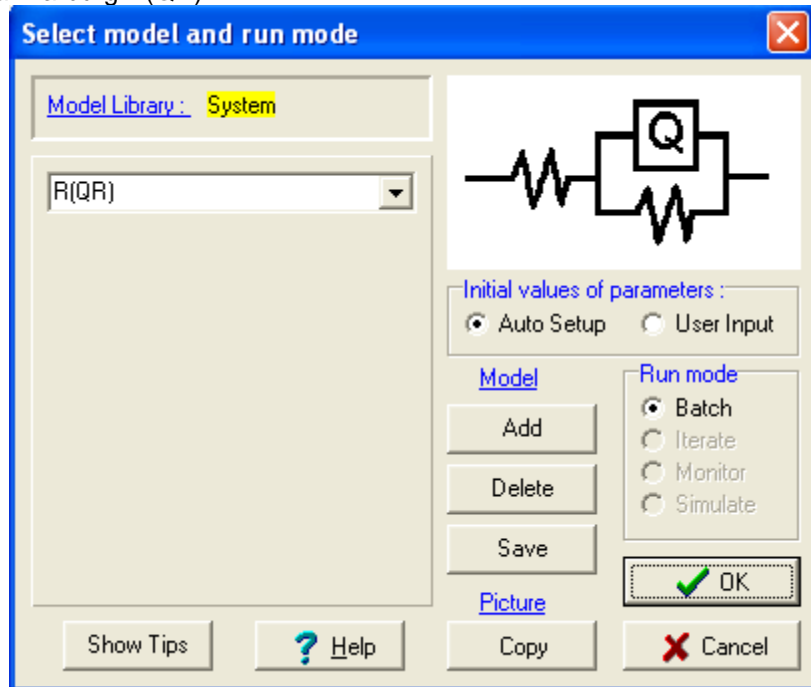


Repeat these steps to add the other three relevant models:

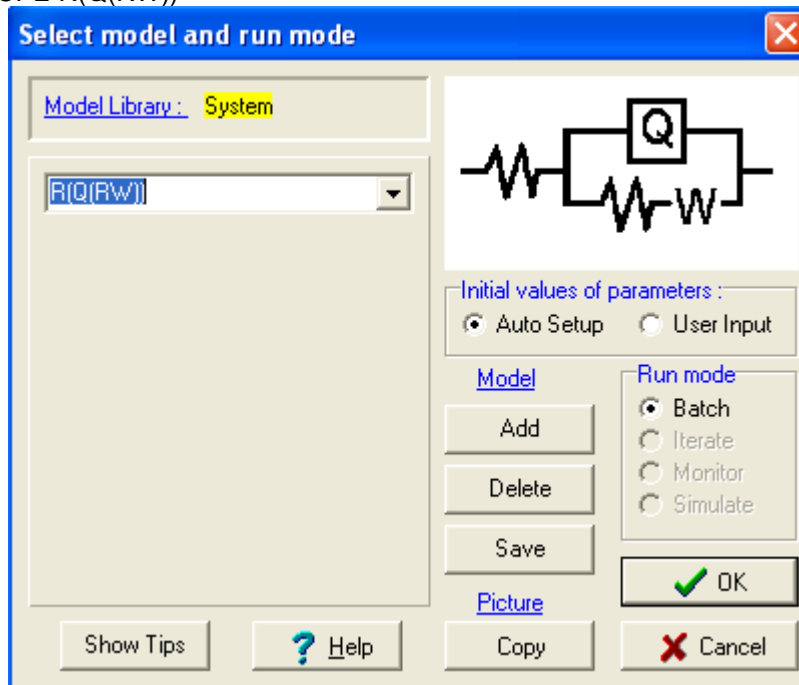
Warburg R(C(RW))



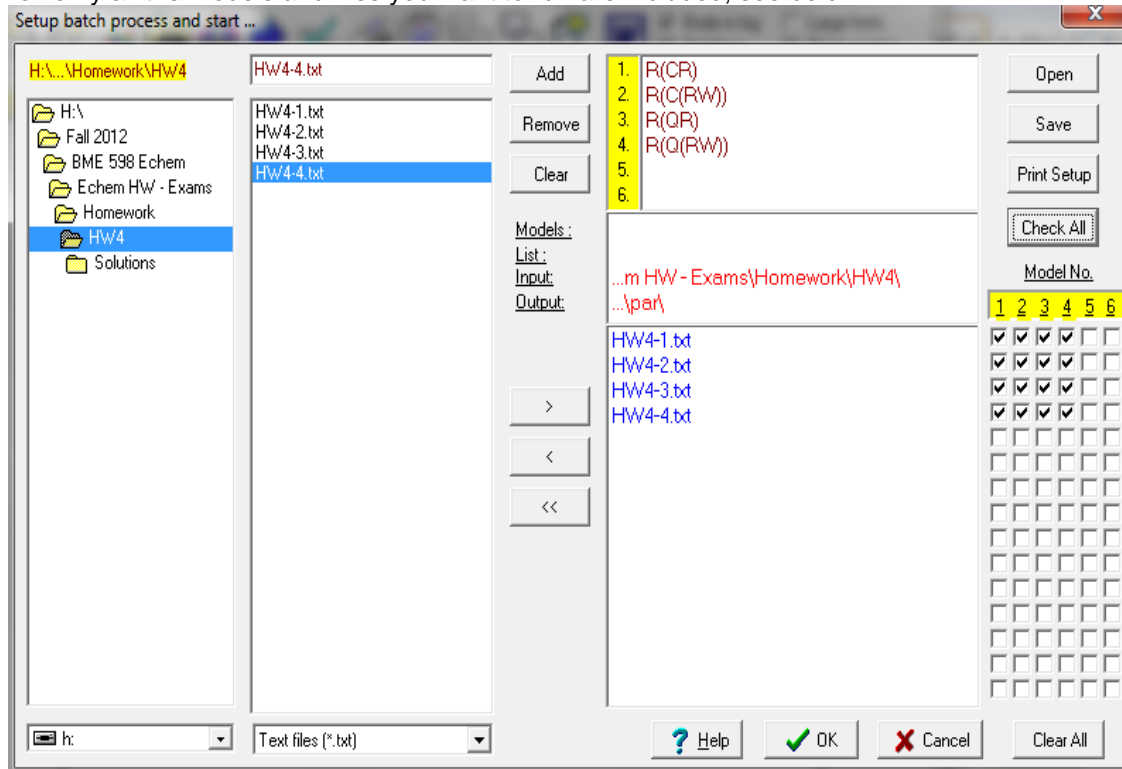
CPE without a Warburg R(QR)



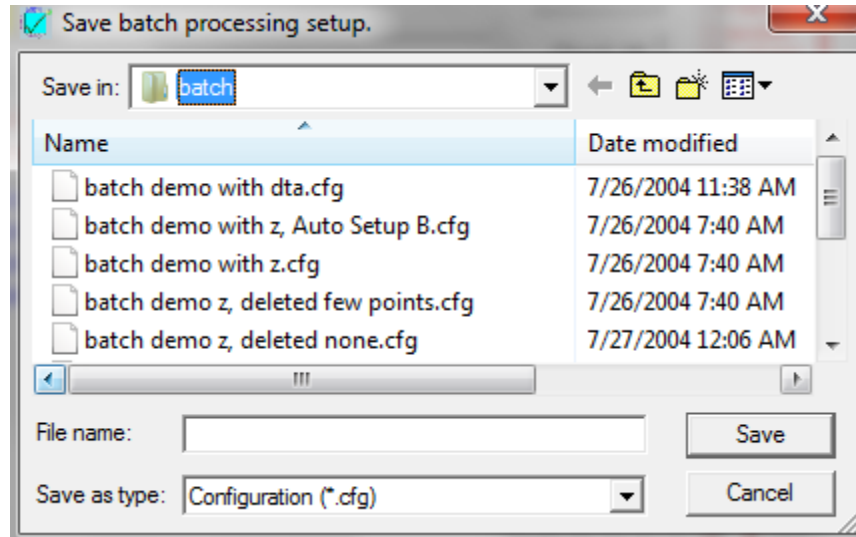
Warburg with CPE R(Q(RW))



To verify all the models and files you want to run are included, see below:



Now you have verified these models and files are added, you need to click “Check All” this will apply these models to all your data (the check marks on the right of the window will appear when you do this), then click “ok” at the bottom of the window. You will be prompted to save the batch:



Save this somewhere you will be able to find again later in case you need to look at the final results again. If you are running the demo version, you may get an error that says something along the lines of: you cannot create this file, click “ok” to these errors. The models will still run, but YOU CANNOT SAVE, so take screen shots, etc. when you get the results.

The results will take a little time to run, should be less than 5 mins. You will see a “Please Wait” window in the upper left portion of your screen while the center Zsimpwin window will be loading data, fitting models.

When it is done, a new window will appear prompting you to save, make sure it is where you want it then click “ok”.

Then another new window will appear:

Batch processing job execution statistics

Statistics: ...m HW - Exams\Homework\HW4\Solutions\Zsimp\Win Data\HW4\_4files\_4models.sta  
 Input: ...m HW - Exams\Homework\HW4\ Std. devs of # of pars with rel. std. Completed: 10/11/2012, 2:17:56 PM  
 Output: ...par\ data points errors? / # of est. pars

Job Identification	σ	pct	> 10%	> 100%	Start	End	Execution time mm:ss:zzz
Hw4-1, R(CR).par	26.60	0 / 3	0 / 3		2:16:13 PM	2:16:14 PM	00:00:890
Hw4-2, R(CR).par	26.20	0 / 3	0 / 3		2:16:14 PM	2:16:16 PM	00:01:180
Hw4-3, R(CR).par	25.99	2 / 3	0 / 3		2:16:16 PM	2:16:16 PM	00:00:770
Hw4-4, R(CR).par	9.33	0 / 3	0 / 3		2:16:16 PM	2:16:17 PM	00:00:900
Hw4-1, R(C(RW)).par	16.37	1 / 4	0 / 4		2:16:17 PM	2:16:18 PM	00:01:190
Hw4-2, R(C(RW)).par	11.08	2 / 4	2 / 4		2:16:18 PM	2:16:20 PM	00:01:110
Hw4-3, R(C(RW)).par	2.42	0 / 4	0 / 4		2:16:20 PM	2:16:20 PM	00:00:600
Hw4-4, R(C(RW)).par	8.96	1 / 4	0 / 4		2:16:20 PM	2:16:21 PM	00:01:350
Hw4-1, R(QR).par	17.42	1 / 4	0 / 4		2:16:21 PM	2:16:23 PM	00:01:050
Hw4-2, R(QR).par	5.68	0 / 4	0 / 4		2:16:23 PM	2:16:23 PM	00:00:960
Hw4-3, R(QR).par	17.74	4 / 4	1 / 4		2:16:23 PM	2:17:50 PM	01:26:417
Hw4-4, R(QR).par	3.01	0 / 4	0 / 4		2:17:50 PM	2:17:50 PM	00:00:380
Hw4-1, R(Q(RW)).par	5.97	0 / 5	0 / 5		2:17:50 PM	2:17:52 PM	00:02:020
Hw4-2, R(Q(RW)).par	5.07	1 / 5	0 / 5		2:17:52 PM	2:17:53 PM	00:01:160
Hw4-3, R(Q(RW)).par	2.39	1 / 5	0 / 5		2:17:53 PM	2:17:54 PM	00:00:870
Hw4-4, R(Q(RW)).par	3.02	1 / 5	1 / 5		2:17:54 PM	2:17:56 PM	00:01:560

Total # of jobs: 16 Page 1 of 1  Include skipped jobs --> View All Close

This is the result of the analysis, check "Include skipped jobs" (lower middle check box) and then

click "View All" and another new window will appear:

Scroll down toward the bottom until you see:

Standard deviations of data points, in % of |Z|.

1 2 3 4 → Data files

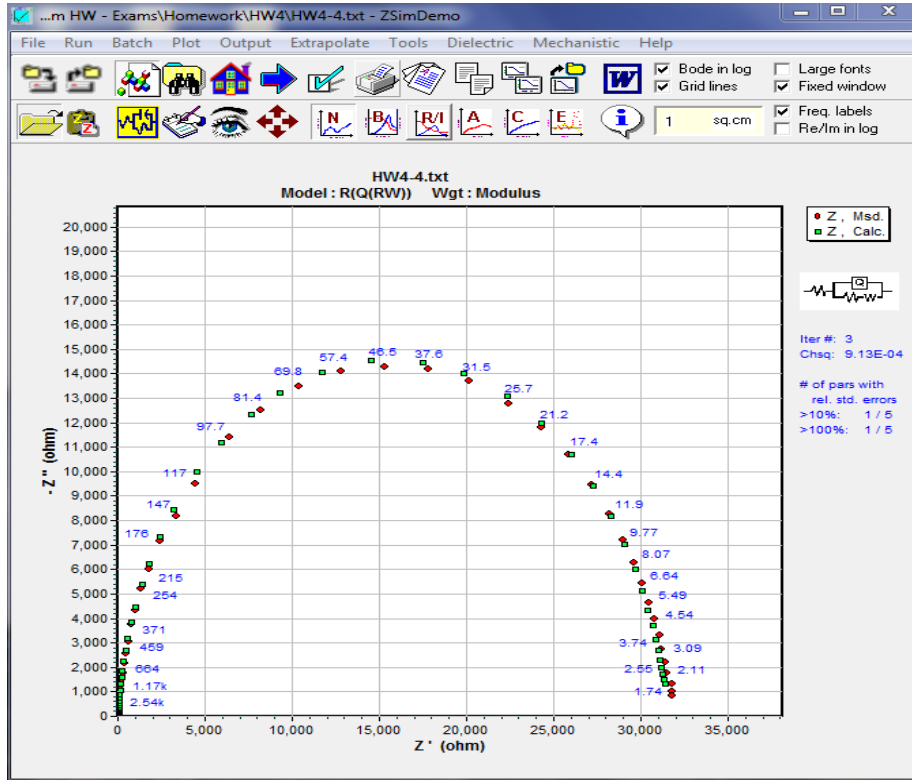
26.60	26.20	25.99	9.33	R(CR)
16.37	11.08	2.42	8.96	R(C(RW))
17.42	5.68	17.74	3.01	R(QR)
5.97	5.07	2.39	3.02	R(Q(RW))

→ Stdev's for R(CR) model for each file

\*\*\*These numbers can be copied and pasted.

This data tells you the best fit for each of the data files selected: lower %= better fit.

Close all the windows except Zsimpwin:



Now, you will open each .txt original data file (can only open one file at a time) by selecting the open folder icon below:



Then model using the best fitting model for that file (refer again to your stdev's table if necessary)

by selecting:



And select the best fitting model for that file as before.

You will be prompted to save, do so in a place you will find later. If you are in the demo version, you cannot save.

In the demo version, a new window will appear with the model parameters:

Input data: ...m HW - Exams\Homework\HW4\HW4-1.txt      Iteration #: 4

Model: R(Q(RW))

Parameter	Fixed?	Neg?	Start	End	Rel. std. error in percents	Inc. dir?
Resistance, [ohm]	<input type="checkbox"/>	<input type="checkbox"/>	11.01	11.01	2.88	<input type="checkbox"/>
CPE, Yo [S-sec <sup>n</sup> ]	<input type="checkbox"/>	<input type="checkbox"/>	0.0002354	2.354E-6	5.68	<input checked="" type="checkbox"/>
Freq power, n [0<n<1]	<input type="checkbox"/>	<input type="checkbox"/>	0.8635	0.8635	0.6901	<input type="checkbox"/>
Resistance, [ohm]	<input type="checkbox"/>	<input type="checkbox"/>	1366	1366	1.533	<input type="checkbox"/>
Warburg, Yo [S-sec <sup>.5</sup> ]	<input type="checkbox"/>	<input type="checkbox"/>	0.0009062	0.0009062	4.781	<input checked="" type="checkbox"/>
Not used	<input type="checkbox"/>	<input type="checkbox"/>	1	1	0	<input type="checkbox"/>
Not used	<input type="checkbox"/>	<input type="checkbox"/>	1	1	0	<input type="checkbox"/>
Not used	<input type="checkbox"/>	<input type="checkbox"/>	1	1	0	<input type="checkbox"/>
Not used	<input type="checkbox"/>	<input type="checkbox"/>	1	1	0	<input type="checkbox"/>
Not used	<input type="checkbox"/>	<input type="checkbox"/>	1	1	0	<input type="checkbox"/>
Not used	<input type="checkbox"/>	<input type="checkbox"/>	1	1	0	<input type="checkbox"/>
Not used	<input type="checkbox"/>	<input type="checkbox"/>	1	1	0	<input type="checkbox"/>
Not used	<input type="checkbox"/>	<input type="checkbox"/>	1	1	0	<input type="checkbox"/>
Not used	<input type="checkbox"/>	<input type="checkbox"/>	1	1	0	<input type="checkbox"/>

Weighting factor: Modulus 0.003567

Chi-squared: 0.003567

Meas. errors in Z: < 5.972 pct.

Run Mode:  Batch,  Iterate,  Monitor,  Simulate

Apply to Start?:  Signs,  Values

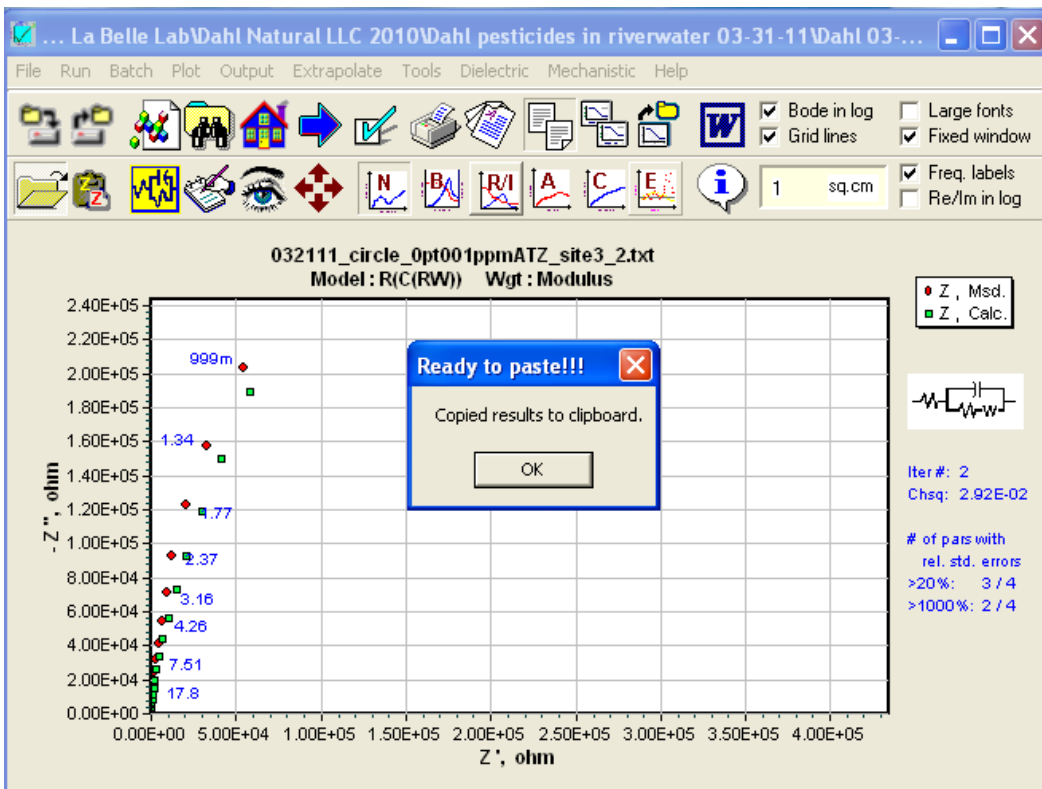
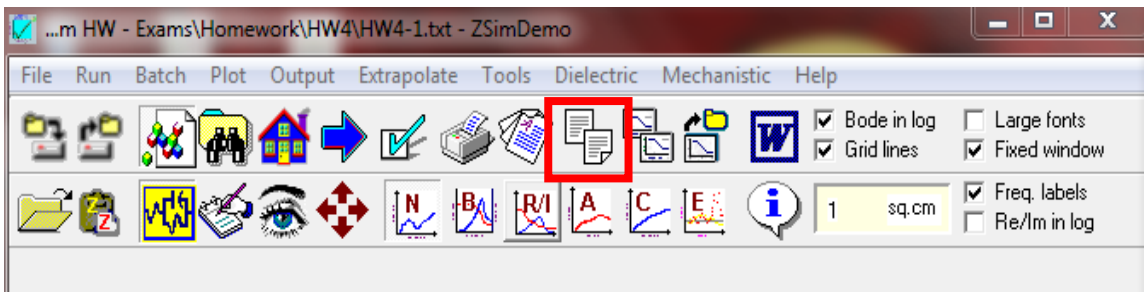
Buttons: Import, Reset, Search, **OK**, Cancel

Bottom buttons: Lock All, Free All, Print/Copy, Help, Cancel

These parameters can be adjusted if desired, but the software is capable of optimizing a fit (these numbers are the computer generated optimum fit). Click “ok” if you do not want to change the parameters. The simulation will run again, if you did not change the parameters click no when prompted to save.

*In the regular software:*

If you were able to save files in the non-demo version, you can select the copy paste button highlighted below to copy the results to the clipboard:





You will get a copied version of the results that look like below that you can paste into WORD

04/21/2011, 7:40:34 AM

...\par\032111\_circle\_Opt001ppmATZ\_site3\_2, R(C(RW)).par

1 = detect the sign of Zim  
1 = modulus weighting factor  
1.000 = sample area in square cm  
R(C(RW))  
2.920e-02 2 = chi squared, # of items

index	fixed	parameter	start	end	rel. std. error (%)
1	0	R	36.28	36.27	7.797
2	0	C	5.321E-7	5.32E-7	2.517E5
3	0	R	0.1236	0.1257	1.53E12
4	0	W	8.342E-7	8.345E-7	21.38

Measurement errors in impedance data = < 17.09 pct.

\*in Warburg w/o CPE model: index1= Rs, index 2= Cdl, index 3= Ret, index 4=Warburg

\*In Warburg w/ CPE model: index1= Rs, index 2= Q-Yo, index 3= Q-n, index 4= Ret

*Analyzing ZsimpWin Output:*

To see how well all these models fit your data, which is best (measured by % error and  $\chi^2$  –low numbers is great fit).

\*Note: The Q's are the nonlinear capacitance,  $Q = Y_o^n$  power

*Optional, but strongly encouraged:*

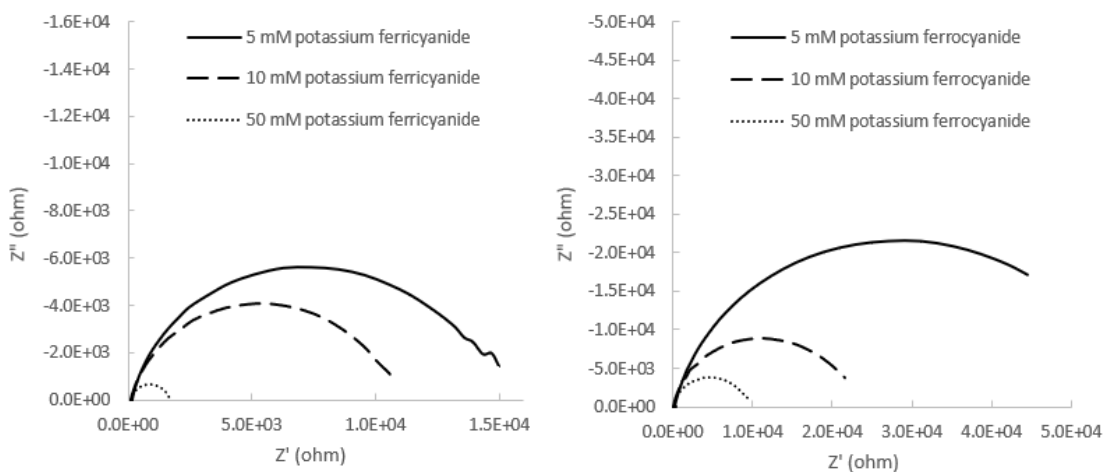
Place the end data (highlighted in yellow for the full software version and boxed in orange in the demo version outputs above) into an EXCEL file and plot versus LOG(concentration) and see if what it looks like next to your impedance plots. If you have a capacitive system, typically the plots are reverse, increasing CAP vs conc as opposed to decreasing Z vs conc.

APPENDIX G

CHANGE IN FERRI/FERRO CONCENTRATIONS ON SAM

The purpose of this experiment is to supplement the hypothesis that, when enzymatic reaction occurs on a GDE coated with an electron insulating self-assembled monolayer (SAM), the change in impedance maybe associated with potassium ferricyanide being reduced to potassium ferrocyanide. The electron insulating feature of SAM limits the electron transport of ferrocyanide, making it unable to drop its electrons and get oxidized back to ferricyanide. Because of that, the accumulation of ferrocyanide on SAM is causing an increase in impedance that's proportional to glucose concentration.

The sensor was prepared using GDEs described in Appendix B using 2 mg/mL of FAD-GDH. Three concentrations of potassium- ferricyanide and ferrocyanide were prepared: 5, 10, 50 mM. The biased potential used was 0.14V, which was the formal potential of potassium ferricyanide. The amplitude was set to 5 mV and frequency was swept from 1 to 100,000 Hz.



The figure above showed the change in impedance with respect to the change in redox mediators. As potassium ferricyanide's concentration decreases, the impedance increases.

In a typical setting, a gradient of glucose solutions prepared in 100 mM potassium ferricyanide would be tested. As the enzyme converts glucose to its byproducts, the generated electrons are facilitated by the ferricyanide through reduction and oxidation. However, when the electron-insulating SAM is present, the electrons cannot be passed onto the sensor at the same rate as electron generation (which is dependent on the glucose concentration). Consequently, more ferricyanide receives the electron, get reduced to ferrocyanide, and then accumulate on the SAM as more glucose is converted. This can be viewed as a decrease in the concentration of ferricyanide and an increase concentration in the ferrocyanide. From the figure above, one can see that, both the decrease in the concentration of ferricyanide and a small concentration of ferrocyanide will have large impedance. This phenomenon can be used to explain the contradicting result of increasing EIS glucose sensors prepared by SAM discussed in Chapter 2.2.